

**Oscillatory Flows in Periodically Interrupted
Rectangular Passages in Heat Exchangers**

by

Alexandre Lamoureux

Department of Mechanical Engineering

**McGill University
Montréal, Québec, Canada**

August, 2006

**A thesis submitted to McGill University
in partial fulfilment of the requirements for the degree of
Master of Engineering**

© Alexandre Lamoureux, Montréal, Québec, Canada, 2006



Library and
Archives Canada

Bibliothèque et
Archives Canada

Published Heritage
Branch

Direction du
Patrimoine de l'édition

395 Wellington Street
Ottawa ON K1A 0N4
Canada

395, rue Wellington
Ottawa ON K1A 0N4
Canada

Your file *Votre référence*
ISBN: 978-0-494-28601-2
Our file *Notre référence*
ISBN: 978-0-494-28601-2

NOTICE:

The author has granted a non-exclusive license allowing Library and Archives Canada to reproduce, publish, archive, preserve, conserve, communicate to the public by telecommunication or on the Internet, loan, distribute and sell theses worldwide, for commercial or non-commercial purposes, in microform, paper, electronic and/or any other formats.

The author retains copyright ownership and moral rights in this thesis. Neither the thesis nor substantial extracts from it may be printed or otherwise reproduced without the author's permission.

AVIS:

L'auteur a accordé une licence non exclusive permettant à la Bibliothèque et Archives Canada de reproduire, publier, archiver, sauvegarder, conserver, transmettre au public par télécommunication ou par l'Internet, prêter, distribuer et vendre des thèses partout dans le monde, à des fins commerciales ou autres, sur support microforme, papier, électronique et/ou autres formats.

L'auteur conserve la propriété du droit d'auteur et des droits moraux qui protègent cette thèse. Ni la thèse ni des extraits substantiels de celle-ci ne doivent être imprimés ou autrement reproduits sans son autorisation.

In compliance with the Canadian Privacy Act some supporting forms may have been removed from this thesis.

Conformément à la loi canadienne sur la protection de la vie privée, quelques formulaires secondaires ont été enlevés de cette thèse.

While these forms may be included in the document page count, their removal does not represent any loss of content from the thesis.

Bien que ces formulaires aient inclus dans la pagination, il n'y aura aucun contenu manquant.


Canada

ABSTRACT

Computational and experimental studies of fluid flow and heat transfer phenomena in interrupted-surface passages are presented. The computational investigation was focused on developing and fully-developed (spatially and temporally) laminar flow and heat transfer in essentially two-dimensional regions of the following passages: 1) a straight rectangular duct with spatially periodic in-line plate inserts; and 2) staggered-plate arrays. A second-order finite-volume method was developed, validated, and used to solve these problems. Time-mean modular friction factors and Colburn factors were obtained from the domain inlet to the spatially-periodic fully-developed region for a Reynolds number range of 100 to 600, thus exploring the laminar steady and unsteady regimes. Additionally, various cyclic domains were investigated. In the experimental investigation, single hot-wire measurements were used to obtain ensemble-averaged power spectrums and Strouhal numbers in the fully-developed region of the rectangular duct with spatially periodic in-line plate inserts, for Reynolds numbers ranging from 2000 to 30000.

RÉSUMÉ

Cette œuvre présente des études numériques ainsi qu'expérimentales d'écoulements et d'échanges thermiques dans des géométries à surfaces discontinues. Les études numériques visèrent à simuler des écoulements dans les passages bidimensionnels suivants : 1) un conduit rectangulaire interrompu par des plaques périodiquement espacées; 2) des matrices de plaques décalées. Une méthode des volumes finis du second ordre fut développée et validée. Les simulations permirent d'obtenir les facteurs de friction et de Colburn des modules, de l'entrée jusqu'à la région d'écoulement développé, pour des nombres de Reynolds de 100 à 600, explorant ainsi les régimes laminaires permanents et non permanents avec divers domaines cycliques. Les études expérimentales eurent pour objectif d'obtenir des mesures au fil chaud dans la région d'écoulement développé d'un conduit rectangulaire interrompu par des plaques périodiquement espacées afin de calculer des spectres de puissance et les nombres de Strouhal pour des nombres de Reynolds de 2000 à 30000.

ACKNOWLEDGEMENTS

First, I am sincerely grateful to my mentor and supervisor, Professor B.R. Baliga, for his guidance, support and inspiring spirit. I want to especially thank him for sharing his admirable wisdom and for passing on his quest to surpass one's own limits.

I would like to thank the Natural Sciences and Engineering Research Council of Canada (NSERC) for a graduate scholarship and for research grants to Professor Baliga. The parallel offer of support from the Fonds québécois de la recherche sur la nature et les technologies (FQRNT) is also very appreciated.

I am also grateful to the Mechanical Engineering Department staff for their help and advice. I would like to thank George Twefik and Peter Chau for their technical support. I would also like to convey my thanks to the secretaries, Della Maharajh, Joyce Nault, and Jean Milliken for their precious help with the paperwork.

Many thanks to Tony Micozzi and his team from the Machine Tool Laboratory for crafting the parts required to perform the hot-wire measurements.

I would like to thank Professor Laurent Mydlarski and Mr. Étienne Costa-Patry for their help with hot-wire anemometry as well as for sharing the wind tunnel and anemometer.

I am thankful to the members of the Heat Transfer Laboratory, David Scott, Nima Atabaki, Nirmalakanth Jesuthasan, Lorena Camargo, and Éric Duplain for transforming our individual burdens into a memorable and enjoyable collective adventure.

To my friends André Leclerc and Mathieu Bock-Côté, thank you for your loyal friendship and enjoyable company during these years. Merci messieurs.

I am infinitely indebted to my parents for their love and support that can never be thanked enough. For all those words of encouragement, thank you.

Finally, I would like to thank Karine Dubois for her everlasting love, remarkable patience and for brightening up every day.

TABLE OF CONTENTS

Abstract	II
Résumé	III
Acknowledgements.....	IV
Table of Contents	V
List of Figures	VII
List of Tables	VIII
Nomenclature	IX
Chapter 1 - Introduction	1
1.1 <i>MOTIVATION AND OVERALL GOAL</i>	1
1.2 <i>LITERATURE REVIEW</i>	6
1.2.1 Investigations of fluid flow and heat transfer in offset fin cores and analogous model geometries	6
1.2.2 Investigations of fluid flow and heat transfer in model interrupted-surface ducts	15
1.2.3 Textbooks, review articles, and other contributions	21
1.3 <i>SPECIFIC OBJECTIVES</i>	23
1.4 <i>THESIS OVERVIEW</i>	24
Chapter 2 – Theoretical Considerations.....	25
2.1 <i>GOVERNING EQUATIONS</i>	25
2.1.1 General form of governing equations	26
2.1.2 Governing equations for numerical investigations	27
2.2 <i>DESCRIPTION OF THE SPATIALLY PERIODIC FULLY-DEVELOPED REGIME</i>	27
2.2.1 General definition	27
2.2.2 Governing equations for spatially periodic fully-developed laminar two- dimensional steady flows	30
2.3 <i>ENSEMBLE AVERAGED POWER SPECTRUM AND STROUHAL NUMBERS</i>	32
2.4 <i>DIMENSIONLESS PARAMETERS</i>	34
2.4.1 Dimensionless parameters pertaining to experiments in rectangular interrupted- plate ducts	34
2.4.2 Dimensionless parameters pertaining to numerical investigations of interrupted-surface passages	35
Chapter 3 – Experimental Apparatus and Techniques.....	39
3.1 <i>OVERVIEW OF THE EXPERIMENTAL APPARATUS</i>	39
3.2 <i>HOT-WIRE TEST SECTION AND INSTRUMENTATION</i>	42
3.3 <i>SUMMARY OF THE EXPERIMENTAL PROCEDURE</i>	45

Chapter 4 – Numerical Method	48
4.1 GOVERNING EQUATIONS	48
4.2 DOMAIN DISCRETIZATION	49
4.2.1 Types of domain	49
4.2.2 Node nomenclature	52
4.3 DISCRETIZED CONSERVATION EQUATIONS	53
4.3.1 Time and space integration of equations	53
4.3.2 Approximation of diffusion transport terms	55
4.3.3 Approximation of advection transport terms	56
4.3.4 Complete discretized equation.....	59
4.3.5 Modified QUICK scheme for given diffusion flux boundary condition	61
4.3.6 Additional details.....	64
4.3.7 Discretized pressure equations.....	66
4.3.8 Treatment of solid regions	68
4.4 SOLUTION OF THE DISCRETIZED EQUATIONS	70
4.4.1 Overview of solution procedure.....	70
4.4.2 Description of line-by-line cyclic solvers	72
4.4.3 Block-correction procedure	73
4.4.4 Underrelaxation.....	75
Chapter 5 – Results and Discussion	76
5.1 RESULTS OF THE EXPERIMENTAL INVESTIGATIONS.....	76
5.1.1 Benchmarking of hot-wire apparatus and preliminary experiments.....	76
5.1.2 Results of lateral symmetry and spatial periodicity investigations.....	80
5.1.3 Turbulence power spectrums	83
5.1.4 Vortex shedding strouhal numbers	88
5.2 RESULTS OF THE NUMERICAL INVESTIGATIONS	91
5.2.1 Test problem #1: steady spatially-periodic fully-developed laminar flow and heat transfer in staggered plate arrays.....	92
5.2.2 Test problem #2: unsteady laminar flow past a square cylinder.....	98
5.2.3 Numerical investigation #1: unsteady laminar developing flow in interrupted-plate ducts	103
5.2.4 Numerical investigation #2: unsteady laminar developing flow and heat transfer in staggered-plate arrays.....	111
Chapter 6 – Conclusion	122
6.1 REVIEW OF THE THESIS AND ITS MAIN CONTRIBUTIONS.....	122
6.2 SUGGESTIONS FOR EXTENSIONS OF THIS WORK	125
References	127

LIST OF FIGURES

1.1	Core of an offset-fin compact heat exchanger.	2
1.2	Core of an offset strip fin heat exchanger.	3
1.3	Schematic illustration of a rectangular interrupted-plate duct.	5
3.1	Schematic of the experimental apparatus.	39
3.2	Top view of the visualization section and wire holder insertion holes.	43
3.3	Positions of the single hot-wire probe in the longitudinal cross-section of the duct.	44
4.1	Example of a cyclic computation domain.	50
4.2	Representation of a regular computation domain.	50
4.3	Sample grid and node notation indexes for a cyclic grid.	51
4.4	CVFDM grid and nomenclature for a node and its related neighbors.	52
4.5	Evolution of the dependent variable in time.	55
4.6	QUICK interpolation scheme of a dependent variable ϕ	57
4.7	QUICK scheme referencing to undetermined north node.	62
4.8	Sweeps in the line-by-line iterative solvers.	72
5.1	Strouhal number of vortex shedding from a cylinder in unconfined crossflow.	77
5.2	Power spectrums showing repeatability (H2, P8, $Re \approx 20000$).	78
5.3	Power spectrums showing vertical symmetry (H2, P5, and mirror position): $Re \approx 5000$	79
5.4	Power spectrums showing vertical symmetry (H2, P5, and mirror position): $Re \approx 20000$	80
5.5	Power spectrums showing lateral symmetry (P8): $Re \approx 5000$	81
5.6	Power spectrums showing lateral symmetry (P8): $Re \approx 20000$	81
5.7	Power spectrums showing spatial periodicity in the axial direction (P8): $Re \approx 5000$	82
5.8	Power spectrums showing spatial periodicity in the axial direction (P8): $Re \approx 20000$	83
5.9	Power spectrums at position P5 and hole H2.	84
5.10	Power spectrums at position P8 and hole H2.	84
5.11	Power spectrums at position P11 and hole H2.	85
5.12	Power spectrums at position P10 and hole H2.	86
5.13	Power spectrums at position P1 and hole H2.	87
5.14	Power spectrums at position P2 and hole H2.	87
5.15	Strouhal numbers at positions P1 and P4, in hole H2.	88
5.16	Strouhal numbers at positions P2, P5, P8, and P11, in hole H2.	89
5.17	Strouhal numbers at positions P9 and P12, in hole H2.	89
5.18	Vortex shedding Strouhal numbers with respect to axial position (z), in hole H2.	90
5.19	Cross-sectional view of a staggered plate array and the computational domain.	92
5.20	Streamline plots for $t/H = 0.2$ and β^* values of 9687.5, 4687.5 and 625.	97
5.21	Computational domain and boundary conditions for Test Problem # 2.	99
5.22	Strouhal number as function of Reynolds number.	102
5.23	Instantaneous streamline plot for $Re = 300$ and $t/H = 0.32$	109
5.24	Cross-sectional view of staggered-plate array and computational domain.	112
5.25	Instantaneous streamline plot for $Re = 600$ and 6X2 module domain (sol. 1).	118
5.26	Fully-developed f and j factors as functions of Re ($t/H = 0.25$ and $L = 2H$).	120

LIST OF TABLES

3.1 Geometric parameters of the test and visualization sections.	40
3.2 Coordinates of the hot-wire positions with reference to the local x-z axis (figure 3.3) (in mm).....	44
5.1: Results for test problem #1: Values of Re, ff and j for $t/H = 0.1$	96
5.2: Results for test problem #1: Values of Re, ff and j for $t/H = 0.2$	96
5.3: Results for test problem #1: Values of Re, ff and j for $t/H = 0.3$	97
5.4: Results for test problem #2: Values of St and C_D	101
5.5: Time-mean module friction factors for $Re = 382.65$ and $t/H = 0.32$	106
5.6: Time-mean module friction factors for $t/H = 0.32$	108
5.7: Time-mean module friction factors for $t/H = 0.20$	108
5.8: Fully-developed module friction factors ($t/H = 0.32$) compared with results of Sebben (1996).	110
5.9: Fully-developed module friction factors ($t/H = 0.20$) compared with results of Sebben (1996).	110
5.10: Strouhal numbers compared with results of Sebben (1996).	110
5.11: Time-step independence study: values of ff and j factors for $Re = 1000$	114
5.12: Grid independence study: values of ff and j factors for $Re = 1000$	114
5.13: Values of ff factors, j factors, and Strouhal numbers for $t/H = 0.25$ and $L = 2H$	117
5.14: Values of ff factors, j factors, and Strouhal numbers for $t/H = 0.25$ and $L = 2H$	119

NOMENCLATURE

α_p, α_{NB}	Coefficients in the discretized equation for ϕ
$A_{c-s-min}$	Minimum cross-sectional flow area of the geometry
$A_{H.T.}$	Heat transfer area of module
A_{wetted}	Total wetted solid surface area in referred module
$A1, A2$	Coefficients used in boundary treatment calculations
b	Duct width; Coefficient of constant term in the discretized equation for ϕ (meaning is clear in context)
c_p	Specific heat at constant pressure
$C1, C2, C3$	Coefficients used in the QUICK scheme
C_D	Drag coefficient
C_L	Lift coefficient
d_u, d_v	Coefficients used in pressure coefficient calculation
D	Diameter of square cylinder
D_h	Hydraulic diameter
f	Weighting function in time integration
f	Darcy friction factor; frequency (meaning is clear in context)
f_v	Vortex-shedding frequency
ff	Time-mean module friction factor
F_D	Drag force on object
F_L	Lift force on object
$Flux_{in}$	Entering flux of ϕ in domain boundary control volumes
\underline{g}	Magnitude of the gravitational acceleration
\bar{h}	Average modular heat transfer coefficient
H	Duct or array module half-height
$H(f)$	Fourier transform
j	Time-mean module Colburn factor
J	Total convective and diffusive flux across a control volume face
k	Thermal conductivity
LMTD	Log-mean temperature difference
L^*	Dimensionless plate length
\dot{m}	Mass flow rate
p	Instantaneous reduced static pressure
\tilde{p}	Periodically varying component of p
P_{atm}	Measured atmospheric pressure
$P_{hot-wire}$	Measured static pressure at hot-wire axial position
P_{stag}	Measured stagnation pressure in Pitot tube
P_{static}	Measured static pressure near Pitot tube
Pr	Prandtl number

NOMENCLATURE (continued)

$PSD_m(f)$	Modified power spectral density
Q_{module}	Modular heat transfer
$Q_{vol.}$	Volumetric heat source of control volume
Re	Reynolds number (as defined in text)
Re_{D_h}	Reynolds number based on the hydraulic diameter
s	Plate spacing
s^*	Dimensionless plate spacing
Sc	Schmidt number
Sh	Sherwood number
St	Stanton number; Strouhal number (meaning is clear in context)
S_ϕ	Volumetric average source term in equation for ϕ
t	Plate half-thickness
t	Time
t^*	Dimensionless plate thickness
Δt	Time step
Δt_{block}	Sampling time for a block of data
T	Temperature
T_B	Bulk temperature
T_{in}	Entering flow temperature
T_w	Plate temperature
\tilde{T}	Periodically varying component of T
ΔT	Temperature difference (as defined in text)
u	Instantaneous velocity component in x-direction
\hat{u}	Pseudo-velocity in x-direction
u_m	Mass-conserving u velocity at a control volume face
\bar{U}	Average velocity based on the nominal cross-sectional flow area
\bar{U}_{c-smin}	Average velocity at the minimum cross-sectional flow area
U_0	Freestream velocity
v	Instantaneous velocity component in y-direction
\hat{v}	Pseudo-velocity in y-direction
v_m	Mass-conserving v velocity at a control volume face
v'	Instantaneous fluctuation about the time-mean value of v
\bar{v}	Time-mean value of v
\vec{v}	Velocity vector
w	Instantaneous velocity component in z-direction
W	Wall factor, equal to 0 or 1, in the pressure contribution calculations and block correction algorithm

NOMENCLATURE (continued)

\bar{W}	Average axial velocity at the minimum cross-sectional area
x,y,z	Cartesian coordinate axes
Δx	Control volume width (in x-direction)
Δy	Control volume height (in y-direction)
α	Underrelaxation factor
β	Time-mean reduced static pressure drop per unit length
β^*	Dimensionless value of β
Γ_ϕ	Diffusion coefficient for variable ϕ
δx	Distance between two given nodes in x-direction
δy	Distance between two given nodes in y-direction
λ	Dimensionless duct width
Λ	Spatial period length of module
μ	Viscosity
ρ	Density
ϕ	Dependent variable

CHAPTER 1 - INTRODUCTION

1.1 MOTIVATION AND OVERALL GOAL

This thesis is an endeavor of the author and his supervisor to contribute to the ongoing worldwide efforts to develop compact heat exchangers with significant performance enhancements, compared to that of currently available versions of these devices. The overall goal of this work is to facilitate improvements of existing cost-effective computational tools for the thermofluid design of such heat exchangers, by conducting complementary numerical and experimental investigations.

The present thesis focuses on flow and heat transfer phenomena present in the cores of compact heat exchangers. These cores are defined as *compact* when they possess a surface area to volume ratio superior to $700 \text{ m}^2/\text{m}^3$. This compactness makes these heat exchangers quite desirable for numerous applications: examples include automobile radiators, coolers for electronic device, industrial gas turbine recuperators, HVAC (heating, ventilating and air-conditioning) systems, and aircraft oil coolers [McDonald (1972, 2000); Timmerhaus and Flinn (1989); Manglik and Bergles (1995); Shah et al. (2001); Kakaç and Liu (2002)]. Due to their enviable characteristics, these heat exchangers have grown in popularity and a lot of research efforts have been deployed to enhance and predict their performance.

A wide variety of compact heat exchanger core geometries are currently used. The configuration of interest in this work is the rectangular plate-fin design. It is generally composed of superimposed parallel plates separating layers of hot and cold fluids exchanging heat. To augment heat transfer, fins are positioned in between these plates. Multiple types of fins exist, the most popular having the following shapes: continuous, rectangular offset, zigzag, chevron, perforated and louvered fins [Kays and London (1984)]. They provide desirable heat transfer effects by increasing the heat exchange surfaces, inducing flow mixing, interrupting boundary layers, and inducing vortex

shedding. The fins may also serve as structural reinforcements. However, the associated heat transfer improvements are likely to be accompanied by increases in pressure drop for the same fluid flow rates.

In this thesis, the numerical and experimental investigations are focused on two interrupted-surface geometries: the offset-fin geometry shown in figure 1.1; and the rectangular interrupted-plate duct portrayed in figure 1.3. The fluid flow in the rectangular interrupted-plate duct of figure 1.3 has features akin to those that occur in the highlighted flow passage shown in figure 1.1.

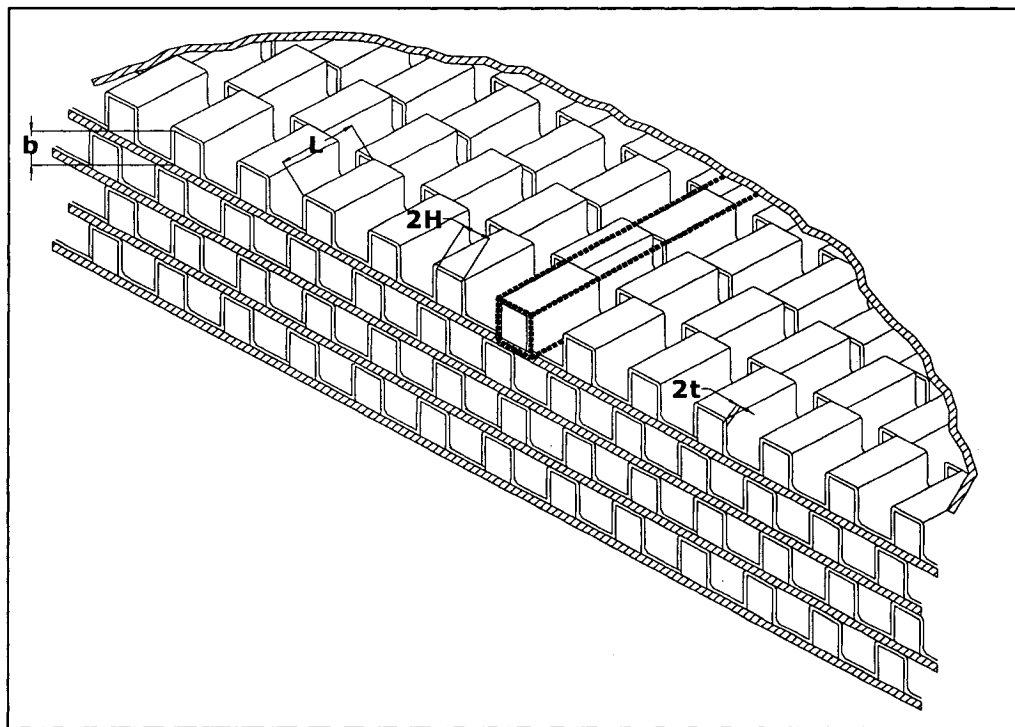


Figure 1.1 Core of an offset-fin compact heat exchanger.

The offset-fin core, shown above with some of its dimensional characteristics, is composed of multiple fin rows in between pairs of parallel plates. The fins are not continuous, as each row is offset with respect to the previous one, thus explaining its name. In this work, the dimensional parameters of such a core are denoted as follows: L represents the length of a fin row in the main flow direction; $2t$ denotes the thickness of the fins; b symbolizes the plate spacing; and $2H$ is the inverse of the fin pitch. This

geometry is usually manufactured by bending metal strips into fin rows that are subsequently brazed with the plates to form the core assembly: this type of configuration is referred to as an “offset strip fin” (shown below in figure 1.2).

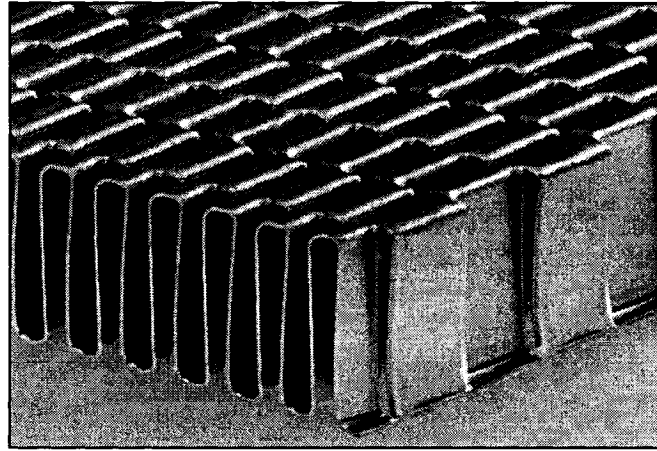


Figure 1.2 Core of an offset strip fin heat exchanger.
(Hughes-Treitler Manufacturing Corporation).

Numerous experimental investigations have been performed [Kays and London (1964, 1984)] on the offset-fin core configuration to obtain empirical data useful for design and accurate performance predictions. Measurements have been made on actual heat exchangers, full-scale models, and representative models, such as the aforementioned rectangular interrupted-plate duct. Correlations for pressure drop and heat transfer coefficients have been formulated based on the acquired empirical data. Some analytical solutions have also been presented.

Numerous numerical investigations of fluid flow and heat transfer in models of offset-fin cores have also been carried out over the last few decades. The first of such investigations simulated two-dimensional laminar steady flows in a simplified geometry, in which fin thickness was nil and the computational domain was limited to a single module with cyclic axial and lateral boundaries [Sparrow et al. (1977); Patankar and Prakash (1981)]. Later simulations were more sophisticated and included flow unsteadiness [Zhang et al. (1997)], fin thickness [Patankar and Prakash (1981)], turbulence effects [Sebben (1996)], three-dimensionality [Kelkar and Patankar (1989)], and influences of multiple modules

[Sebben (1996)]. However, there is a lack of modern computational analyses of developing flows in such geometries. Therefore, one of the author's objectives in this work was to contribute to the ongoing research efforts by simulating unsteady laminar flows and heat transfer from the entrance of the core to the temporally and spatially periodic fully-developed conditions. Additionally, various cyclic domains were investigated.

In order to maximize heat transfer and reduce pressure losses in the cores of compact heat exchangers, researchers and designers must investigate the influence of geometric and thermofluid parameters. The long-term goal in this regard is to develop mathematical models and numerical solution methods that are able to accurately predict flows and heat transfer in such heat exchanger cores for any flow regime (laminar, transitional, and turbulent), a feat that still remains largely unattained. The aim in this thesis is to contribute to the efforts directed at achieving this goal.

In order to validate and refine new mathematical models of fluid flow and heat transfer in the cores of compact heat exchangers, precise experimental data are needed. Accurate local measurements are hard to obtain on real exchangers. Therefore, researchers have leaned towards experiments on model geometries. Such investigations have been carried out by Cur and Sparrow (1978), McBrien and Baliga (1988), Sekulic (1989), Amon et al. (1992), and Grosse-Gorgemann et al. (1995). One of these models, the rectangular interrupted-plate duct, is shown in figure 1.3. It consists of a rectangular duct with evenly spaced plates inserted along its central (y - z) plane. The geometry of this duct mimics (to some extent) a section of the offset fin heat exchanger core, highlighted in figure 1.1. Additionally, flows in this model duct reproduce the heat transfer enhancing mechanisms observed in real cores, such as vortex shedding and boundary layer interruption. However, the ability to obtain precise local measurements is the main advantage of using such model geometries. Therefore, the interrupted-plate duct is a convenient and effective geometry to gather the experimental data required to refine the aforementioned mathematical models and numerical solution methods.

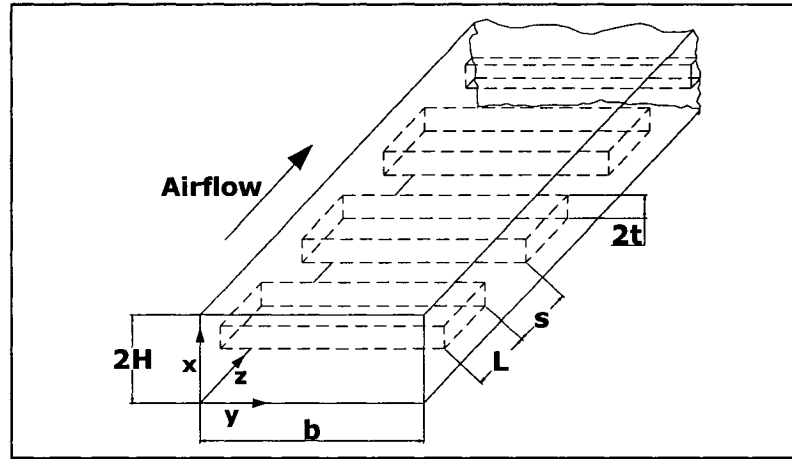


Figure 1.3 Schematic illustration of a rectangular interrupted-plate duct.

Some key numerical contributions in this area include the works of Sparrow et al. (1977) and Patankar et al. (1977), in which the concept of a *spatially periodic fully developed flow regime*, explained in further detail in chapter 2, was proposed. Curr and Sparrow (1978, 1979) have experimentally investigated the developing length (from the inlet) that is required for the establishment of the spatially periodic fully developed regime. McBrien and Baliga (1988) have provided accurate wall static pressure measurements for turbulent flows in rectangular interrupted-plate ducts similar to that shown in figure 1.3. Candanedo et al. (2003) extended the work of McBrien and Baliga (1988) by providing highly accurate time-mean intramodular pressure measurements for a wide range of flow parameters and geometric configurations. However, empirical data on turbulence statistics, which could be potentially useful for the validation of mathematical models and numerical solution methods suitable for computer simulations of unsteady turbulent flows in interrupted-surface geometries, for example, direct numerical simulation (DNS) and large eddy simulation (LES), are scarce in the literature. Therefore, the experimental part of this thesis is devoted to complementing and building on the work of Candanedo et al. (2003), by performing single hot-wire anemometry measurements at multiple locations in a rectangular interrupted-plate duct (similar to that in figure 1.3) for a wide range of Reynolds number. The aim in this part of the work is to use such measurements to obtain turbulence power spectrums and Strouhal numbers (when oscillatory flows, including vortex shedding, occur).

1.2 LITERATURE REVIEW

The objective in this section is to present a concise review of the major contributions in the published literature directly relevant to the present thesis work. The review surveys two principal research subjects: first, past investigations of flows and heat transfer in actual offset fin exchanger cores and analogous model geometries; and then, important research contributions on flow and heat transfer in model interrupted-surface ducts. Finally, important textbooks and classical works related to heat exchangers as well as computational fluid dynamics and heat transfer are mentioned.

1.2.1 INVESTIGATIONS OF FLUID FLOW AND HEAT TRANSFER IN OFFSET FIN CORES AND ANALOGOUS MODEL GEOMETRIES

1.2.1.1 EXPERIMENTAL AND ANALYTICAL INVESTIGATIONS

London and Shah (1968) conducted one of the first experiments on actual offset-fin cores. They investigated flow and heat transfer in eight different configurations. Heat transfer measurements were made with a steam-to-air steady test method for seven of the eight cores and a transient method for the last core. The authors used their measurements for calculating fanning friction factors and Colburn factors at multiple Reynolds number values. Their results were later incorporated into a book by Kays and London (1984). After analyzing their results, London and Shah (1968) recommended some desirable geometrical parameters, such as a small fin length (L), a small fin thickness ($2t$), and a large aspect ratio ($b/2H$). Finally, they warned that the processes used to manufacture the core must be strictly controlled since slight deviations, such as burred fin edges, might cause some significant performance departures from the predicted results.

Kays (1972) presented one of the first analytical models of laminar flows in offset-fin cores. By adapting the boundary layer solution of flow over a flat plate [Schlichting

(1968)] to the offset-fin geometry, he devised a model for predicting frictions factors and heat transfer performance.

Wieting (1975) proposed the first empirical correlations for predicting friction and Colburn factors for offset-fin heat exchanger cores. He correlated flow friction and heat transfer data gathered from 22 different cores by other researchers. Wieting believed that the development of empirical relationships obtained by correlating empirical data was the best method available to predict heat exchanger performance. He proposed two such correlations, one for friction factors and another for Colburn factors. Each of these correlations is a function of geometric variables and the Reynolds number. Wieting correlated data for laminar and turbulent flows separately. Therefore, the values of the coefficients and exponents in his correlations depend on the flow regime, itself estimated in accordance with prescribed limits on the values of Reynolds number. To predict performance in the transitional range, Wieting proposed two “threshold” Reynolds number formulas, indicating which of the laminar or turbulent correlations should be used. Wieting’s correlations have been widely used by designers, and they are regarded as a simple, yet relatively accurate, method of predicting heat exchanger performance. His work is also considered to be one of the most significant milestones in this field of research.

Webb and Joshi (1982) later tried to improve on the work of Wieting (1975) by performing experiments on a scaled-up model of an offset strip fin core. They sought accurate empirical data for a wider range of dimensional parameters. The authors argued that such measurements should be made on scaled-up arrays in which geometrical dimensions can be strictly controlled and the effects of imperfections, such as burred edges, may be isolated. Webb and Joshi obtained friction factor data for eight different cores for the lower range of Reynolds number: they used an aqueous ethylene glycol mixture as the test fluid since it generated pressure drops large enough to be measured accurately with manometers. These authors developed a new friction factor correlation, which is, in their opinion, more accurate than that of Wieting (1975). Finally, their correlation, developed with their model data, also precisely predicted friction factors

measured in real heat exchanger cores. Therefore, they stated that the effects of burred edges and other dimensional deviations on the flow are relatively insignificant.

Mullisen and Loehrke (1986) investigated the flow mechanisms that enhance heat transfer in certain compact heat exchanger cores. They used flow visualization in scaled-up models to identify various flow regimes present in the following geometries: in-line plates, staggered offset plates, and perpendicular plates. Measurements were performed in a wind tunnel for a total of eight different dimensional configurations over a range of Reynolds number, based on the Kays and London (1984) definition, of 100 to 10000. Mullisen and Loehrke observed three different flow regimes prevailing in the arrays: steady, general unsteady, and periodic unsteady. The first was characterized by continuous boundary layers over the plates and the interstices; the second displayed flow unsteadiness growing in the downstream direction; and the last was characterized by synchronized vortex shedding from the trailing edges of the upstream plates and was always accompanied by audible tones. Interestingly, the periodic unsteady flow regime was not encountered in the perpendicular plate arrays, but no explanation was given for this finding. Lastly, the authors also assessed the quantitative performance improvements of interrupted surface arrays over that of continuous plate geometries. In particular, they obtained friction factors and heat transfer coefficients with measurements from a transient technique and found that enhancements of over 100 percent in the average heat transfer coefficients may be attained by incorporating surface interruptions.

Joshi and Webb (1987) proposed analytical models to predict the friction factors and Colburn factors of offset-fin heat exchanger cores. They defined two flow regimes, laminar and turbulent, formulated a different model for each, and presented an equation predicting the transitional Reynolds number. Their laminar flow model was based on the numerical solution of Sparrow and Liu (1979). For the turbulent regime, a semi-empirical model was proposed. These authors validated their analytical friction factor model with their own experimental data, obtained for eight model core configurations. The friction factor predictions fell within $\pm 20\%$ of their experimental data. The Colburn factor predictions were compared with experimental heat transfer data gathered by multiple

authors: the predictions were within $\pm 20\%$ of the measured data for 19 of the 21 selected cores. They also conducted visualization experiments to investigate flow regimes and validate their transition-point formula. With increasing values of Reynolds number, the flow departed from a smooth laminar appearance to a vortex-shedding regime. Finally, Joshi and Webb proposed empirical correlations similar to those of Wieting (1975), in conjunction with their flow regime transition limit formula.

Mochizuki et al. (1988) investigated pressure drops and turbulence intensity in model heat exchanger cores. They studied 18 different test cores of three types of geometry: plain fin, offset fins, and slotted fins. The test cores were installed in a suction type wind tunnel fitted with pressure taps and three hot-wire probes at different locations along the airflow path. Static pressure distributions were obtained for a wide range of Reynolds number based on the Kays and London (1984) definition (3500 to 13000). These authors observed that the pressure drops increased almost linearly along the core and also noticed that shorter fin lengths generated higher pressure losses. They also pointed out that the turbulence intensity in offset strip fin cores was not uniform throughout the core at lower Reynolds numbers, the turbulence intensity was low in the entry zone and gradually increased downstream. For higher values of Reynolds number, the turbulence intensity was found to be approximately uniform across the core. The authors also performed flow visualization experiments in a water tunnel with dye injection to observe flow structures. Lastly, they recommended that model core geometries should always possess the same number of fin rows as the actual heat exchangers of interest to accurately recreate their flow patterns.

Manglik and Bergles (1995) reviewed past experimental data on fluid flow and heat transfer performance and proposed new correlations with the hope of surpassing existing ones. They sought to overcome some weaknesses of available correlations, such as the poor description of the transitional regime and the absence of some pertinent geometrical parameters in the equations. They also criticized some analytical models for either oversimplifying the problem or being too cumbersome for efficient use. The authors gathered a wide range of data and proposed a set of correlations based on the Reynolds

number and dimensions such as fin thickness, length, width, and spacing. Each correlation is composed of two formulas, one for each flow regime. They also proposed another correlation consisting of a single equation devised with an asymptote-matching technique in order to include all flow regimes. Their correlations predicted friction and heat transfer performance within 20% for the vast majority of data surveyed in their work, making it one of the most significant contributions in this field of research.

Dejong and Jacobi (1997) investigated the local convective effects in offset strip fin geometries. They used a sublimation technique on models installed in a wind tunnel to obtain local plate Sherwood numbers for three different geometries. Their results displayed the importance of vortex shedding on heat transfer performance. In steady flows, the maximum value of the local Sherwood number was observed at the leading edge of the fin, while in flows characterized by vortex shedding, it peaked at 20% of the fin length downstream from the leading edge. These distributions shed some light on the importance of flow mechanisms such as vortex shedding and boundary layer interruption. The authors also performed flow visualization experiments to relate observable flow structures with their local measurements. They were able to identify the position of the onset of vortex shedding, which started downstream and moved upstream with increasing Reynolds number.

Smotrys et al. (2003) investigated the potential of introducing vortex generators into offset strip-fin cores. They performed mass transfer measurements using a naphthalene sublimation technique to observe increases in heat transfer performance. These experiments were conducted in a wind tunnel on a model core for Reynolds numbers ranging from 400 to 3700. Two types of geometries were studied: two arrays with delta-wing type vortex generators attached to the first row of plates; and a baseline array used for comparison purposes. The authors presented data on the enhancement of the Sherwood number, which is clearly noticeable (up to 17%) for a good portion of the Reynolds number range. However, this increase in performance was found to be rather modest for a Reynolds number range of 1000 to 1600. Smotrys et al. also conducted flow visualization and PIV experiments to investigate flow structures in the spanwise and

streamwise directions. These additional investigations enabled the authors to assert that the performance drop observed in the transitional Reynolds number range is caused by the presence of destructive interactions between spanwise and streamwise vortices in the flow. Unfortunately, no data on the related increases in pressure drop of these enhanced cores was given.

Michna et al. (2005) investigated the performance of offset strip-fin heat exchangers in the high Reynolds number range (up to 120 000). They used a single modeled geometry in a special open-loop tunnel supporting pressures up to 6.8 atmospheres. Fanning friction factor distributions were obtained and compared with those obtained in past works, and also with those predicted by the correlation of Manglik and Bergles (1995). For Reynolds number values below 20 000, the experimental data is within 10% of the aforementioned correlation. Above that value, the friction factor distribution forms a plateau with slight oscillations, suggesting, according to the authors, a radically different flow regime. Mass transfer experiments were also conducted with a naphthalene technique. These data are presented in the form of a modified Colburn factor and are shown to be about twice the values predicted by the extrapolation of available correlations.

1.2.1.2 NUMERICAL INVESTIGATIONS

Sparrow, Baliga, and Patankar (1977) conducted one of the first numerical investigations of flows in offset-fin geometries. Their analysis assumed zero-thickness fins and two-dimensional laminar and steady flow. They used the boundary layer equations in which the streamwise diffusive terms were omitted, thus making the problem parabolic. The Prandtl number value was set to 0.7. The authors compared the offset-fin geometries with a parallel plate channel with continuous surfaces. As expected, both pressure drop and heat transfer increased with the presence of surface interruptions for the same Reynolds number and heat transfer area. Their investigation also included a heat transfer comparison of both geometries for a fixed pumping power: it showed appreciable improvements in performance (approximately 80%). When compared to experimental

data, the numerical analysis overpredicted heat transfer by 20 to 35% and underpredicted the friction factor by 10 to 20% for Reynolds numbers under 900. The authors attributed these deviations to the presence of burred edges on actual fins and the lack of fin thickness in their analysis. Still, such relatively good agreement is impressive considering the computing facilities and numerical methods available in those years. Finally, the analysis predicted the onset of a periodic fully-developed regime after the fifth row of fins.

Sparrow and Liu (1979) extended the work of Sparrow et al. (1977). In addition to staggered offset and parallel plate channels, they investigated the performance of in-line plate arrays. They provided basic heat transfer and pressure drop information and compared these results for all three geometry types. The superior performance of interrupted-surface geometries was confirmed once more by their results. The staggered plate array was shown to offer superior heat transfer performance for the same pumping power.

Patankar and Prakash (1981) investigated the effects of finite plate thickness on flows in offset-fin heat exchangers. The flow was assumed to be laminar and two-dimensional. The authors simplified the problem by exploiting the periodic fully-developed regime to their advantage, by imposing cyclic boundary conditions in the streamwise direction. They proposed a new pressure definition compatible with this cyclic domain and imposed a pressure gradient which induced the fluid motion. The thermal boundary condition was set so that the heat transfer was constant for each fin. This was achieved by increasing the temperature of a row of plates by the desired increment over that of the preceding row. Multiple plate thickness configurations were analyzed as well as different Reynolds number values. The flow fields were found to be quite complex, with recirculation zones near the trailing edges of the plates. Patankar and Prakash carefully reduced their data to compare their results with previous numerical analyses and available experimental data. They discovered that the finite plate thickness strongly increased the friction factor, by 10 to 16 times above the value found for zero-thickness plates. However, the Stanton number did not increase as much as the friction factor with the finite thickness plates (2.4

times for the thickest plate, $t/H = 0.3$). Finally, a comparison was made with the experimental data obtained by Kays and London (1964, 1984) on a geometrically similar core. While the friction factors agreed reasonably well, the Stanton number distributions significantly departed from the experimental heat transfer data. Unfortunately, the authors did not provide a complete explanation or state the possible causes of these discrepancies.

Suzuki et al. (1985) conducted complementary numerical and experimental studies of flows in vertical staggered plate arrays. They investigated the lower Reynolds number range (under 1000) in the mixed (free-forced) convection regime. In the numerical part of the work, two-dimensional flows developing across rows of plates were investigated. Two methods were used to tackle the elliptic problem. The streamline and vorticity method were implemented and compared to the “primitive variables” method, which yielded almost identical results. The authors performed an experimental investigation on an analogous model array and gathered local Nusselt numbers for comparison. The numerical models accurately predicted their experimental measurements. The effects of upstream turbulence were also considered and found to have little impact on heat transfer results. The numerical model was tested against experimental data obtained from two actual geometries by Kays and London (1964, 1984). The numerical predictions agreed poorly with the benchmark experimental data, but still displayed a qualitative agreement. Lastly, the authors numerically investigated the effects of geometric parameters and recommended thin fins, since the modest heat transfer gains caused by added fin thickness are generally spoiled by the larger increases in pressure drop.

Kelkar and Patankar (1989) studied steady laminar flows in offset strip fin geometries. Their numerical study was three-dimensional and investigated the developing region from the entrance to the fully-developed regime. The fin thickness was assumed to be negligible, thus justifying the use of a parabolic method in the streamwise direction. All surfaces were maintained at a fixed temperature. Their results showed that the flow development length varied from 5 to 10 modules. The authors also investigated a wide range of geometric parameters that influence heat transfer performance.

Zhang et al. (1997) performed numerical analyses of flows in parallel-plate fin heat exchangers. Using powerful computers and parallel computing techniques, they demonstrated the importance of including unsteady effects and three-dimensionality to obtain adequate predictions. The computational domain was limited to a single geometric module in the fully developed region. Thus, cyclic boundary conditions were used, as suggested by Patankar and Prakash (1981). Grid independence checks were performed as well as processing performance studies. As expected, both the steady and unsteady solutions diverged with increasing Reynolds number. Additionally, the authors compared their unsteady solutions with the experimental data of Mullisen and Loehrke (1986). While the steady simulations departed from the experimental results once unsteadiness appears, the unsteady analyses agreed quite well for both friction and Colburn factors. Finally, they showed that intrinsic three-dimensional effects should not be neglected for Reynolds number values past the transitional range.

Saidi and Sundén (2001) recently investigated unsteady and two-dimensional flows in offset-fin geometries. The flow problem was simplified by using cyclic conditions across a single module in the fully-developed regime. Their objective was to shed some light on the physical phenomena involved in the heat transfer process. They used an established finite volume method along with a very fine grid and focused their efforts on a single geometric configuration. First, the friction factor and Colburn factors were compared to the experimental results of DeJong et al. (1998), and the deviations were found to be in the range of 6 to 8 percent. With these results providing new confidence in their method, they observed flow mechanisms such as circulation bubbles commuting along the fins and the absence of a classic boundary layer structure over the plates. The authors also found that the velocity field had an oscillatory motion (at $Re = 993$) that was not chaotic in appearance.

1.2.2 INVESTIGATIONS OF FLUID FLOW AND HEAT TRANSFER IN MODEL INTERRUPTED-SURFACE DUCTS

1.2.2.1 EXPERIMENTAL INVESTIGATIONS

Cur and Sparrow (1978) investigated airflows in a rectangular duct with two plates aligned along the centerline. Pressure drop measurements were taken in addition to mass transfer measurements with a naphthalene sublimation technique. Another objective of the study was to isolate the effects of the mass transfer from the first plate on that from the second one. Sherwood numbers were provided for both plates for Reynolds numbers between 1000 and 14000. Multiple plate thicknesses and plate spacing were tested. The authors noted that heat transfer performance gains caused by thickening the plates are accompanied by a larger increase in pressure drop.

Cur and Sparrow (1979) aimed to surpass their previous efforts (1978) by performing experiments on airflows in a rectangular duct with numerous rows of collinear plates. Their objective was to prove the existence of a thermally developed condition in interrupted geometries. Again, a naphthalene sublimation technique was used to measure Sherwood numbers (Sh) for each plate and then infer the corresponding Nusselt numbers using the heat-mass transfer analogy. They tested three different plate thicknesses and obtained data for Reynolds numbers ranging from 1100 to 13600. The reduced data, in the form of $Sh/Sc^{0.4}$, was presented concisely in three figures showing the effect of Reynolds number and plate thickness. Once more, increasing fin thickness induced higher mass (heat) transfer. The thermally fully developed regime was shown to prevail within eight plates, making this investigation the first experimental demonstration of its existence.

Sparrow and Hajiloo (1980) have also carried out an investigation of flows in interrupted-plate ducts. In this particular study, the duct contained an array of staggered plates arranged in five columns, each composed of ten plates. Three plate thicknesses were tested over a Reynolds number range of 1000 to 9000. Once more, a naphthalene

sublimation technique was employed to gather plate Sherwood numbers. The presence of a spatially-periodic fully-developed regime was observed as expected. The Sherwood number (and the analogous Nusselt number) increased with the Reynolds number for all cases. Plate thickness also increased mass (heat) transfer for most cases. The authors compared their results with correlations in the literature, such as the one provided by Wieting (1975). The data scatter about the predictions obtained with the correlations was around 15 to 20 %. These deviations were explained by differences in geometry, such as aspect ratio and number of columns. In addition to the mass transfer data, friction factors were obtained for the duct. Curiously, the friction factors became constant at high Reynolds values while Wieting's correlation predicted a downward trend in that range.

Roadman and Loehrke (1983) studied regime transition of flows between a pair of plates. They varied geometric parameters such as plate thickness and spacing. Dye visualization along with hot film anemometry was used in a water channel to determine transition thresholds. Experiments were also conducted in a wind tunnel with hot-wire anemometry. They found that the critical velocity corresponding to the triggering of transition varied strongly with plate spacing for small plate gaps. However, this transitional velocity was independent of plate spacing if the plate interval was large. Surprisingly, the transition point was found to be insensitive to the level of free stream turbulence.

Zelenka and Loehrke (1983) extended the experiments of Roadman and Loehrke (1983) by investigating heat transfer from two collinear plates. These authors studied the effects of plate edge bluntness, plate spacing, and Reynolds number. Heating elements were inserted into the plates and copper-constantan thermocouples were used to monitor their temperatures. As expected, heat transfer from a single blunt plate depended on its length and thickness. Blunt leading edges at low Reynolds numbers were found to inhibit plate heat transfer due to the presence of separation bubbles. Such structures were absent for flows around a single plate with round edges. At higher Reynolds number, heat transfer was enhanced by the turbulence generated in the separated leading edge shear layer. For large plate spacings, the heat transfer from the second plate was independent of the edge bluntness of the first plate and was solely influenced by its unstable wake. This flow

structure enabled the heat transfer coefficient on second plate to approach and even surpass that on the first one. Finally, the shape of the second plate only influenced the heat transfer from it if the inter-plate spacing and Reynolds number were high.

McBrien and Baliga (1988) studied flows in interrupted-plate ducts in order to better understand the flow complexities and characteristics found in actual heat exchanger cores. They investigated a relatively high Reynolds number range (from 5000 to 45000) and six different geometric configurations. One of the objectives of this contribution was to fill the need for local intramodular flow measurements. Numerous pressure taps on the top wall of the duct enabled the authors to obtain locally precise time-mean wall static pressure distributions in the spatially-periodic fully-developed region. These distributions were plotted and used to calculate modular friction factors. Their results shed some light on the flow mechanisms affecting pressure drop and provided useful data to validate numerical models. The existence of a spatially periodic fully-developed region was confirmed in this model geometry.

Sekulic (1989) conducted experimental investigations of flows in interrupted-plate ducts. The main interest of this research was to monitor flow transition between the laminar and turbulent regimes. The author used three different core arrangements: two interrupted-plate geometries and a continuous plate configuration for comparison. Overall friction factors were obtained and plotted for the three test cases for Reynolds number values ranging from 1000 to 4000. As expected, the presence of the plates increased the pressure drop. Though the findings of this research did not bring forth new fundamental understanding of such flows, it offered additional test data and further insights on flow regime transition.

McBrien et al. (2000) performed an experimental study of flows in interrupted-plate ducts. The objectives of this work were to provide detailed time-mean wall static pressure distributions along with module friction factors as function of Reynolds number. The authors investigated two different geometric configurations for turbulent flows with Reynolds numbers ranging from 1700 to 35000. Intramodular pressure distributions were

plotted as functions of duct streamwise position to determine module friction factors. Additionally, flow visualization experiments were conducted with the use of paints to investigate plate-surface streakline patterns. The results showed that the time-mean flow was two-dimensional over 80% of the plates in the spanwise direction. They also confirmed the existence of flow separation and recirculation at the plate leading edge. The trailing edge zone was believed to be a region of low shear or flow reversal and separation probably caused by oscillating wakes.

Candanedo et al. (2003) carried out experimental investigations of flows in interrupted-plate ducts. They provided additional time-mean wall static pressure distributions and module friction factors for a wide range of Reynolds numbers and additional geometrical configurations. Candanedo (2003) extended this research and redesigned the apparatus at McGill University to improve its repeatability and accuracy. With this new test rig, wall static pressure distributions were measured as well as friction factors for a wide range of Reynolds number and geometrical parameters. Finally, the authors developed a generalized correlation predicting module friction factors as functions of the Reynolds number.

Lamoureux et al. (2005) extended the work of Candanedo (2003) by performing single hot-wire measurements of flows in interrupted-plate ducts. Turbulence power spectrums were provided for many different locations in the duct for a wide range of Reynolds number. Dimensionless vortex shedding frequencies were also presented in the form of Strouhal numbers. This contribution constitutes the experimental part of this thesis and will be explained further in the following chapters.

1.2.2.2 NUMERICAL INVESTIGATIONS

Amon and Mikic (1990) performed numerical investigations of flows in grooved channels and interrupted-plate ducts. The analysis was two-dimensional and included unsteady effects. The authors studied laminar flows with self-sustained oscillations and their critical onset Reynolds number (Re_c). The time discretization was performed with a multistep fractional scheme. The convective terms were discretized with a third-order

Adams-Bashforth scheme while the pressure and diffusion effects were treated with the Euler backward scheme or Crank-Nicolson scheme. A spectral element method was chosen to discretize the governing equations in space. The problem was simplified by studying the periodic fully-developed region and by limiting the domain to a single module with axial cyclic conditions. Solutions were obtained by marching in time until a stable or unsteady flow prevailed. The critical Reynolds number at which unsteadiness appears was evaluated at 110. After this threshold, periodic oscillations appeared and heat transfer increased significantly. This periodic regime was considered advantageous since it required less pumping power to provide the same heat transfer performance. Finally, it was shown that heat transfer increased up to three times for the same pumping power in interrupted-plate ducts when compared to continuous flat channels.

Amon et al. (1992) pursued the investigations of Amon and Mikic (1990) by performing numerical and experimental studies of flows and heat transfer in interrupted-plate ducts. Attention was focused on regime transition and the oscillatory phenomena present in the flow. The experimental apparatus was composed of ten plates, each heated with an electric foil controlled with DC power inputs. Holographic interferometry was used to visualize instantaneous temperature fields. A spectral numerical method, almost identical to the one used by Amon and Mikic (1990), was used to simulate two-dimensional unsteady laminar flows. Flows prevailing in the spatially periodic fully-developed region were simplified with the use of a cyclic boundary in the streamwise direction. Reynolds numbers ranging between 100 and 400 were investigated with this numerical method. The onset of periodic oscillations appeared between Re values of 150 and 200. This unsteadiness threshold value was evaluated to be around $Re = 200$ in the experiments, thus corroborating the numerical predictions. As expected, predicted and actual heat transfer performance increased with the presence of flow oscillations. This enhancement was explained with temperature visualization interferograms. They revealed that the unsteady flows had thinner boundary layers and enhanced mixing due to vortex shedding. The results of this numerical investigation were presented again by Majumdar and Amon (1992) in another journal paper which also included new local Nusselt number

distributions, phase-plane velocity plots, and an analysis of Reynolds stresses and turbulent heat fluxes.

Suzuki et al. (1994) performed numerical investigation of flows in interrupted-plate ducts in order to examine the mechanisms responsible for heat transfer enhancement in such geometries. Attention was focused on two-dimensional laminar and unsteady flows in the middle Reynolds number range, where self-sustained periodic flows oscillations occurred. The computational domain included three consecutive plates. Uniform velocity and temperature profiles were imposed at the duct inlet. A two-level multi-grid method was used to speed up convergence. The diffusive terms were treated with a central difference scheme, while the convective contributions were modeled with the QUICK scheme of Leonard (1979). The fully-implicit scheme was chosen to treat the temporal effects. The authors presented overall Colburn factors, local Nusselt number distributions, plots of Reynolds stresses, maps of vorticity, and instantaneous velocity vectors maps. Their results showed that the vortices enhanced heat transfer by mixing the temperature excess of the wake with the main stream flow and drawing cool fluid toward the hot plates.

Grosse-Gorgemann et al. (1995) carried out numerical investigations of flows in interrupted-plate ducts and other geometries. A numerical code, based on the SIMPLEC procedure of Van Doormal and Raithby (1984), was used to solve two-dimensional unsteady flow fields. The authors provided Strouhal numbers and validated their results with hot-wire measurements obtained in a complementary experimental study. The computed Strouhal numbers showed very good agreement with those obtained from the measurements ($St_{exp} = 0.19$ and $St_{num} = 0.20$).

Sebben (1996) performed numerical studies of flows in interrupted-plate rectangular ducts. Attention was focused on the laminar regime as well as the intermediate Reynolds number turbulent regime. The author used a finite volume method to solve unsteady two-dimensional flows across axially periodic domains containing up to six geometric modules. Her study revealed the existence of multiple stable solutions, a major finding of

this work. In order to solve the turbulent flow problems, several different turbulence models were explored. However, the predictions in the turbulent regime, such as time-mean friction factors and Strouhal numbers, only followed the behavior of the experimental data of McBrien and Baliga (1988) and did not compare well quantitatively.

Valencia (1999) conducted numerical investigations of flows in a geometry similar to the interrupted-plate duct: a channel with periodically mounted transverse vortex generators. These vortex generators are thick plates (spanning half the height of the channel) of short length in the main flow direction. Flow and heat transfer data were obtained for different values of the plate spacing for a Reynolds number range of 100-400. The problem was simplified by imposing periodic conditions over a single module. Temperature was set constant on the channel walls and the temperature of the plate was not fixed. The control volume formation employed in this work was inspired by the works of Patankar (1980) and incorporated the SIMPLEC scheme along with line Gauss-Seidel solvers based on the tri-diagonal matrix algorithm (TDMA). Flow unsteadiness appeared at $Re = 150$ and a single dominant vortex shedding frequency was observed up to $Re = 200$. At a Reynolds number of 300, an additional frequency appeared and both prevailed equally at $Re = 400$. Nusselt number plots and friction factors were provided. Finally, it was shown that ordered oscillatory flows required less pumping power than turbulent ones for the same heat transfer performance. The author explained this observation by stating that laminar self-sustained oscillatory flows induce less viscous dissipation than the ones characterized by random chaotic turbulent structures, and thus require less pumping power to yield the same transport rates.

1.2.3 TEXTBOOKS, REVIEW ARTICLES, AND OTHER CONTRIBUTIONS

The work of Kays and London (1964, 1984) is pivotal in the field of compact heat exchangers. These authors presented a wide range of experimental data on pressure losses and heat transfer performance for many different compact heat exchanger cores. In a

recent book by Hesselgreaves (2001), design methodologies for compact heat exchangers and correlations for pressure losses and heat transfer in modern cores are presented. This book includes discussions on various types of geometry along with their respective advantages and drawbacks. Shah et al. (2001) have presented a comprehensive review of past computational studies of fluid flow and heat transfer in compact heat exchanger cores along with a presentation of potential challenges awaiting researchers in this field.

Numerical methods used for the prediction of fluid flow and heat transfer in heat exchangers are described in books authored by Roache (1976), Patankar (1980), Reddy and Gartling (1994), and Ferziger and Peric (1996, 1999), among others. Other important works presenting review articles on numerical methods include the following: *The Handbook of Numerical Heat Transfer* edited by Minkowycz, Sparrow, Schneider and Pletcher (1988), and the *Advances in Numerical Heat Transfer* series, edited by Minkowycz and Sparrow (1997, 2000).

Fundamental and practical notions about fluid flow and heat transfer related to heat exchangers are presented in several textbooks. Some of the key books on these topics include those written by the following authors: Rouse (1946, 1978), Streeter (1951, 1962), Schlichting (1955, 1968, 1979), Landau and Lifshitz (1959, 1987), Bird et al. (1960, 2002), Batchelor (1967), Eckert and Drake (1971), White (1974, 1991), Currie (1974, 2003), Kays and Crawford (1980, 1993), Incropera and DeWitt (1981, 2002), Bejan (1984, 1995), Fox and McDonald (1985, 1998), Churchill (1988), Panton (1996), Wilkes (1999), and Cebeci (2002). Shah and London (1978) have provided numerous reviews of works on laminar flow and heat transfer in ducts. Finally, the *Handbook of Heat Transfer Fundamentals* edited by Rohsenow et al. (1985) has become a classic as an extensive source information on these topics.

Numerous experimental and numerical investigations have been performed on other types of heat exchanger core geometries, such as grooved channels, passages with louvered fins, and wavy channels. However, for the sake of conciseness, attention in this review was limited to geometries akin to those investigated in this work. Some of these other

contributions include the following works: Greiner (1991), Kim and Anand (1994), and Grosse-Gorgemann (1995), all on grooved channels; and Blancher et al. (2004), on the stability of flows in wavy channels.

1.3 SPECIFIC OBJECTIVES

This work is divided into two parts: experimental investigations of turbulent flows in rectangular interrupted-plate ducts; and numerical studies of unsteady, two-dimensional, laminar flows in staggered-plate arrays, akin to those encountered in offset-fin cores of compact heat exchangers. The specific objectives of this work are summarized below.

The aims of the experimental investigations are the following:

- Modify an available rectangular interrupted-plate duct, akin to that shown in figure 1.3, in order to incorporate a section suitable for single hot-wire measurements in the spatially periodic fully-developed flow region.
- Benchmark the hot-wire probe and anemometer, and confirm the repeatability of the related measurements.
- Investigate the spatial periodicity of the turbulence statistics at multiple streamwise locations and examine the two-dimensionality of these statistics across the width of the duct.
- Obtain ensemble-averaged power spectrums at multiple locations in the duct and for a Reynolds number range of 2000 to 30000. Obtain Strouhal numbers of the principal vortex frequencies by analyzing the power spectrums.

The objectives in the numerical investigation are the following:

- Develop a finite volume method (FVM) to simulate laminar, unsteady, two-dimensional flows of a Newtonian fluid. Implement the QUICK scheme along with appropriate iterative solvers, and design the computer program to solve unsteady problems with multiple time integration schemes in cyclic and regular domains.

- Validate the proposed FVM method with two test cases: (1) steady flows in staggered plate arrays; and (2) unsteady unconfined flows past a square cylinder.
- Investigate unsteady, laminar, two-dimensional, developing flows in a rectangular interrupted-plate duct. Provide modular time-averaged friction factors and vortex shedding Strouhal numbers.
- Investigate unsteady, laminar, two-dimensional flows and heat transfer in staggered plate arrays, representing offset-fin heat exchanger cores. Conduct time and grid independence studies. Obtain module time-averaged friction factors, Colburn factors, and vortex shedding Strouhal numbers for multiple geometric configurations and a Reynolds number range of 100 to 600. Investigate the effects of the multiple plate rows in the cyclical domain.

The numerical investigation is limited to two-dimensional, laminar, Newtonian fluid flows, as the corresponding mathematical models are well established and the computational costs are quite reasonable. On the other hand, the experiments are focused on turbulent Newtonian fluid flows, as the mathematical models are still not well established, and reliable experimental data are urgently needed to check and refine available models.

1.4 THESIS OVERVIEW

The motivation behind this work was presented in this first chapter, along with the objectives and a concise review of past research contributions in the field of compact heat exchangers. Theoretical aspects relevant to the experimental and numerical parts of this work are presented and discussed in chapter 2. In chapter 3, the apparatus used in the experimental part of this work and the test methodology are described concisely. The formulation of the numerical method employed in the computational studies is presented in chapter 4. The experimental and numerical results are presented and discussed chapter 5. Lastly, in chapter 6, the contributions of this work are summarized and suggestions are made for its extensions.

CHAPTER 2 – THEORETICAL CONSIDERATIONS

The theoretical considerations relevant to the experimental and numerical parts of this thesis, such as the governing equations, the description of the spatially periodic fully-developed regime, the definition of ensemble-averaged power spectrums and related Strouhal numbers, and the other nondimensional parameters used in this work, are presented in this chapter.

2.1 GOVERNING EQUATIONS

In this thesis, the working fluid is considered to be Newtonian and incompressible, and its thermophysical properties are assumed to remain essentially constant at suitably averaged values.

In the problems of interest, the Mach numbers are all well below 0.1, so the assumption of incompressible fluid is quite valid. In the experimental part of this work, the fluid temperature was almost constant and the pressure drops were relatively minor compared to the values of average absolute static pressure in the ducts, thus justifying the assumption regarding constant fluid properties. It is also common in heat exchanger design practice to peg the fluid thermophysical properties to average values corresponding to mean values of the bulk temperature and the static pressure, and assume that these average properties remain essentially constant, at least in the first pass of the design process; corrections to account for the variations of the fluid properties are incorporated in the second pass of the design process, if needed. Furthermore, the values of the Eckert number for the flows of interest are all much less than one (unity), so the viscous dissipation is considered negligible.

The governing equations are presented in this section in the context of the above-mentioned assumptions. Furthermore, as the focus in the work is primarily on flow in rectangular geometries, the governing equations are presented with respect to the Cartesian coordinate system shown in Figure 1.3.

2.1.1 GENERAL FORM OF GOVERNING EQUATIONS

The continuity equation for an incompressible fluid is expressed as follows:

$$\frac{\partial u}{\partial x} + \frac{\partial v}{\partial y} + \frac{\partial w}{\partial z} = 0 \quad (5.1)$$

The gravitational body forces are included in a reduced static pressure. It is also assumed (with no real loss in generality) that the gravitational acceleration vector is directed in the negative x direction. Thus, the reduced pressure is defined as follows:

$$p = p_{static} + \rho g (x - x_{reference}) \quad (5.2)$$

In this equation, g is the gravitational acceleration; and it is assumed to remain constant in the problems of interest.

Using the reduced pressure defined in equation (2.2), the Navier-Stokes (momentum) equations can be expressed as follows:

$$\rho \left(\frac{\partial u}{\partial t} + u \frac{\partial u}{\partial x} + v \frac{\partial u}{\partial y} + w \frac{\partial u}{\partial z} \right) = -\frac{\partial p}{\partial x} + \mu \left(\frac{\partial^2 u}{\partial x^2} + \frac{\partial^2 u}{\partial y^2} + \frac{\partial^2 u}{\partial z^2} \right) \quad (5.3)$$

$$\rho \left(\frac{\partial v}{\partial t} + u \frac{\partial v}{\partial x} + v \frac{\partial v}{\partial y} + w \frac{\partial v}{\partial z} \right) = -\frac{\partial p}{\partial y} + \mu \left(\frac{\partial^2 v}{\partial x^2} + \frac{\partial^2 v}{\partial y^2} + \frac{\partial^2 v}{\partial z^2} \right) \quad (5.4)$$

$$\rho \left(\frac{\partial w}{\partial t} + u \frac{\partial w}{\partial x} + v \frac{\partial w}{\partial y} + w \frac{\partial w}{\partial z} \right) = -\frac{\partial p}{\partial z} + \mu \left(\frac{\partial^2 w}{\partial x^2} + \frac{\partial^2 w}{\partial y^2} + \frac{\partial^2 w}{\partial z^2} \right) \quad (5.5)$$

The experimental investigation reported in this thesis does not involve heat transfer, but the numerical studies do. Therefore, the energy equation is presented below in the context of the assumptions stated earlier:

$$\rho c_p \left(\frac{\partial T}{\partial t} + u \frac{\partial T}{\partial x} + v \frac{\partial T}{\partial y} + w \frac{\partial T}{\partial z} \right) = k \left(\frac{\partial^2 T}{\partial x^2} + \frac{\partial^2 T}{\partial y^2} + \frac{\partial^2 T}{\partial z^2} \right) \quad (5.6)$$

2.1.2 GOVERNING EQUATIONS FOR NUMERICAL INVESTIGATIONS

In the numerical studies presented in this thesis, only unsteady two-dimensional fluid flow and heat transfer problems are considered in the context of the assumptions stated earlier. Furthermore, in the numerical investigations, the x axis is taken to coincide with the main flow direction and y axis is oriented in the vertically upward direction (the gravitational acceleration vector is now directed in the negative y direction). Thus, the following simplified versions of the continuity, x - and y -momentum, and energy equations apply in the numerical part of this work:

$$\frac{\partial u}{\partial x} + \frac{\partial v}{\partial y} = 0 \quad (5.7)$$

$$\rho \left(\frac{\partial u}{\partial t} + u \frac{\partial u}{\partial x} + v \frac{\partial u}{\partial y} \right) = -\frac{\partial p}{\partial x} + \mu \left(\frac{\partial^2 u}{\partial x^2} + \frac{\partial^2 u}{\partial y^2} \right) \quad (5.8)$$

$$\rho \left(\frac{\partial v}{\partial t} + u \frac{\partial v}{\partial x} + v \frac{\partial v}{\partial y} \right) = -\frac{\partial p}{\partial y} + \mu \left(\frac{\partial^2 v}{\partial x^2} + \frac{\partial^2 v}{\partial y^2} \right) \quad (5.9)$$

$$\rho c_p \left(\frac{\partial T}{\partial t} + u \frac{\partial T}{\partial x} + v \frac{\partial T}{\partial y} \right) = k \left(\frac{\partial^2 T}{\partial x^2} + \frac{\partial^2 T}{\partial y^2} \right) \quad (5.10)$$

2.2 DESCRIPTION OF THE SPATIALLY PERIODIC FULLY-DEVELOPED REGIME

2.2.1 GENERAL DEFINITION

Flows in geometries with multiple repetitive modules, such as offset-fin cores of compact heat exchangers (see Figure 1.1) and rectangular interrupted-plate ducts (see Figure 1.3), develop in the streamwise direction and could, if the flow passage is long enough, reach a

fully-developed state. However, since the geometry itself varies in the flow direction (albeit in a spatially periodic manner), the classical fully-developed concept of invariance of the velocity field in the main flow direction, does not apply to such flows. Rather, such flow can reach what is called as a spatially periodic fully-developed state, a concept first postulated in a numerical study by Sparrow et al. (1977). This spatially periodic fully-developed regime is established after a sufficient number of geometric modules downstream from the inlet of interrupted-surface flow passages and is characterized by the following features [Sparrow et al. (1977); Patankar et al. (1977); McBrien and Baliga (1988)]: the time-mean velocity field repeats identically in each geometrically similar module in the flow direction; and the time-mean static pressure *drop* between similar locations in adjacent geometrically similar modules becomes constant. If the length of the spatial period of a single module is denoted Λ and z is the streamwise direction (with respect to Figure 1.3, for example, $\Lambda = L + s$), then the time-mean velocity field in the spatially periodic fully-developed region displays the following properties:

$$\langle u \rangle(x, y, z) = \langle u \rangle(x, y, z + \Lambda) = \langle u \rangle(x, y, z + 2\Lambda) = \langle u \rangle(x, y, z + 3\Lambda) = \dots \quad (5.11)$$

$$\langle v \rangle(x, y, z) = \langle v \rangle(x, y, z + \Lambda) = \langle v \rangle(x, y, z + 2\Lambda) = \langle v \rangle(x, y, z + 3\Lambda) = \dots \quad (5.12)$$

$$\langle w \rangle(x, y, z) = \langle w \rangle(x, y, z + \Lambda) = \langle w \rangle(x, y, z + 2\Lambda) = \langle w \rangle(x, y, z + 3\Lambda) = \dots \quad (5.13)$$

In this equation set, the brackets $\langle \rangle$ denote time-mean values. As was mentioned above, the drops in time-mean static pressure values between similar locations in adjacent geometric modules (separated by the spatial period Λ in the z direction) are equal, as indicated in the following equation:

$$\begin{aligned} \langle p \rangle(x, y, z) - \langle p \rangle(x, y, z + \Lambda) = \\ \langle p \rangle(x, y, z + \Lambda) - \langle p \rangle(x, y, z + 2\Lambda) = \\ \langle p \rangle(x, y, z + 2\Lambda) - \langle p \rangle(x, y, z + 3\Lambda) = \dots \end{aligned} \quad (5.14)$$

It is also useful to formulate a modular gradient of the time-mean static pressure as follows:

$$\beta = \frac{\langle p \rangle(x, y, z) - \langle p \rangle(x, y, z + \Lambda)}{\Lambda} \quad (5.15)$$

This time-mean modular static pressure gradient can be measured experimentally or obtained numerically (for flows amenable to computational studies) and presented in the form of modular friction factors.

The spatial period Λ is specific to the problem being investigated. For the rectangular interrupted-plate duct shown in Figure 1.3, this spatial period Λ is equal to the sum of a single plate length (L) and the inter-plate spacing (s): $\Lambda = L + s$. In the case of offset-fin core of a compact heat exchanger, a module includes a set of two successive (staggered) plates in the flow direction, thus the spatial period Λ is defined as twice the plate length (L): $\Lambda = 2L$.

The existence of such a spatially periodic fully developed regime has been confirmed for offset-fin geometries and rectangular interrupted-plate ducts in several numerical and experimental investigations. Such investigation include the works of Patankar et al. (1977), Patankar et al. (1981), Kelkar et al. (1989), Sparrow and Hajiloo (1980), Mullisen and Loehrke (1986), and McBrien and Baliga (1988).

A spatially periodic fully-developed thermal regime can also be defined for flow and heat transfer in interrupted-surface geometries [Patankar et al (1977); Patankar and Prakash (1981)]. However, since multiple thermal boundary conditions can lead to the establishment of such a spatially periodic thermal regime (such as constant plate temperature or constant plate heat transfer), the definition of the spatially periodic thermal regime must be compatible with the problem being considered. For example, this regime can be tied to the establishment of a constant modular heat transfer coefficient at a certain point downstream from the inlet; or it could be characterized by self-similar temperature profiles in successive modules. For additional details, the reader is referred to the works of Patankar et al. (1977) and Patankar and Prakash (1981).

2.2.2 GOVERNING EQUATIONS FOR SPATIALLY PERIODIC FULLY-DEVELOPED LAMINAR TWO-DIMENSIONAL STEADY FLOWS

Spatially-periodic fully-developed steady flows can be analyzed with reference to just one geometrically similar module, with suitable cyclic boundary conditions, as described in the pioneering work of Patankar et al. (1977). While this strategy is quite straightforward for time-mean velocity components, the treatment of pressure requires special attention. Due viscous and inertial losses, pressure has to inevitably drop from the inlet plane of a module to its exit. Thus, the pressure itself does not submit to the cyclic boundary condition. However, as was stated earlier, the modular time-mean pressure drop becomes constant in the spatially fully-developed region. Advantage can be taken of these characteristics to propose a mathematical model limited to just one geometric module. In this section, such a mathematical model is proposed for spatially periodic fully-developed laminar *two-dimensional steady* flows, in preparation for some aspects of the numerical studies presented later in this thesis.

Following Patankar et al. (1977), the pressure field in spatially periodic fully-developed laminar *two-dimensional steady* flows can be decomposed into two parts: one of which is a linear function of the streamwise coordinate (denoted by x in the two-dimensional problems considered in this thesis), and a function that repeats periodically in successive modules. Thus:

$$p(x, y) = -\beta x + \tilde{p}(x, y) \quad (5.16)$$

The spatially periodic portion of the pressure field, $\tilde{p}(x, y)$, respects the following equation:

$$\tilde{p}(x, y) = \tilde{p}(x + \Lambda, y) = \tilde{p}(x + 2\Lambda, y) = \dots \quad (5.17)$$

This treatment for pressure is used to obtain the following forms of the continuity and steady momentum equations:

$$\frac{\partial u}{\partial x} + \frac{\partial v}{\partial y} = 0 \quad (5.18)$$

$$\rho \left(u \frac{\partial u}{\partial x} + v \frac{\partial u}{\partial y} \right) = \beta - \frac{\partial \tilde{p}}{\partial x} + \mu \left(\frac{\partial^2 u}{\partial x^2} + \frac{\partial^2 u}{\partial y^2} \right) \quad (5.19)$$

$$\rho \left(u \frac{\partial v}{\partial x} + v \frac{\partial v}{\partial y} \right) = -\frac{\partial \tilde{p}}{\partial y} + \mu \left(\frac{\partial^2 v}{\partial x^2} + \frac{\partial^2 v}{\partial y^2} \right) \quad (5.20)$$

The x -momentum equation given above now has an extra source term, β . Two strategies are commonly used to handle this situation: in one, β is treated as a specified parameter and the above-mentioned governing equations are solved for u , v , and \tilde{p} ; in the other, the overall mass flow rate is prescribed, and u , v , \tilde{p} , and β are calculated by solving the three governing equations given above, in conjunction with the overall continuity equation: $\dot{m} = \rho u_{av} A_{c.s.} = \dot{m}_{specified}$. The first of these strategies produces a velocity field (hence, an overall mass flow rate) in response to the specified value of β ; the second strategy allows the calculation of β that is consistent with the specified mass flow rate.

The temperature field also requires a special treatment. Like pressure, temperature values across the cyclic boundary are not equal if heat transfer is present in the domain. The solution was again proposed by Patankar et al. (1977) and also by Patankar and Prakash (1981). It consists of a decomposition of the temperature field into a linearly increasing term and a periodically varying part. In this particular treatment, the thermal boundary conditions were set to simulate constant plate heat transfer. This was accomplished by fixing the temperature of a plate row to uniform values. Each plate row temperature was increased by ΔT above the preceding upstream plate row value. Therefore, in the spatially periodic fully-developed region, the fluid bulk temperature also increases by the same increment over each plate length (L). Thus, for this specific problem, the temperature is expressed as:

$$T(x, y) = \left(\frac{x}{L}\right)\Delta T + \tilde{T}(x, y) \quad (5.21)$$

The fluctuating part $\tilde{T}(x, y)$ is periodic and repeats itself in each successive module in the fully-developed region. This decomposed temperature field can now be introduced into the energy equation, yielding:

$$\rho c_p \left(u \frac{\partial \tilde{T}}{\partial x} + v \frac{\partial \tilde{T}}{\partial y} \right) = -\rho c_p u \left(\frac{\Delta T}{L} \right) + k \left(\frac{\partial^2 \tilde{T}}{\partial x^2} + \frac{\partial^2 \tilde{T}}{\partial y^2} \right) \quad (5.22)$$

The strategy for solving the temperature field is analogous to that used to solve the pressure field.

2.3 ENSEMBLE AVERAGED POWER SPECTRUM AND STROUHAL NUMBERS

As was stated earlier, the objective in the experimental investigation is to undertake single hot-wire measurements in a rectangular interrupted-plate duct (see Figure 1.3) and use the data collected to obtain turbulence power spectrums and Strouhal numbers for the flows of interest. In this work, this experimental data was collected by inserting a single hot-wire probe in the spatially periodic fully-developed region. The hot wire was maintained perpendicular to the main-flow direction (z) and parallel to the y direction (see Figure 1.3). The probe measured the instantaneous velocity perpendicular to its axis, denoted here as v , and such measurements were carried out at multiple spatial locations in the duct. Details of these hot-wire measurements locations are provided in chapter 3. The hot-wire measurements provided blocks of data, which were processed to obtain the power spectrums and Strouhal numbers.

First, the velocity fluctuation, v' , about the time-mean value, \bar{v} , is computed:

$$v' = v - \bar{v} \quad (5.23)$$

A Fourier transform is then applied to the velocity fluctuation, as follows:

$$H(f) = \int_{-\infty}^{\infty} v'(t) e^{-2\pi ift} dt \quad (5.24)$$

Here, f is the frequency in Hz, and $H(f)$ is the Fourier transform of a single block of 8192 samples (hot-wire measurements) taken at 10 000 Hz. A fast Fourier transform (FFT) was used along with Hann windowing to compute $H(f)$ using the hot-wire measurements [Press et al. (1992)]. The power spectrum was computed as follows:

$$PSD_m(f) = \left[\sum_{block=1}^{100} \frac{2}{\Delta t_{block}} |H_{block}(f)|^2 \right] \div 100 \quad (5.25)$$

The power spectrum presented above is obtained by performing an ensemble-average of a 100 blocks of sample data. In Eq. (2.25), Δt_{block} is the total sampling time of a single sample data block. This power spectrum respects the one-side power spectral density convention, thus explaining the presence of the multiplying factor of 2 in the equation.

Depending on the hot-wire (sampling) spatial position, dominant vortex shedding frequencies are revealed in the form of peaks when the power spectrums are plotted against frequency. This dominant or main frequency, denoted as f_v , was determined by applying a least-squares fit of a ninth-order polynomial to a sufficient number of data points in the vicinity of the peak in the power spectrum of interest: the frequency is determined from the local maximum of this polynomial function. If two spikes are visible in the power spectrum, the first (dominant) one is chosen as the main frequency. This primary frequency is then used to obtain the corresponding Strouhal number as follows:

$$St = \frac{f_v(2t)}{\bar{W}} \quad (5.26)$$

The Strouhal number is based on the plate thickness ($2t$) and \bar{W} , the average z -direction velocity at the minimum cross-sectional area of the duct. In the next section, other dimensionless variables, parameters, and results relevant to this work are discussed.

2.4 DIMENSIONLESS PARAMETERS

The dimensionless variables, parameters, and results relevant to the numerical and experimental parts of this work are described in this section.

2.4.1 DIMENSIONLESS PARAMETERS PERTAINING TO EXPERIMENTS IN RECTANGULAR INTERRUPTED-PLATE DUCTS

In the experimental studies of flows in the rectangular interrupted-plate duct shown in figure 1.3, for a given geometry, the dimensionless parameter is the Reynolds number. This Reynolds number is based on the average time-mean velocity in the streamwise direction at the minimum cross-sectional area (\bar{W}) and a hydraulic diameter (D_h), as defined by Kays and London (1984).

$$Re_{D_h} = \frac{\rho \bar{W} D_h}{\mu} \quad (5.27)$$

The hydraulic diameter and the average velocity in this equation are defined as follows:

$$D_h = \frac{4A_{c-s-min}}{A_{wetted}} \Lambda \quad (5.28)$$

$$\bar{W} = \frac{\dot{m}}{\rho A_{c-s-min}} \quad (5.29)$$

Here, the spatial period Λ is equal to the addition of the plate length (L) and plate spacing (s) with respect to the notation of figure 1.3. The minimum cross-section area and wetted area are given by the following equations, respectively:

$$A_{c-s-min} = 2b(H - t) \quad (5.30)$$

$$A_{wetted} = 2 \left[(2L + s)b + 2 \{ L(H - t) + Hs \} + 2bt \right] \quad (5.31)$$

This definition of Reynolds number was also used by McBrien and Baliga (1988). It was employed in the experimental part of this thesis.

The geometric dimensionless parameters are listed below. The duct height ($2H$) is used as the reference length.

$$\lambda = b/2H ; L^* = L/(2H) ; s^* = s/(2H) ; t^* = 2t/(2H) = t/H \quad (5.32)$$

2.4.2 DIMENSIONLESS PARAMETERS PERTAINING TO NUMERICAL INVESTIGATIONS OF INTERRUPTED-SURFACE PASSAGES

The dimensionless parameters used in the numerical part of this work are presented in this section.

2.4.2.1 PARAMETERS RELEVANT TO SIMULATIONS OF FLOWS IN RECTANGULAR INTERRUPTED-PLATE DUCTS

The dimensionless parameters used in the numerical investigation of unsteady laminar flows in the rectangular interrupted-plate ducts of interest (see figure 1.3 for a schematic representation and the associated nomenclature) were defined in accordance with the work of Sebben (1996), mainly in order to facilitate comparisons of the results. Again, for a given geometry, the governing parameter is the Reynolds number, now defined as:

$$Re = \frac{\rho \bar{U} (2H)}{\mu} \quad (5.33)$$

In equation 2.33, \bar{U} denotes the time-mean average velocity based on the nominal cross-sectional flow area of the duct ($2H$). It is given by the following equation:

$$\bar{U} = \frac{\dot{m}}{2H\rho} \quad (5.34)$$

Once the flows were computed, the time-mean modular pressure gradient was used to calculate the corresponding friction factor, defined as follows in this problem:

$$ff = \frac{(2H)\langle\beta\rangle_{module}}{\frac{1}{2}\rho\bar{U}^2} \quad (5.35)$$

Additionally, vortex shedding frequencies were reduced to dimensionless form as follows:

$$St = \frac{f_v(2t)}{\bar{U}} \quad (5.36)$$

2.4.2.2 PARAMETERS RELEVANT TO SIMULATIONS OF FLOWS AND HEAT TRANSFER IN STAGGERED PLATE ARRAYS

In these numerical investigations, for a given geometry, the governing parameters are the Reynolds number and Prandtl number. In keeping with commonly used terminology in the practice of heat exchanger design, the Reynolds number definition is taken from Kays and London (1984):

$$Re = \frac{\rho\bar{U}_{c-smin}D_h}{\mu} \quad (5.37)$$

In this equation, \bar{U}_{c-smin} is the time-mean average velocity at the minimum cross-sectional flow area and D_h is the hydraulic diameter, given by the following equations, respectively:

$$\bar{U}_{c-smin} = \frac{\dot{m}}{(2H - 4t)\rho} \quad (5.38)$$

$$D_h = \frac{4A_{c-smin}}{A_{wetted}} \Lambda = 4 \frac{(2H - 4t)}{2(4t + 2L)} (2L) \quad (5.39)$$

In equation (2.39), Λ represents the module length, which is equal to twice the plate length (L) in this case. The Prandtl number is given by:

$$Pr = \frac{\mu c_p}{k_{fluid}} = 0.7 \text{ (for air)} \quad (5.40)$$

For this particular problem, the results included time-mean modular pressure gradients, time-mean modular average heat transfer coefficients, and vortex shedding frequencies. They were calculated and then expressed as the modular friction factor, the Colburn j factor, and the Strouhal number, defined as follows, respectively:

$$ff = \frac{D_h \langle \beta \rangle_{module}}{\frac{1}{2} \rho \bar{U}_{c-smin}^2} \quad (5.41)$$

$$j = \frac{\langle \bar{h} \rangle_{module}}{\rho c_p \bar{U}_{c-smin}} Pr^{2/3} \quad (5.42)$$

$$St = \frac{f_v(2t)}{\bar{U}_{c-smin}} \quad (5.43)$$

The time-mean module pressure gradient, $\langle \beta \rangle_{module}$, is calculated by first averaging the pressure drops across a module in time and then dividing the result by the module length

(2L). The value of $\langle \bar{h} \rangle_{module}$ is obtained by dividing the time-mean modular heat flux by a log-mean temperature difference across the module as follows:

$$\langle \bar{h} \rangle_{module} = \frac{\langle Q_{module} \rangle}{A_{H.T.} LMTD} \quad (5.44)$$

In this equation,

$$\langle Q_{module} \rangle = \dot{m} c_p (\langle T_{Bout} \rangle - \langle T_{Bin} \rangle) \quad (5.45)$$

$$LMTD = \frac{(T_w - \langle T_{Bin} \rangle) - (T_w - \langle T_{Bout} \rangle)}{\ln \left(\frac{(T_w - \langle T_{Bin} \rangle)}{(T_w - \langle T_{Bout} \rangle)} \right)} \quad (5.46)$$

$$A_{H.T.} = 2(4t + 2L) \quad (5.47)$$

It should be noted here that in the problems of interest, the temperature of the plates, T_w , was a specified constant.

The heat transfer area is twice the total plate surface area, since each module is composed of two plates. The bulk temperatures are computed at the entry and the exit planes of each module, at each instant in time, and later time-averaged. The bulk temperature definition used in this work is the following (note that the thermophysical properties of the fluid are assumed constant):

$$T_B = \frac{\int_{cs} \rho c_p u T dy}{\int_{cs} \rho c_p u dy} = \frac{\int_{cs} u T dy}{\int_{cs} u dy} \quad (5.48)$$

Again, the values of the bulk temperature are calculated and stored at each time step for each module and later are time-averaged.

CHAPTER 3 – EXPERIMENTAL APPARATUS AND TECHNIQUES

The experimental apparatus and test methodology are described in this chapter. The apparatus was originally built by McBrien (1989) and later improved by Candanedo (2003). Only an overview of this apparatus is presented here: for a full description, see Candanedo (2003). McBrien (1989) designed the first version of the apparatus which he used to obtain precise local time-mean wall static pressure distributions. Candanedo (2003) improved the test section by redesigning the duct test section and by adding a flow visualization section. This flow visualization section was modified in this work to allow insertion of a single hot-wire probe at multiple spatial positions.

3.1 OVERVIEW OF THE EXPERIMENTAL APPARATUS

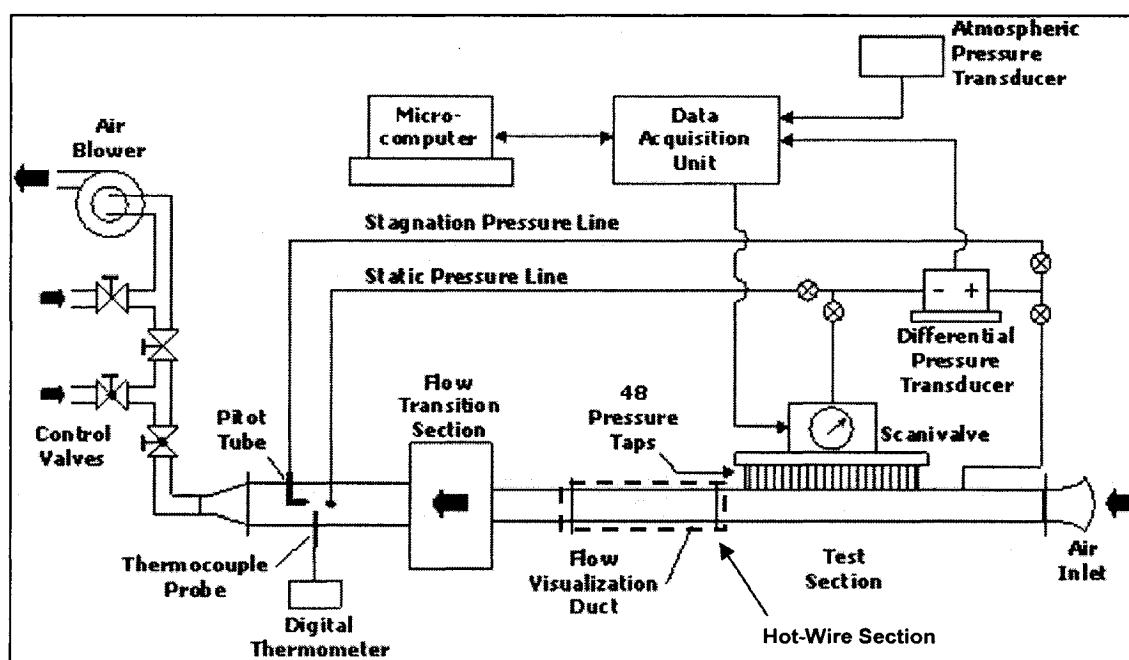


Figure 3.1 Schematic of the experimental apparatus.

A schematic representation of the experimental apparatus is given in figure 3.1. It is composed of these main elements: (i) a test section in which the wall static pressure distributions can be measured; (ii) a flow visualization section where the hot-wire

measurements were made; (iii) a flow transition section; (iv) a flow metering section; (v) a flow control, generation, and exhaust section; and (vi) a data acquisition and processing system. A brief description of each component is presented in this section. The hot-wire measurement section will be presented in full detail in section 3.2.

The test section is a straight rectangular duct that can be outfitted with plate inserts with sharp edges to form the interrupted-plate duct geometry shown in figure 1.3. Pressure taps were drilled along the axial central line of the top wall. The duct walls were machined out of aluminum, and the plate inserts were made of precision-ground steel. The new design can be easily modified to allow the testing of multiple geometrical configurations. Candanedo et al. (2003) tested nine different configurations, and also a plain duct with no plate inserts. The hot-wire measurements were performed on a single geometry, with dimensionless parameters representative of those found in actual compact heat exchanger cores (see table 3.1; dimensional uncertainties are less than ± 0.03 mm).

Table 3.1 Geometric parameters of the test and visualization sections.

Dimensional parameters (mm)						Dimensionless parameters			
2H	b	2t	L	s	D_h	λ	t^*	L^*	s^*
25.18	152.67	6.36	25.21	25.59	21.32	6.063	0.2526	1.001	1.016

The dimensionless plate thickness (t^*) is roughly twice those commonly found in actual cores (Kays & London 1984). This relatively thicker plate configuration was chosen to accentuate the vortex shedding phenomenon.

The total length of the test section is 1524 mm and it contains 30 geometric modules of periodic length $\Lambda = L + s$. The flow visualization, 609.6 mm long, is composed of another 12 modules. As demonstrated by the works of Sparrow et. al. (1977), Cur and Sparrow (1979) and Candanedo et al. (2003), the spatially periodic fully-developed regime normally prevails after 12 modules. Therefore, it is assumed that flows in the last 30 modules of the duct are characterized by this regime.

The duct walls were held together with stainless steel bolts and sealed with rubber gaskets as well as standard black electrical insulation tape. The walls were polished to obtain a very smooth finish. Although the surface roughness was not quantitatively measured, the walls provided excellent specular reflection thus indicating it is well below $0.4\ \mu\text{m}$, the lower wavelength limit of visible light.

A flow transition section separates the flow visualization and test sections from the metering section. This component is composed of two parts: a flow redevelopment section and a diffuser box. The redevelopment section is a straight rectangular duct with no plate inserts. Its dimensions are identical to those of the flow visualization section. This duct segment reduces any possible end effects that could influence flow in the visualization section. The diffuser box decelerates the flow and uniformizes it for the metering section.

The flow measurement section is a straight acrylic pipe of circular cross-section (63.22 mm internal diameter and 1320.8 mm long). Flow exiting the diffuser box enters this tube and the mass flow rate of air is measured with a traversing Pitot tube and two static pressure ports. The mass flow rate was initially calculated by measuring dynamic pressure according to the ten-point log-linear method of Winternitz and Fischl (1957). This method was simplified by calibrating it with respect to measurements at a single point, by Lorena Camargo, a graduate student at McGill University. This new method was validated and proven to be highly accurate while considerably reducing the required time for mass flow measurements.

The flow generation and control section is composed of a pipe and valve circuit linking the flow measurement section to an air blower. This centrifugal air blower (Regenair R7100A) is driven by a 10 horsepower AC motor rotating at 3450 RPM. Air is drawn through the flow metering section and the duct, and then vented to the exterior. The mass flow rate is controlled with two valves: a gate valve restricting flow and a ball valve operating the air bypass (used to prevent blower starvation). An additional bypass circuit was added by Candanedo (2003) to allow a temporary airflow shut off in the duct. Thus,

it is possible to shut the airflow in the duct without starving the blower or affecting the mass flow rate settings. This flow-circuit arrangement allowed the manipulation of the hot-wire probe during test runs without restarting the flow measurement procedure.

The apparatus is equipped with pressure-sensing instrumentation and a data acquisition system. Initially conceived by McBrien (1989) and later redesigned by Candanedo (2003), this measuring equipment was used to obtain precise intramodular time-mean static pressure distributions. Although not utilized in this thesis work, a brief description of the instrumentation and acquisition systems used by Candanedo (2003) is provided. The distributions were obtained by measuring the differential between the wall static pressure at a given tap and a reference atmospheric pressure. These measurements were performed with a differential Barocel pressure transducer, accurate to ± 0.3 Pa (Datametries, Model 590-D-1kPa-2Q8-V1X-4D, capacitance type). An electronic barometer (Vaisale PTA 427) with $\pm 0.1\%$ accuracy was used to measure atmospheric pressure. Pressure differentials above 1 kPa could not be accurately measured by the Barocel transducer. Therefore, an inclinable reservoir-type manometer (Airflow Developments, Type 5) was used for such measurements.

Pressure taps were sequentially connected to the Barocel transducer by a mechanical multiplexor (Scanivalve model 48D9). For each individual tap, 60 discrete pressure readings were taken over 15 seconds. These values were then arithmetically averaged and recorded. This procedure averaged out the inherent instantaneous static pressure fluctuations in the turbulent flow and provided adequate time-averaged pressure values [Candanedo (2003)]. A microprocessor-based data acquisition unit (Hewlett-Packard, Model 3497A) was used to record the measured pressure values. These values were then sent to a personal computer and processed with an acquisition program.

3.2 HOT-WIRE TEST SECTION AND INSTRUMENTATION

The visualization section was redesigned in this work to accommodate a hot-wire probe holder. The new top plate has nine holes through which the probe holder can be inserted.

These holes are shown in figure 3.2 in which the shaded areas represent the plate inserts. Three of these holes (H2, H5 and H8) are aligned with the duct longitudinal centerline. The other six (H3, H6 and H9; H1, H4 and H7) are offsets shifted laterally from the centerline by 38.1 mm ($b/4$). Once inserted, the probe holder's bottom surface is flush with the top wall of the duct, thus the wetted surface is still continuous. Holes that do not contain the probe holder are simply filled with plugs. Since the pressure inside the duct is lower than atmospheric, the plugs and holder are held in place due to suction and are additionally secured by a close fit with the plate bores. O-rings were incorporated in the plugs and holder diameters to seal the holes and prevent leakage into the duct. Sealing grease was also applied to offer further sealing. Two of the plugs incorporated pressure taps which were used to measure the wall static pressure near the hot-wire position. They were positioned at the same streamwise location as that of the probe holder.

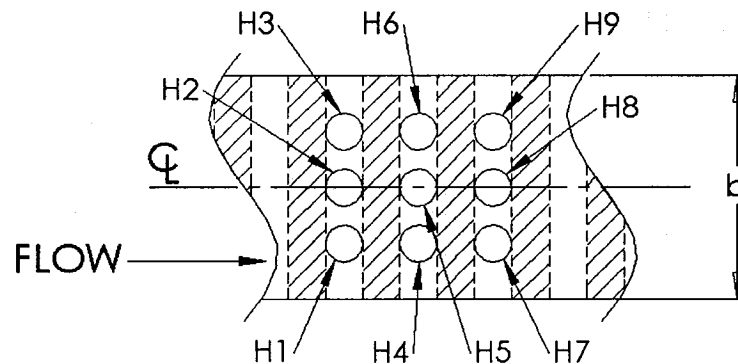


Figure 3.2 Top view of the visualization section and wire holder insertion holes.

Three different probe holders were designed to offer additional measuring positions in the streamwise direction (z). The vertical position (x) of the single hot wire was also adjustable. In total, up to 12 different positions in the x - z plane were investigated for each hole. The coordinates of these positions, with respect to the local x - z axes shown in figure 3.3, are listed in table 3.2. The uncertainties in the measured positions are lower than ± 0.10 mm.

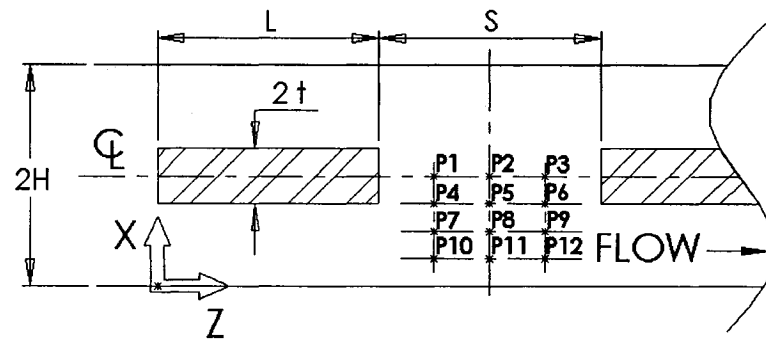


Figure 3.3 Positions of the single hot-wire probe in the longitudinal cross-section of the duct.

Table 3.2 Coordinates of the hot-wire positions with reference to the local x-z axis (figure 3.3) (in mm).

	P1	P2	P3	P4	P5	P6
x	12.5	12.5	12.5	9.3	9.3	9.3
z	32.4	39.2	46.1	32.4	39.2	46.1

	P7	P8	P9	P10	P11	P12
x	6.1	6.1	6.1	3.0	3.0	3.0
z	32.4	39.2	46.1	32.4	39.2	46.1

The hot wire was oriented normal to the main flow direction (z) and parallel to the y direction at all times, thus measuring the magnitude of the cross flow in the x - z plane. The single hot-wire probe used was a TSI 1210 – T1.5. The wire is made of platinum coated tungsten and has a diameter of 3.81×10^{-3} mm. The sensing region is a small portion of the wire (1.27 mm) where the platinum is etched out. The hot wire was operated at a constant temperature of 250 °C. It was calibrated once a week with a calibration facility kindly supplied by Professor Laurent Mydlarski and Mr. Étienne Costa-Patry at McGill University. The probe was calibrated for velocities ranging from 2 m/s to 20 m/s at room temperatures of $23.3 \text{ °C} \pm 0.5 \text{ °C}$. Since hot-wire measurements can be influenced by ambient fluid temperature variations, the laboratory room temperature was strictly maintained in the aforementioned calibration range. After a week

of experiments, the first test runs made with a freshly calibrated probe were repeated, to check if that the hot-wire measurements had not drifted in time.

The hot-wire anemometer used was a DISA CTA Bridge 56C16 operated at an overheat ratio of 1.825. This anemometer maintained the wire temperature at a constant value by supplying the required power to compensate the convective heat transfer losses to the flow. The instantaneous cross flow velocity magnitude is thus converted into a voltage signal by the anemometer. This signal is then measured with a data acquisition system.

The voltage signal was acquired with a personal computer equipped with a data acquisition card (National Instruments PCI-6036E A/D) and a BNC-2110 board. Discrete samples of the anemometer signal were obtained at a frequency of 10 000 Hz. Low pass filtering was set at 10 000 Hz to filter out high frequency noise. The periodic flow phenomena of interest were always below 1000 Hz: thus, the aforementioned filtering and sampling rate were more than adequate for obtaining accurate hot-wire measurements. A LabView program, generously supplied by Professor Laurent Mydlarski, was used to acquire and store the discrete signal values. As was mentioned in chapter 2, a hundred blocks of data, each composed of 8192 discrete samples, were gathered to produce a single power spectrum at a given duct Reynolds number and wire position. This combination of block number and block sample size was shown to provide smooth spectrums while requiring a reasonable sampling time of 82 seconds per spectrum. A FORTRAN code was then used to compute the power spectrums and a Matlab program analyzed the spectrums to obtain the main vortex shedding frequencies.

3.3 SUMMARY OF THE EXPERIMENTAL PROCEDURE

The test procedure followed to obtain a single power spectrum is presented below.

1. The air blower and instrumentation were turned on at least an hour before a test run, to warm-up and stabilize then. The anemometer was turned on but the hot-wire probe was kept “cold” except during sampling to prevent unnecessary oxidation of the sensing area.

2. The Barocel pressure transducer was zeroed as much as possible just before starting a test run. A mass flow rate measuring code was launched and a tentative Reynolds number was given. The static and stagnation pressures of the Pitot tube were fed to the Barocel transducer and the pressure differential was displayed on the data acquisition screen. The program indicated the dynamic pressure required to attain the desired mass flow rate. The flow control valves were then adjusted until the indicated dynamic pressure matched the prescribed value.

3. The atmospheric pressure and flow temperature were measured and recorded. The two Barocel measuring ports were then linked together to measure the “zero pressure”. Even if no pressure differential was present, the measured value was generally slightly offset from zero. This offset value was measured 30 times, averaged, stored and was later used to correct future Barocel pressure difference readings.

4. The difference between atmospheric pressure (P_{atm}) and the wall static pressure on the hot-wire holder surface ($P_{hot\ wire}$) was measured and corrected by subtracting the “zero pressure” from the obtained value. Similarly, the pressure difference between $P_{hot\ wire}$ and the Pitot tube static taps (P_{static}) was recorded and corrected. Thus, absolute values of $P_{hot\ wire}$ and P_{static} were then computed by the mass flow program. Air density at the metering and hot-wire sections was computed using the ideal gas law. Pressure differentials above 1 kPa prompted the code to request a manual pressure measurement with the inclinable manometer.

5. The mass flow rate was computed by measuring the Pitot tube dynamic pressure ($P_{stag} - P_{static}$) at a single point in the metering section tube. The average velocity in the tube was then calculated using a previously obtained calibration curve. With the known local air density and the area cross of section, the program computed the time-averaged mass flow rate. The mean velocity at the hot-wire section was then calculated by dividing the duct mass flow rate by the local air density (obtained in step 4) and the corresponding cross-sectional area. The Reynolds number at the hot-wire position was finally computed with

the definition given by Kays and London (1984). These mass flow rate measurements were conducted simultaneously with the hot-wire sampling described in step 6.

6. The hot-wire data acquisition program was launched and the sampling parameters were prescribed. The probe was activated and the data sampling was started at the same time as the mass flow measurements. Once a hundred blocks of 8192 samples were acquired, the power to the hot wire was shut off.

7. The anemometer voltage samples were converted into velocity with a FORTRAN program that uses a relation established during the probe calibration. Another FORTRAN code processed the velocity samples and computed the power spectrums. Finally, a Matlab program was used to calculate the main vortex shedding frequency (and Strouhal number), if one was observable. The results were stored in an individual Excel spreadsheet that generated a plot of the power spectrum.

These steps were repeated for each hot-wire position and mass flow rate combination. The wire was calibrated at the beginning of each week. At the end of this period, the first test runs of the week, made with a freshly calibrated probe, were repeated to check if the hot-wire measurements had not drifted significantly with time. The experimental results are presented in chapter 5 along with the results of the numerical investigation.

CHAPTER 4

NUMERICAL METHOD

A finite volume method (FVM) that was developed, tested, and used to investigate the two-dimensional flows of interest in this work is presented in this chapter. This FVM is inspired by and borrows heavily from the works of Patankar (1980), Leonard (1979), Van Doormal and Raithby (1984), and Settari and Aziz (1973). This chapter presents an overview of this FVM in a complete yet concise manner.

4.1 GOVERNING EQUATIONS

The governing equations for the laminar, two-dimensional, unsteady flows of interest were presented earlier in chapter 2. Here, the appropriate continuity, x -momentum, y -momentum, and energy equations are recast in the following forms, which are amenable to discretization by the proposed FVM:

$$\frac{\partial \rho}{\partial t} + \frac{\partial(\rho u)}{\partial x} + \frac{\partial(\rho v)}{\partial y} = 0 \quad (4.1)$$

$$\frac{\partial(\rho u)}{\partial t} + \frac{\partial(\rho uu)}{\partial x} + \frac{\partial(\rho vu)}{\partial y} = -\frac{\partial p}{\partial x} + \frac{\partial}{\partial x} \left(\mu \frac{\partial u}{\partial x} \right) + \frac{\partial}{\partial y} \left(\mu \frac{\partial u}{\partial y} \right) + S_u \quad (4.2)$$

$$\frac{\partial(\rho v)}{\partial t} + \frac{\partial(\rho uv)}{\partial x} + \frac{\partial(\rho vv)}{\partial y} = -\frac{\partial p}{\partial y} + \frac{\partial}{\partial x} \left(\mu \frac{\partial v}{\partial x} \right) + \frac{\partial}{\partial y} \left(\mu \frac{\partial v}{\partial y} \right) + S_v \quad (4.3)$$

$$\frac{\partial(\rho T)}{\partial t} + \frac{\partial(\rho u T)}{\partial x} + \frac{\partial(\rho v T)}{\partial y} = \frac{\partial}{\partial x} \left(\frac{k}{c_p} \frac{\partial T}{\partial x} \right) + \frac{\partial}{\partial y} \left(\frac{k}{c_p} \frac{\partial T}{\partial y} \right) + S_T \quad (4.4)$$

The S_u and S_v terms represent volumetric forces that may affect the flow, and are retained here for the sake of generality of the proposed FVM. However, they are equal to zero in the simulations undertaken in this work because no such sources are present in the problems investigated here (gravitational effects are absorbed in the reduced pressure, p).

The above-mentioned forms of the governing equations can all be recovered from a single general advection-diffusion equation, as pointed out by Patankar (1980). This general equation is the following:

$$\frac{\partial(\rho\phi)}{\partial t} + \frac{\partial(\rho u\phi)}{\partial x} + \frac{\partial(\rho v\phi)}{\partial y} = \frac{\partial}{\partial x} \left(\Gamma_{\phi} \frac{\partial\phi}{\partial x} \right) + \frac{\partial}{\partial y} \left(\Gamma_{\phi} \frac{\partial\phi}{\partial y} \right) + S_{\phi} \quad (4.5)$$

In this equation, ϕ is a general specific (per unit mass) dependent variable; Γ_{ϕ} is the corresponding diffusion coefficient; and S_{ϕ} is the corresponding volumetric source term. The use of this general form of the governing equations facilitates the formulation of general FVMs [Patankar (1980)].

4.2 DOMAIN DISCRETIZATION

4.2.1 TYPES OF DOMAIN

Two types of calculation domains were considered in this work. To study developing laminar unsteady flows in rectangular interrupted-surface ducts, a regular, non-periodic, grid was used. For developing laminar unsteady flows in staggered plate arrays, a cyclic domain, formed by multiple rows of plates, was chosen to model the spatial periodicity of the geometry and the flows. Both these types of domain are planar, two-dimensional, and rectangular in shape.

The cyclic domain is shown in figure 4.1. It is divided into two sections: a series of plate modules and a flow exit zone. The boundaries parallel to the main flow direction are cyclic. An integer numbers of geometrically similar modules, each composed of two staggered plates, can be combined in both the x and y directions to obtain the desired configurations of the calculation domains.

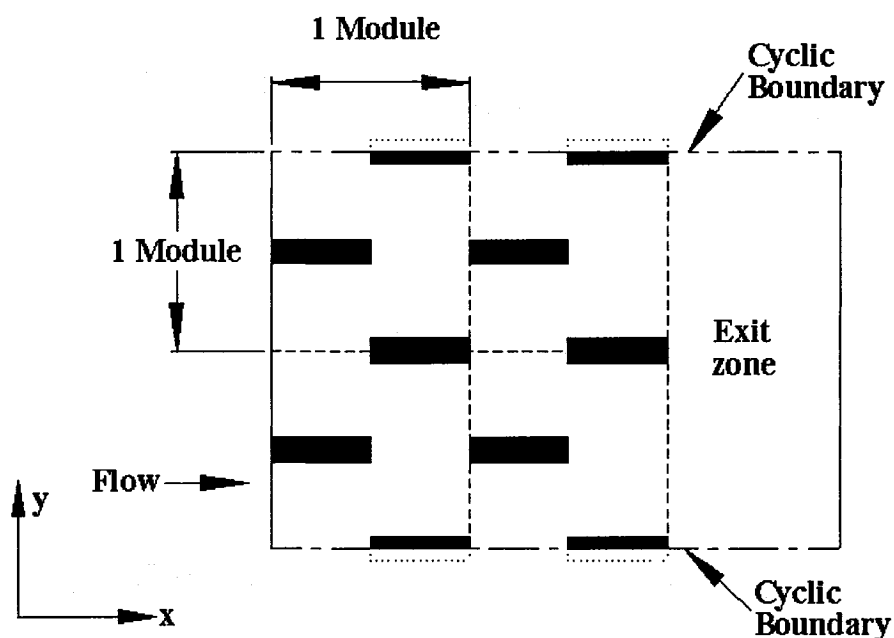


Figure 4.1 Example of a cyclic computation domain.

The regular domain used for the computation of developing laminar unsteady flows in rectangular interrupted-surface ducts is illustrated in figure 4.2. Each module includes a single plate and a gap. Again, an integer number of such modules can be combined in the x direction to obtain the desired configurations of the calculation domain.

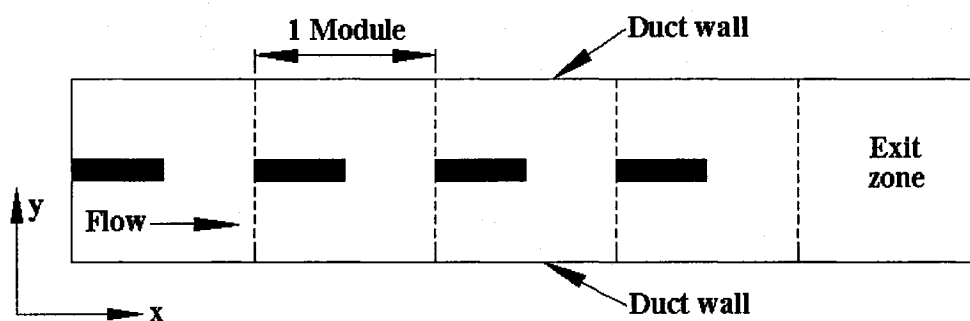


Figure 4.2 Representation of a regular computation domain.

Both of the aforementioned types of calculation domain are first divided into non-overlapping and contiguous control volumes (CVs), forming a Cartesian grid of such CVs. A node or grid point is then located at the center of each such CV. The nodes are then joined by lines in the x and y directions (grid lines) and nodes are also located at

points where these lines intersect the domain boundaries. The nodes or grid points are locations where every dependent variable is stored and computed. Thus, this FVM is a so-called co-located method. It is also an equal-order control-volume-based finite-difference method [Baliga and Atabaki (2006)], as will become clear in later sections of this chapters. The resulting computational grid, for a simple cyclic domain, is shown in figure 4.3: the CV faces are represented by the dashed lines; the nodes are portrayed as black dots; and the continuous lines are the grid lines. A set of additional nodes are placed where the grid intersects the domain at the non-cyclic boundaries: the nodes located on non-cyclic boundaries do not have a control volume associated with them. At the cyclic boundaries, the last row of nodes is a duplication of the first one, therefore the dependent variables they store are respectively equal.

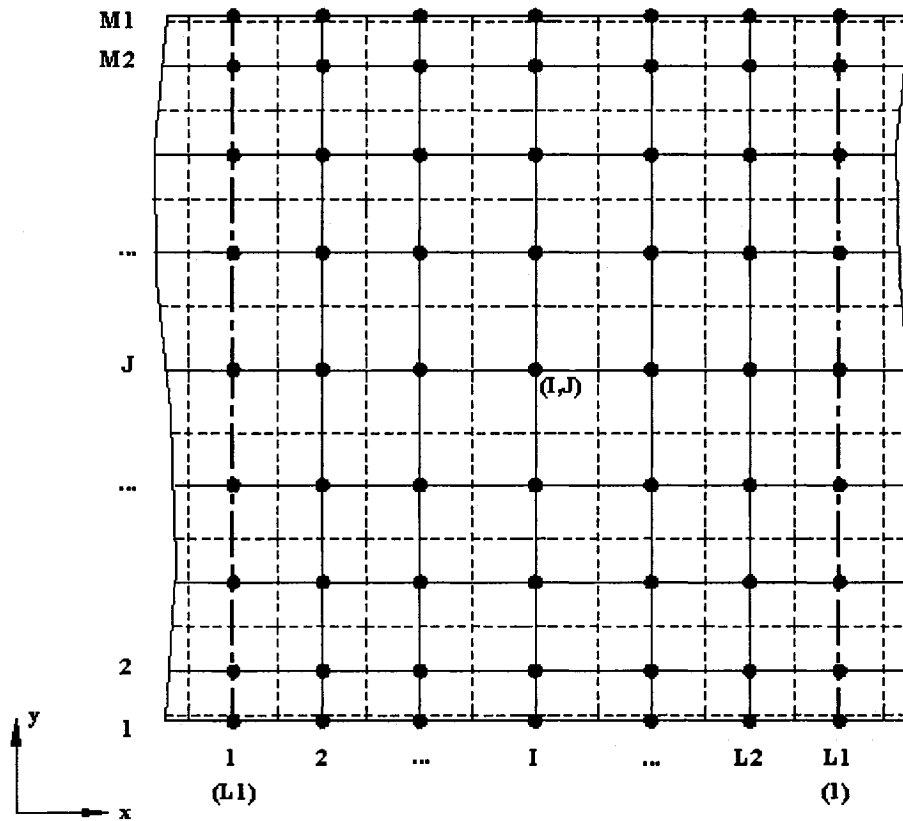


Figure 4.3 Sample grid and node notation indexes for a cyclic grid.

4.2.2 NODE NOMENCLATURE

Again, all the dependent variables and fluid properties are calculated and stored at each node. Once the domain is discretized, every node relates with its neighbors according to the nomenclature shown in figure 4.4. The node of interest, here named "P", is related to its 8 neighbors (E, EE, W, WW, N, NN, S, SS) by x and y direction grid lines. The points where the gridlines intersect the CV faces, and where fluid properties and some variables are interpolated, are denoted with lower case letters. The notation for inter-nodal distances and also the x and y extents of the CV are also shown in figure 4.4.

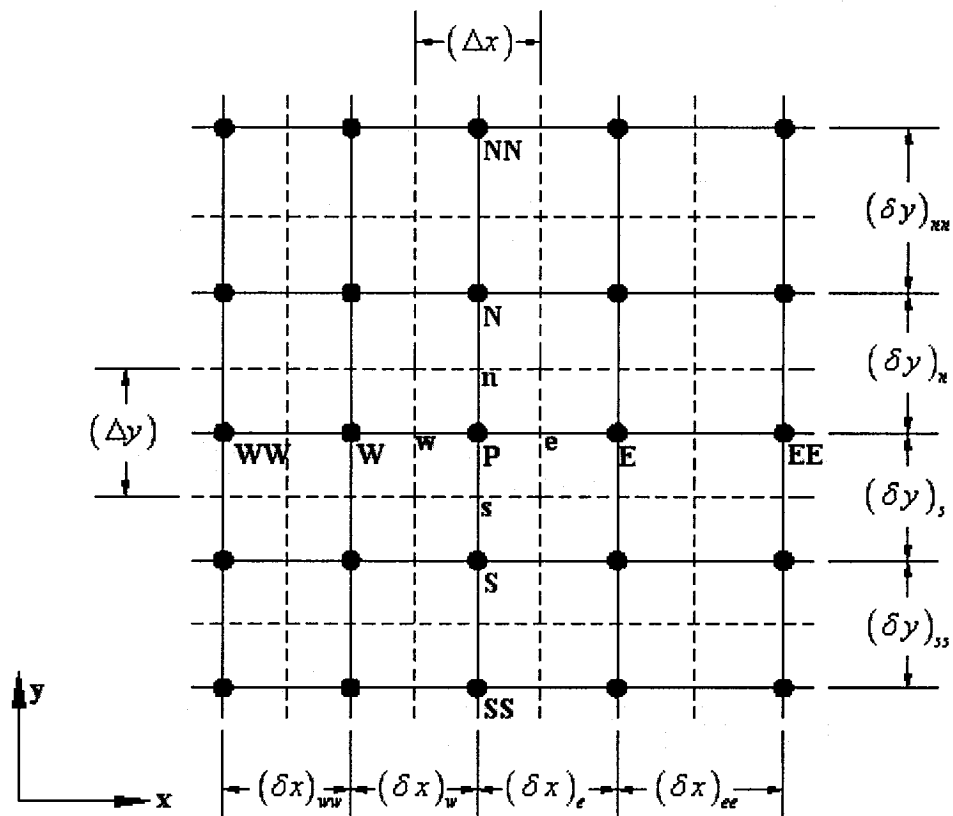


Figure 4.4 CVFDM grid and nomenclature for a node and its related neighbors.

4.3 DISCRETIZED CONSERVATION EQUATIONS

4.3.1 TIME AND SPACE INTEGRATION OF EQUATIONS

The general advection-diffusion equation (4.5) is integrated over a control volume for point P (see figure 4.4) and over a time step, Δt ; then algebraic approximation are derived for this integral equation to obtain the discretized equations in the FVM. This integral is first approximated as follows:

$$\begin{aligned} & (\rho\phi_P - \rho\phi_P^0) \frac{\Delta x \Delta y}{\Delta t} + f(J_e - J_w + J_n - J_s) + \\ & (1-f)(J_e - J_w + J_n - J_s)^0 = fS_\phi \Delta x \Delta y + (1-f)S_\phi^0 \Delta x \Delta y \end{aligned} \quad (4.6)$$

In this equation, J_e , J_w , J_n , and J_s represent rates of advection-diffusion transport across the east, west, north, and south faces of the CV surrounding node P (see figure 4.4). They are approximated by the following equations:

$$\begin{aligned} J_e &= (\rho u \phi - \Gamma_\phi \frac{\partial \phi}{\partial x})|_e \Delta y \\ J_w &= (\rho u \phi - \Gamma_\phi \frac{\partial \phi}{\partial x})|_w \Delta y \\ J_n &= (\rho v \phi - \Gamma_\phi \frac{\partial \phi}{\partial y})|_n \Delta x \\ J_s &= (\rho v \phi - \Gamma_\phi \frac{\partial \phi}{\partial y})|_s \Delta x \end{aligned} \quad (4.7)$$

The integration in time of the advection and diffusion terms is performed with a weighting function "f" that characterizes the evolution of the dependent variable in time. The chosen value of "f", which may vary between 0 and 1, defines the type of time integration scheme used. In the present work, this value is generally set to 0.5 (Crank-Nicolson scheme): this is equivalent to prescribing a linear variation of ϕ over the time

step [Patankar (1980)]. The superscript “^o” denotes the values at current time, t , and terms without this superscript represent values at time $t + \Delta t$.

Equation (4.6) is now recast into a more convenient form for further discretization:

$$\begin{aligned} & (\rho\phi_p - \rho\phi_p^o) \frac{\Delta x \Delta y}{f \Delta t} + (J_e - J_w + J_n - J_s) + \\ & \frac{(1-f)}{f} (J_e - J_w + J_n - J_s)^o = S_\phi \Delta x \Delta y + \frac{(1-f)}{f} S_\phi^o \Delta x \Delta y \end{aligned} \quad (4.8)$$

With this formulation, multiple time schemes can be invoked, each having their advantages and drawbacks. The simplest one is the explicit scheme ($f = 0$), and it is the easiest to implement: since the old value of ϕ is assumed to prevail over the whole time step, the new value may be computed explicitly, without any reference to its neighbors at the new time level. Although simple, this scheme suffers from multiple weaknesses. First, the size of the time step is limited by the Courant-Friedrich-Levy (CFL) criterion [Roache (1976); Patankar (1980); Ferziger and Peric (1996)] to ensure stability and physically realistic results. To satisfy this criterion, every refinement of the spatial grid for precision purposes requires an even smaller time step (which, in the two-dimensional problems of interest, diminishes as the square of the control volume size). Finally, this scheme is only first-order accurate in time [Patankar (1980)].

In the fully-implicit scheme ($f = 1$), ϕ is assumed to be equal to the newly calculated value over the whole time step. This scheme offers unconditional stability, meaning that there is no stability criterion limiting the size of the time step. However, it is also first-order accurate in time: thus, it was dismissed, in favor of the more accurate semi-implicit Crank-Nicolson scheme ($f = 0.5$).

The Crank-Nicolson scheme is implemented by setting the value of f to 0.5. It is equivalent to assuming a linear variation of the value of ϕ over the time step, as shown in figure 4.5. This scheme is shown to be unconditionally stable in classical numerical

analysis books. However, in order to avoid spurious (numerical) oscillations of the computed dependent variables in time, the time step in this scheme must satisfy a criterion analogous to the CFL criterion [Patankar (1980)]. Nevertheless, this scheme is second-order accurate in time and also relatively easy to implement. Furthermore, the fluid flow problems of interest are unsteady and nonlinear, thus a small time step has the advantage of providing quick convergence of iterative solution procedures (needed to tackle the nonlinearity) at each time step. Keeping these features in mind, the Crank-Nicolson scheme was chosen for use in this work.

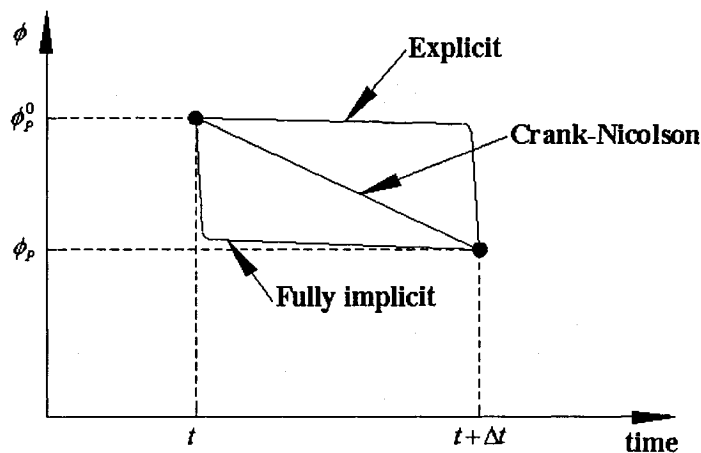


Figure 4.5 Evolution of the dependent variable in time.

4.3.2 APPROXIMATION OF DIFFUSION TRANSPORT TERMS

Piecewise-linear interpolation of the dependent variables along grid lines between adjacent nodes is used to derive algebraic approximations to the derivatives in the diffusion transport terms in equations (4.6) and (4.7). Thus, the diffusion transport rates at the east and west boundaries of the CV associated with node P in figure 4.4 are approximated as follows:

$$\begin{aligned}
J_{Diff\ e} &= -\Gamma_{\phi_e} \Delta y \frac{(\phi_E - \phi_P)}{(\delta x)_e} \\
J_{Diff\ w} &= -\Gamma_{\phi_w} \Delta y \frac{(\phi_P - \phi_W)}{(\delta x)_w}
\end{aligned}
\tag{4.9}$$

The diffusion coefficient Γ_ϕ is interpolated at each volume faces with a conductance analogy, as proposed by Patankar (1980). This interpolation procedure is more accurate and becomes especially useful in the incorporation of solid regions in the computational domain, as explained in further detail in section 4.3.6. Thus, for example, the diffusion coefficient at the east face of the CV surrounding node P in figure 4.4 is obtained as follows [Patankar (1980)]:

$$\Gamma_{\phi_e} = \frac{(\delta x)_e \Gamma_{\phi_P} \Gamma_{\phi_E}}{(\delta x)_{e-} \Gamma_{\phi_E} + (\delta x)_{e+} \Gamma_{\phi_P}}
\tag{4.10}$$

The expressions for $J_{Diff\ w}$, $J_{Diff\ s}$, and $J_{Diff\ n}$ can be obtained in an analogous manner.

4.3.3 APPROXIMATION OF ADVECTION TRANSPORT TERMS

The advection terms in equations 4.6 and 4.7 at the east and west faces of the CV surrounding node P in figure 4.4 are first written as follows:

$$\begin{aligned}
J_{Adv\ e} &= (\rho u_m \Delta y) \Big|_e \phi_e \\
J_{Adv\ w} &= (\rho u_m \Delta y) \Big|_w \phi_w
\end{aligned}
\tag{4.11}$$

The subscript "m" in the previous equations denotes that u_m is a "mass-conserving" velocity component. These mass flow rates are computed separately by using the so-called momentum interpolation scheme [Ferziger and Peric (1996)] and stored for later use. This procedure is described in more detail in section 4.3.7.

There are multiple schemes available in the literature to interpolate the value of ϕ at the desired control-volume face. Some popular first-order schemes, like the hybrid difference scheme of Spalding (1972) and the power-law difference scheme of Patankar (1980), were considered for this work. While relatively robust and easy to implement, these schemes are known to cause significant false diffusion when the flow is not parallel to the grid lines. Therefore, the higher-order quadratic upstream interpolation for convection kinematics (QUICK) scheme of Leonard (1979) was chosen to model the advection transport terms.

As its name suggests, the QUICK scheme performs a piecewise quadratic interpolation of ϕ between nodes along grid lines. Furthermore, it accounts for the flow direction: the nodes for the determination of the coefficients in the quadratic interpolation are chosen in accordance with the direction of flow. The interpolation uses the nearest two upstream nodes and the closest downstream node along a grid line for this interpolation. For example, with respect to the node cluster shown in figure 4.6, to obtain the value of ϕ_e , the values of ϕ_P , ϕ_E , and either ϕ_W or ϕ_{EE} , whichever lies on the upstream side of the e CV face, are interpolated using a quadratic interpolation function [Leonard (1979)].

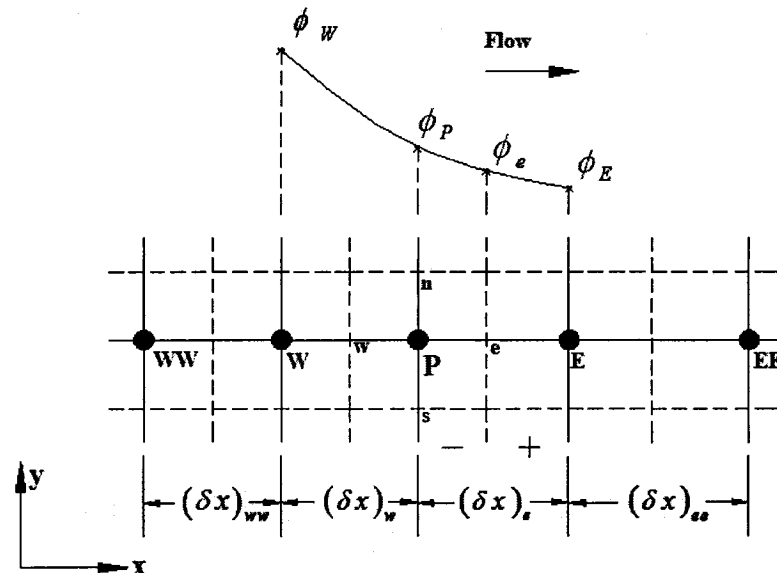


Figure 4.6 QUICK interpolation scheme of a dependent variable ϕ .

If the mass-conserving velocity component in the x direction at e , $(u_m)_e$, is positive, then the interpolation for ϕ_e is given by the following equation:

$$\begin{aligned} \phi_e|_{+flow} &= \frac{\left((\delta_x)_w^2 + (\delta_x)_w (\delta_x)_{e-}\right) \frac{(\delta_x)_{e-}}{(\delta_x)_e}}{(\delta_x)_w^2 + (\delta_x)_w (\delta_x)_e} \phi_E - \frac{(\delta_x)_{e+} (\delta_x)_{e-}}{(\delta_x)_w^2 + (\delta_x)_w (\delta_x)_e} \phi_W + \\ &\frac{\left((\delta_x)_w^2 + (\delta_x)_w (\delta_x)_{e-}\right) \frac{(\delta_x)_{e+}}{(\delta_x)_e} + (\delta_x)_{e+} (\delta_x)_{e-} + (\delta_x)_{e+} (\delta_x)_W}{(\delta_x)_w^2 + (\delta_x)_w (\delta_x)_e} \phi_P \end{aligned} \quad (4.12)$$

This expression can be compactly written as follows:

$$\phi_e|_{+flow} = C1_{e+} \phi_E + C2_{e+} \phi_W + C3_{e+} \phi_P \quad (4.13)$$

If $(u_m)_e$, is negative, then the interpolation for ϕ_e is given by the following equation:

$$\begin{aligned} \phi_e|_{-flow} &= \frac{\left((\delta_x)_{ee}^2 + (\delta_x)_{ee} (\delta_x)_{e+}\right) \frac{(\delta_x)_{e-}}{(\delta_x)_e} + (\delta_x)_{e+} (\delta_x)_{e-} + (\delta_x)_{e-} (\delta_x)_{ee}}{(\delta_x)_{ee}^2 + (\delta_x)_{ee} (\delta_x)_e} \phi_E + \\ &\frac{\left((\delta_x)_{ee}^2 + (\delta_x)_{ee} (\delta_x)_{e+}\right) \frac{(\delta_x)_{e+}}{(\delta_x)_e}}{(\delta_x)_{ee}^2 + (\delta_x)_{ee} (\delta_x)_e} \phi_P - \frac{(\delta_x)_{e+} (\delta_x)_{e-}}{(\delta_x)_{ee}^2 + (\delta_x)_{ee} (\delta_x)_e} \phi_{EE} \end{aligned} \quad (4.14)$$

Again, this expression can be compactly written as follows:

$$\phi_e|_{-flow} = C1_{e-} \phi_P + C2_{e-} \phi_{EE} + C3_{e-} \phi_E \quad (4.15)$$

Thus the advection transport rate across the east face of the CV for node P in figure 4.4 is approximated as follows (the details of the mass-conserving velocity calculations will be presented in section 4.3.7):

$$J_{Adv_e} = (C1_{e+} \phi_E + C2_{e+} \phi_W + C3_{e+} \phi_P) \max \left[(\rho u_m \Delta y) \Big|_e, 0 \right] + (C1_{e-} \phi_P + C2_{e-} \phi_{EE} + C3_{e-} \phi_E) \min \left[(\rho u_m \Delta y) \Big|_e, 0 \right] \quad (4.16)$$

Likewise, for the west face, the following equation applies:

$$J_{Adv_w} = (C1_{w+} \phi_P + C2_{w+} \phi_{WW} + C3_{w+} \phi_W) \max \left[(\rho u_m \Delta y) \Big|_w, 0 \right] + (C1_{w-} \phi_W + C2_{w-} \phi_E + C3_{w-} \phi_P) \min \left[(\rho u_m \Delta y) \Big|_w, 0 \right] \quad (4.17)$$

Additionally, it can be proven that the west-face coefficients for a node I are related to the east-face ones of the previous node $(I-1)$, as shown in the following equation:

$$\begin{aligned} C1_{w+}(I, J) &= C1_{e+}(I-1, J) & C1_{w-}(I, J) &= C1_{e-}(I-1, J) \\ C2_{w+}(I, J) &= C2_{e+}(I-1, J) & C2_{w-}(I, J) &= C2_{e-}(I-1, J) \\ C3_{w+}(I, J) &= C3_{e+}(I-1, J) & C3_{w-}(I, J) &= C3_{e-}(I-1, J) \end{aligned} \quad (4.18)$$

Similar expressions can be derived for the calculation of J_{Adv_n} and J_{Adv_s} .

4.3.4 COMPLETE DISCRETIZED EQUATION

The complete discretized conservation equation for the dependent variable at node P, ϕ_P , is assembled by combining the diffusion, advection, source, and unsteady terms. This equation can be arranged in the following form:

$$a_P \phi_P = a_E \phi_E + a_W \phi_W + a_N \phi_N + a_S \phi_S + a_{EE} \phi_{EE} + a_{WW} \phi_{WW} + a_{NN} \phi_{NN} + a_{SS} \phi_{SS} + b \quad (4.19)$$

where:

$$\begin{aligned}
a_E &= \frac{\Gamma_e \Delta y}{(\delta x)_e} - C1_{e+} \max [(\rho u_m \Delta y)|_e, 0] + C2_{w-} \min [(\rho u_m \Delta y)|_w, 0] - C3_{e-} \min [(\rho u_m \Delta y)|_e, 0] \\
a_W &= \frac{\Gamma_w \Delta y}{(\delta x)_w} + C1_{w-} \min [(\rho u_m \Delta y)|_w, 0] - C2_{e+} \max [(\rho u_m \Delta y)|_e, 0] + C3_{w+} \max [(\rho u_m \Delta y)|_w, 0] \\
a_N &= \frac{\Gamma_n \Delta x}{(\delta y)_n} - C1_{n+} \max [(\rho v_m \Delta x)|_n, 0] + C2_{s-} \min [(\rho v_m \Delta x)|_s, 0] - C3_{n-} \min [(\rho v_m \Delta x)|_n, 0] \\
a_S &= \frac{\Gamma_s \Delta x}{(\delta y)_s} + C1_{s-} \min [(\rho v_m \Delta x)|_s, 0] - C2_{n+} \max [(\rho v_m \Delta x)|_n, 0] + C3_{s+} \max [(\rho v_m \Delta x)|_s, 0] \\
a_{EE} &= -C2_{e-} \min [(\rho u_m \Delta y)|_e, 0] \\
a_{WW} &= C2_{w+} \max [(\rho u_m \Delta y)|_w, 0] \\
a_{NN} &= -C2_{n-} \min [(\rho v_m \Delta x)|_n, 0] \\
a_{SS} &= C2_{s+} \max [(\rho v_m \Delta x)|_s, 0] \\
a_P &= \underbrace{\sum a_{nb} - S_P \Delta x \Delta y}_{\text{SteadyStateTerms}} + \underbrace{\frac{\rho \Delta x \Delta y}{f \Delta t}}_{\text{UnsteadyTerm}} \\
b &= \underbrace{S_C \Delta x \Delta y}_{\text{SteadyStateTerm}} + \underbrace{\frac{\rho \Delta x \Delta y}{f \Delta t} \phi_P^0 + \frac{(1-f)}{f} \left[\sum a_{nb}^0 \phi_{nb}^0 - a_{P(\text{Steady St.})}^0 \phi_P^0 + S_C^0 \Delta x \Delta y \right]}_{\text{UnsteadyTerms}}
\end{aligned}
\tag{4.20}$$

In the previous set of equations, $\sum a_{nb}$ is the summation of the neighboring coefficients needed to calculate a_P . Coefficients a_P and b are formed by adding the unsteady terms to the steady state ones. Lastly, $a_{P(\text{Steady St.})}^0 \phi_P^0$ represents $(\sum a_{nb} - S_P \Delta x \Delta y)$ from the previous time iteration.

It is also important to point out that the source term, S_ϕ , has been linearized in the following way, following the recommendations of Patankar (1980):

$$S_\phi = S_C + S_P\phi \quad (4.21)$$

As suggested by Patankar (1980), the S_P must be negative to ensure numerical stability and realistic solutions. The respective values of S_C , S_P and Γ_ϕ for each dependent variable will be discussed in the following sections. First, it is necessary to present a modified QUICK scheme required for nodes near a domain boundary with a given flux condition.

4.3.5 MODIFIED QUICK SCHEME FOR GIVEN DIFFUSION FLUX BOUNDARY CONDITION

If the boundary condition is of the given diffusion-flux type, the aforementioned derivation of the QUICK scheme is modified as discussed in this section. This modification is described here for an upper border node (at $J=M2$), with reference to the nomenclature shown in figure 4.7.

For the case shown in figure 4.7, the approximated southern advection transport rate, J_{Adv_s} , would normally involve a reference to the northern node ϕ_N if the mass flow at the south face of the CV is in the negative y direction. However, if a diffusion flux is imposed as the boundary condition at the north face, the aforementioned advection transport rate must be calculated with a modified interpolation scheme to prevent any reference to the undetermined ϕ_N . A new quadratic interpolation function is derived in which the reference to ϕ_N is replaced by accounting for the given diffusion flux.

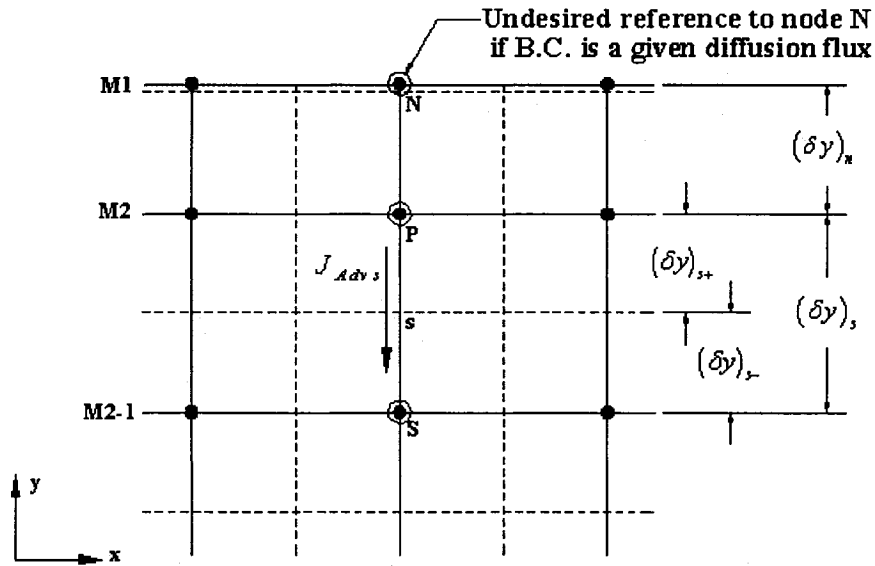


Figure 4.7 QUICK scheme referencing to undetermined north node.

This modification is only applied when the boundary condition is one of specified (given) diffusion flux and the mass flow rate at the southern face of the CV is in the negative y direction. If ϕ_s is interpolated at the lower south boundary with the modified quadratic function, the following result is obtained:

$$\phi_s = \left(\phi_s - \phi_p + \frac{Flux_{in}}{\Gamma} (\delta y)_s \right) \frac{((\delta y)_n + (\delta y)_{s+})^2 - (\delta y)_n^2}{((\delta y)_n + (\delta y)_s)^2 - (\delta y)_n^2} - \frac{Flux_{in}}{\Gamma} (\delta y)_{s+} + \phi_p \quad (4.22)$$

In this case, the south-face advection transport rate, J_{Adv_s} is given by the following equation:

$$J_{Adv_s} = (\rho v_m \Delta x) \Big|_s \phi_s \quad (4.23)$$

When the interpolated ϕ_s is substituted:

$$\begin{aligned}
J_{Adv_s} = & (\rho v_m \Delta x) \Big|_s AI \cdot \phi_s + \\
& (\rho v_m \Delta x) \Big|_s [1 - AI] \phi_p + \\
& (\rho v_m \Delta x) \Big|_s \frac{Flux_{in}}{\Gamma} [AI \cdot (\delta y)_s - (\delta y)_{s+}]
\end{aligned} \tag{4.24}$$

$$\text{where } AI = \frac{((\delta y)_n + (\delta y)_{s+})^2 - (\delta y)_n^2}{((\delta y)_n + (\delta y)_s)^2 - (\delta y)_n^2}$$

Therefore, the contributions of J_{Adv_s} to the coefficients a_s , a_p and b of the discretized equation for node $J = M2$ in this particular case are the following:

$$\begin{aligned}
a_s &= (\rho v_m \Delta x) \Big|_s AI \\
b &= (\rho v_m \Delta x) \Big|_s \frac{Flux_{in}}{\Gamma} [AI \cdot (\delta y)_s - (\delta y)_{s+}] \\
a_p &= a_s - \underbrace{(\rho v_m \Delta x) \Big|_s}_{\substack{\text{Term will cancel out} \\ \text{at convergence}}}
\end{aligned} \tag{4.25}$$

The south CV face mass flow present in a_p will cancel out at convergence with other similar terms generated by the remaining advection contributions. Therefore, it is not necessary to add it to a_p .

The approximation of the north advection transport rate for the lower node (at $J = M2 - 1$) also requires a special treatment in this case, since it too may refer to the undetermined boundary nodal value. By using the same modified scheme, the contribution of J_{Adv_n} to the coefficients a_s , a_p and b of the discretized equation for node $J = M2 - 1$ now becomes:

$$\begin{aligned}
a_N &= (\rho v_m \Delta x)|_n (A2-1) \\
a_p &= a_N + \underbrace{(\rho v_m \Delta x)|_n}_{\substack{\text{Term will cancel out} \\ \text{at convergence}}} \\
con &= -(\rho v_m \Delta x)|_n \frac{Flux_m}{\Gamma} [A2 \cdot (\delta y)_n - (\delta y)_{n+}] \\
\text{where } A2 &= \frac{((\delta y)_{nn} + (\delta y)_{n+})^2 - (\delta y)_{nn}^2}{((\delta y)_{nn} + (\delta y)_n)^2 - (\delta y)_{nn}^2}
\end{aligned} \tag{4.26}$$

Again, the modifications described in this section are only applied in the case of a specified (given) diffusion flux at the top boundary and when the mass flow rate at the south face of the CV in figure 4.7 is in the negative y direction.

4.3.6 ADDITIONAL DETAILS

The aforementioned discretized equations must be adapted to solve the velocity and temperature variables. The values of Γ_ϕ , S_C , and S_p are specifically assigned and modified prior to the calculation of the coefficient in these equations and their solution.

In the discretized x and y momentum equations (for u and v), Γ_ϕ is set equal to the dynamic viscosity of the fluid in regions occupied by the flow. However, it is set to a very high value (10^{30}) in the control volumes located in solid regions with zero velocity (such as the plates). This strategy, with the use of the conductance analogy, Eq. (4.10), to interpolate Γ_ϕ , ensures adequate treatment of the diffusion effects at interfaces between the fluid and the solid regions [Patankar (1980)].

In this work, the term S_p is equal to zero for the velocity components u and v . The constant source term S_C contains the volume-averaged pressure gradient force acting on the fluid: thus

$$S_C^u = \left(-\frac{\partial p}{\partial x} \right)_{Vol.Av.} = \left[\frac{p_P - p_E}{(\delta x)_e} \left(\frac{\Delta x \Delta y}{2} \right) + \frac{p_W - p_P}{(\delta x)_w} \left(\frac{\Delta x \Delta y}{2} \right) \right] \div \Delta x \Delta y \quad (4.27)$$

This equation reduces to:

$$S_C^u = \left(-\frac{\partial p}{\partial x} \right)_{Vol.Av.} = \frac{p_P - p_E}{2(\delta x)_e} + \frac{p_W - p_P}{2(\delta x)_w} \quad (4.28)$$

Similarly, the volume-averaged pressure gradient and the S_C term for v are given by:

$$S_C^v = \left(-\frac{\partial p}{\partial y} \right)_{Vol.Av.} = \frac{p_P - p_N}{2(\delta y)_n} + \frac{p_S - p_P}{2(\delta y)_s} \quad (4.29)$$

In the energy equation, Γ_ϕ represents the thermal conductivity divided by the specific heat at constant pressure: this diffusion coefficient is assigned as follows:

$$\begin{aligned} \Gamma_\phi &= \frac{k_{fluid}}{c_{P fluid}} && \text{in fluid regions} \\ \Gamma_\phi &= \frac{k_{solid}}{c_{P solid}} && \text{in solid regions} \end{aligned} \quad (4.30)$$

Once more, S_P is set to zero in the energy equations for the problems of interest in this work. If the plate temperature is fixed, S_C is also set to zero. However, for a fixed surface heat flux condition, S_C is set to the implied volumetric heat generation value for solid volumes:

$$\begin{aligned} S_C^T &= 0 && \text{For constant plate temperature case.} \\ S_C^T &= Q_{Vol.} && \text{For constant plate heat flux case.} \end{aligned} \quad (4.31)$$

4.3.7 DISCRETIZED PRESSURE EQUATIONS

The discretized pressure equations are obtained by discretizing the continuity equation, and then amalgamating it with suitable forms of the discretized momentum equations derived earlier. The general strategy here consists of defining "pseudo-velocities" using the discretized momentum equations and using the continuity relation to form the pressure equation, as described by Ferziger and Peric (1996) and Baliga and Atabaki (2006). First, the discretized equation for the u velocity component is cast as follows:

$$u = \frac{\sum a_{nb}^u u_{nb} + b_{no\ p.\ cont.}^u}{a_p^u} + \left(-\frac{\partial p}{\partial x} \right)_{Vol.\ Av.} \frac{\Delta x \Delta y}{a_p^u} \quad or, \quad (4.32)$$

$$u = \hat{u} + d_u \left(-\frac{\partial p}{\partial x} \right)_{Vol.\ Av.}$$

Here, \hat{u} and d_u are defined as follows:

$$\hat{u}_p = \frac{\sum a_{nb}^u u_{nb} + b_{no\ p.\ cont.}^u}{a_p^u} \quad (4.33)$$

$$d_u = \frac{\Delta x \Delta y}{a_p^u}$$

A similar treatment is applied to the discretized y -momentum equations, yielding the following relations:

$$\hat{v}_p = \frac{\sum a_{nb}^v v_{nb} + b_{no\ p.\ cont.}^v}{a_p^v} \quad (4.34)$$

$$d_v = \frac{\Delta x \Delta y}{a_p^v}$$

The continuity equation is then used to find a pressure field that would induce velocities that satisfy mass conservation. The mass-conserving velocity at each CV face, denoted with the " m " subscript, is defined as shown in this example for the east CV face:

$$(u_m)_e = \hat{u}_e + (d_u)_e \left(-\frac{\partial p}{\partial x} \right)_e \quad (4.35)$$

where the pressure gradient is approximated as follows:

$$\left(-\frac{\partial p}{\partial x} \right)_e = \frac{(p_P - p_E)}{(\delta x)_e} \quad (4.36)$$

In equation (4.35), the values of \hat{u}_e and $(d_u)_e$ are obtained by linearly interpolating the nodal values to the desired location of the east face of the CV. Similar expressions are derived for the other mass-conserving velocities. The continuity equation (4.1) is then integrated over the CV for node P (see figure 4.4) and approximated as follows:

$$(\rho u_m \Delta y)_e - (\rho u_m \Delta y)_w + (\rho v_m \Delta x)_n - (\rho v_m \Delta x)_s = 0 \quad (4.37)$$

The reader might have noticed that no time integration was performed: this is because, as the fluid mass density is considered constant in this work, its time derivative is nil in the continuity equation. If the mass-conserving velocities are inserted into equation (4.37), the discretized pressure equation is obtained.

$$a_P^p p_P = a_E^p p_E + a_W^p p_W + a_N^p p_N + a_S^p p_S + b^p \quad (4.38)$$

where,

$$a_E^p = \frac{\rho (d_u)_e \Delta y}{(\delta x)_e}; \quad a_W^p = \frac{\rho (d_u)_w \Delta y}{(\delta x)_w}$$

$$a_N^p = \frac{\rho (d_v)_n \Delta x}{(\delta y)_n}; \quad a_S^p = \frac{\rho (d_v)_s \Delta x}{(\delta y)_s} \quad (4.39)$$

$$a_P^p = a_E^p + a_W^p + a_N^p + a_S^p$$

$$b^p = \rho \hat{u}_w \Delta y - \rho \hat{u}_e \Delta y + \rho \hat{v}_s \Delta x - \rho \hat{v}_n \Delta x$$

These equations are then solved to obtain the new pressure field needed to compute the velocities. The mass flow rates at the CV face are subsequently updated by using the solved pressure field in the mass-conserving velocities, akin to equation (4.35). These mass flow rates are stored and latter used in the calculation of the advection effects in the discretized transport equation coefficients. At this stage, all discretized equations in the fluid flow region have been derived.

4.3.8 TREATMENT OF SOLID REGIONS

When control volumes in the FVM grid fall in solid regions, the strategy consists of forcing appropriate values of the dependent variable in such regions. This done for the velocity components u and v , by modifying the coefficients in the discretized momentum equations as follows:

$$\begin{aligned} a_p^{u,v} &= 1 \\ a_{nb}^{u,v} &= 0 \\ b^{u,v} &= 0 \end{aligned} \tag{4.40}$$

Thus, the velocity is set to zero throughout the solid control volumes. The treatment for discretized pressure equations coefficients is similar, but additional modifications are necessary. First, the interpolated values of \hat{u} , \hat{v} , d_u and d_v at nodes in the solid regions are set to zero. Therefore, any coefficient linking a fluid node to a solid neighbor is automatically equal to zero. In other words, the nodal pressure values inside a plate region are totally decoupled from the rest of the fluid domain. Thus, pressure in the solid region can be fixed arbitrarily to any convenient value. For every solid volume, the discretized pressure equations coefficients are modified as follows:

$$\begin{aligned} a_p^p &= 1 \\ a_{nb}^p &= 0 \\ b^p &= 0 \quad (\text{set arbitrarily}) \end{aligned} \tag{4.41}$$

Due to the changes mentioned above, the mass conserving velocities u_m and v_m at nodes inside solid regions are also forced to zero. Hence the corresponding mass flow rates, used in the QUICK scheme to approximate advection effects, are also equal to zero at nodes inside solid regions:

$$(\rho u_m \Delta y) = (\rho v_m \Delta x) = 0 \quad \text{at any solid boundary} \quad (4.42)$$

Furthermore, the volume-averaged pressure gradient calculation is slightly modified for control volumes adjacent to solid regions. Since the pressure stored at nodes inside solid regions has no physical relevance, the average gradient is computed using only the values at nodes in the fluid regions: thus, for example,

$$\left(-\frac{\partial p}{\partial x} \right)_{Vol.Av.} = \frac{W_P W_E \left(\frac{P_P - P_E}{(\delta x)_e} \right) + W_P W_W \left(\frac{P_W - P_P}{(\delta x)_w} \right)}{W_P W_E + W_P W_W} \quad \text{where,}$$

$$W = 0 \quad \text{for a solid control volume} \quad (4.43)$$

$$W = 1 \quad \text{for a fluid control volume}$$

and, similarly, for the derivative with respect to y :

$$\left(-\frac{\partial p}{\partial y} \right)_{Vol.Av.} = \frac{W_P W_N \left(\frac{P_P - P_N}{(\delta y)_n} \right) + W_P W_S \left(\frac{P_S - P_P}{(\delta y)_s} \right)}{W_P W_N + W_P W_S} \quad (4.44)$$

The coefficients in the discretized equations for temperature are treated with respect to the type of problem being solved. If the plate temperature is considered to be at a fixed value, the following modifications are applied in the solid regions:

$$a_P^T = 1; a_{nb}^T = 0; b^T = T_{WALL} \quad (4.45)$$

If the plate heat transfer is specified, no modifications are required in the solid regions.

4.4 SOLUTION OF THE DISCRETIZED EQUATIONS

4.4.1 OVERVIEW OF SOLUTION PROCEDURE

A modified version of the iterative sequential iterative variable adjustment (SIVA) procedure developed by Masson, Saabas and Baliga (1994) is used to solve the discretized equations. This method is summarized below.

- 1: Provide initial values of the dependent variables u , v , P and T . Also set $\hat{u} = u$, $\hat{v} = v$, $d_u = 0$ and $d_v = 0$. Compute mass flow rate at CV faces.
- 2: Start calculations to advance the solution from t to $t + \Delta t$.
- 3: Calculate coefficients in the discretized u equations, without accounting for the contributions of the pressure gradient terms. Store a_p^u and $b_{no P.Cont.}^u$, which are needed to compute \hat{u} and d_u .
- 4: Add pressure contribution to b^u ; under-relax coefficients; and modify coefficients for control volumes in solid regions.
- 5: Calculate the new u velocity field, using the block-correction algorithm and the appropriate solvers (standard line-by-line penta-diagonal matrix algorithm (PDMA) or cyclic PDMA depending on the type of domain).
- 6: Compute \hat{u} and d_u .
- 7: Calculate coefficients in the discretized v equations, without accounting for the contribution of the pressure gradient terms. Store a_p^v and $b_{no P.Cont.}^v$, which are needed to compute \hat{v} and d_v .
- 8: Add pressure contribution to b^v ; under-relax coefficients; and modify coefficients for control volumes in solid regions.
- 9: Calculate the new v velocity field, using the block-correction algorithm and the appropriate solvers (standard line-by-line PDMA or cyclic PDMA depending on the type of domain).

- 10: Compute \hat{v} and d_v .
- 11: Calculate coefficients in the discretized pressure equations; do not apply under-relaxation; and modify coefficients for control volumes in solid regions.
- 12: Calculate the new pressure field, using the block-correction algorithm and the appropriate solvers (standard line-by-line tri-diagonal matrix algorithm (TDMA) or cyclic TDMA depending on the type of domain).
- 13: Update mass-conserving velocities and calculate the new mass flow rates at the CV faces.
- 14: Update the pressure field with under-relaxation.
- 15: Calculate coefficients in the discretized temperature equation; modify these coefficients for control volumes in solid regions, if needed.
- 16: Calculate the new temperature field, using the block-correction algorithm and the appropriate solvers (standard line-by-line PDMA or cyclic PDMA depending on the type of domain).
- 17: Inspect normalized residues and other convergence monitoring variables against specified convergence criteria. If convergence is attained, store all converged dependent variable values ϕ into the "old" variable array ϕ^0 ; start computations for the new time step (go to Step 2). However, if convergence for the current time step has not been reached, continue computations by restarting a new internal iteration from step 3.

This strategy efficiently solves the non-linear discretized equations by seeking full convergence at each time step. The method has proven to be rugged enough to solve various types of problems, involving steady and unsteady flows. Under-relaxation is applied to the velocity and temperature coefficients to provide stability of this iterative solution procedure. However, the discretized pressure equations are not under-relaxed prior to solving: the new pressure field is solved without any under-relaxation. Only afterwards, a modified under-relaxation is applied [Baliga and Atabaki (2006)]. The block-correction algorithm and the line-by-line solvers used in this procedure are presented in the next subsection.

4.4.2 DESCRIPTION OF LINE-BY-LINE CYCLIC SOLVERS

The dependent variables are computed iteratively by solving the linearized and decoupled discretized equations using multi-directional sweeping line-Gauss Seidel solvers. The line sweeps head back and forth over the domain, alternately in the x and y directions as shown in figure 4.8.

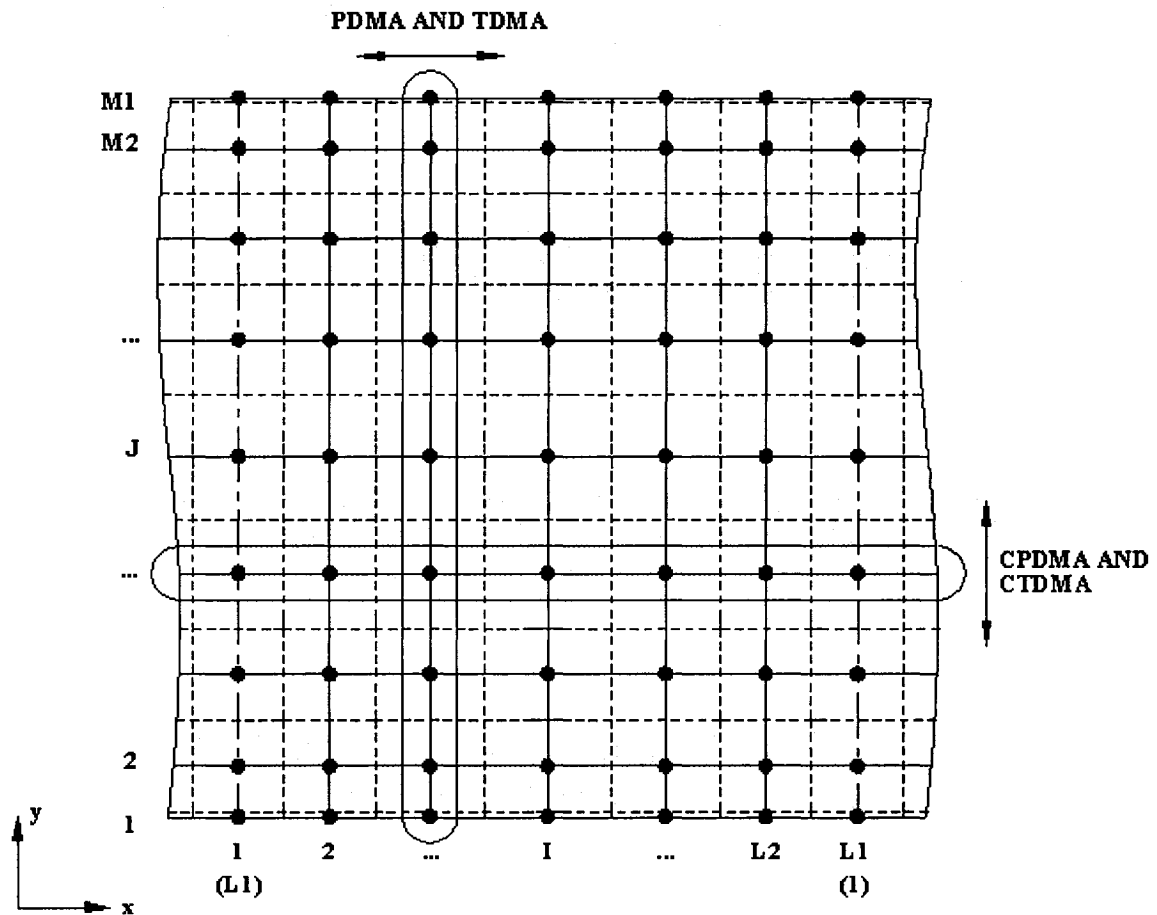


Figure 4.8 Sweeps in the line-by-line iterative solvers.

In the discretized pressure equations, each node is linked to just two neighbors along the grid lines. Therefore, a line-by-line tridiagonal matrix algorithm (TDMA) is used to solve the equations over non-cyclic domains; for sweeps over cyclic domains, a line-by-line cyclic tri-diagonal matrix algorithm (CTDMA) is used.

In the discretized velocity and temperature equations assembled using the QUICK scheme, a node could be linked with up to four neighbors, two each in the positive and negative directions along a grid line. Thus, a line-by-line pentadiagonal matrix algorithm (PDMA) solver is used to solve these equations over non-cyclic domains; for sweeps over cyclic domains, a line-by-line cyclic PDMA (CPDMA) is used.

The TDMA and CTDMA techniques are well-known and are commonly used [Patankar (1980); Press et al. (1992)]. The PDMA and CPDMA, inspired from the TDMA and CTDMA, have been derived by Sebben and Baliga (1995). Since the descriptions of these algorithms are quite extensive, the reader is referred to the aforementioned journal paper for a complete presentation.

To speed up convergence, a block-correction algorithm is used before performing the above-mentioned line sweeps. This procedure is presented in the next subsection.

4.4.3 BLOCK-CORRECTION PROCEDURE

The block-correction method is a simple and efficient way to speed up convergence of the line-by-line iterative solvers. It consists of adding uniform corrections to each line of the unconverged variable field ($\phi_{i,j}^*$) prior to the application of the line-by-line solver. A correction value $\bar{\phi}_i$ is obtained for each line and applied uniformly over the whole i^{th} grid line $\phi_{i,j}^*$ values. Similarly, $\bar{\phi}_j$ corrections are computed and applied for every j^{th} line. For additional details and the rationale behind these methods the reader is referred to the works of Patankar (1980) and Kelkar and Patankar (1989). The coefficients and equations for line corrections $\bar{\phi}_i$ and $\bar{\phi}_j$ are described below.

The details of the equation for $\bar{\phi}_i$ are presented below. The dependent variable is first expressed as follows:

$$\begin{aligned}
\phi_{i,j} &= \phi_{i,j}^* + \bar{\phi}_i \cdot W_{i,j} \\
W_{i,j} &= 0 \text{ for a solid control volume} \\
W_{i,j} &= 1 \text{ for a fluid control volume}
\end{aligned} \tag{4.46}$$

The previous expression is introduced into the discretized equation for ϕ , and the following relation for $\bar{\phi}_i$ is obtained:

$$A_i \bar{\phi}_i = B_i \bar{\phi}_{i+1} + C_i \bar{\phi}_{i+2} + D_i \bar{\phi}_{i-1} + E_i \bar{\phi}_{i-2} + F_i \tag{4.47}$$

In this equation,

$$\begin{aligned}
A_i &= \sum_{j=2}^{M2} (a_{P i,j} \cdot W_{i,j} - a_{NN i,j} \cdot W_{i,j+2} - a_{N i,j} \cdot W_{i,j+1} - a_{SS i,j} \cdot W_{i,j-2} - a_{S i,j} \cdot W_{i,j-1}) \\
B_i &= \sum_{j=2}^{M2} a_{E i,j} \\
C_i &= \sum_{j=2}^{M2} a_{EE i,j} \\
D_i &= \sum_{j=2}^{M2} a_{W i,j} \\
E_i &= \sum_{j=2}^{M2} a_{WW i,j} \\
F_i &= \sum_{j=2}^{M2} (\sum a_{NB i,j} \phi_{NB i,j}^* + b_{i,j} - a_{P i,j} \phi_{i,j}^*)
\end{aligned} \tag{4.48}$$

The equation for $\bar{\phi}_i$ is solved using CPDMA or PDMA algorithms. Zero corrections are imposed at the boundaries with prescribed values of the dependent variables. The $\bar{\phi}_i$ corrections are subsequently added to the individual values of $\phi_{i,j}^*$ over each solved line. An expression for the $\bar{\phi}_j$ correction equation is derived, solved, and applied using the similar steps.

The block-correction algorithm for the discretized pressure equations is simpler, as these equations involve fewer neighbors. Thus, these equations can be solved using TDMA or CTDMA algorithms [Sebben and Baliga (1995)].

4.4.4 UNDERRELAXATION

In order to ensure convergence of the aforementioned iterative solution procedures for the sets of the nonlinear, coupled, discretized equations, implicit underrelaxation is applied to the coefficients in these equations, following the proposal of Patankar (1980):

$$\frac{a_p}{\alpha} \phi_p = \sum a_{nb} \phi_{nb} + b + \left(\frac{1-\alpha}{\alpha} \right) a_p \phi_p^* \quad (4.49)$$

In this equation, ϕ_p^* denotes the value of ϕ_p from the previous inner iteration and α represents the underrelaxation factor, which may have a value ranging from 0 to 1. For pressure, a different type of underrelaxation (explicit) is implemented to update the field. It is applied only after newly calculated pressure field is computed:

$$p = \alpha p^{NC} + (1-\alpha) p^* \quad (4.50)$$

In this equation, p^{NC} is the newly calculated pressure field, obtained by solving the discretized pressure equations without underrelaxation; and p^* is the unconverged value of p from the previous iteration.

Individual values of α are prescribed for each dependent variable. These underrelaxation parameters are set the highest possible value that can be used without incurring divergence of the iterative schemes. Since there is no straightforward way to determine the optimal values for α , they must be set in accordance with previous experience or based on heuristic (trial) calculations. In this work, relatively high values of α (0.75 to 1.0) were used to solve the unsteady problems.

CHAPTER 5 – RESULTS AND DISCUSSION

The results of the experimental and numerical investigations are presented in this chapter.

5.1 RESULTS OF THE EXPERIMENTAL INVESTIGATIONS

As was stated earlier in the thesis, the emphasis in this experimental investigation was on single hot-wire measurements in the spatially periodic fully-developed region of turbulent flows in a rectangular interrupted-plate duct, akin to that shown schematically in Figure 1.3. Specifically, the aim was to obtain turbulence power spectrums and Strouhal numbers for the aforementioned flows. The results of this experimental investigations are presented and discussed in this section.

5.1.1 BENCHMARKING OF HOT-WIRE APPARATUS AND PRELIMINARY EXPERIMENTS

The hot-wire equipment was benchmarked by measuring the frequency of vortices shed from a cylinder in unconfined cross flow. A lot of experimental data are available for this particular unsteady flow, since this is a classic problem in fluid mechanics.

These experiments were performed in an open-circuit wind tunnel in the Aerodynamics Laboratory at McGill University. The test section of this tunnel is 0.914 meter wide by 0.610 meter high. The turbulence intensity was under 1%, thanks to a well-designed inlet section. A stainless steel cylinder, 1-inch (2.54 cm) diameter and 0.914 meter long, was installed vertically and in the center of the test section of this wind tunnel. The blockage area was negligible: so no correction was applied to the measured freestream velocity, which was varied from about 1.35 m/s to 26.17 m/s. This freestream velocity was measured with a pitot tube installed at the same axial position as that of the cylinder. The dynamic pressure required to compute this velocity was measured with a highly accurate Askania-type manometer. The atmospheric pressure was obtained with a mercury-in-glass barometer and the air temperature was measured with a thermocouple installed in

the laboratory. The fluid density and kinematic viscosity were computed with the ideal gas law and the Sutherland law, respectively. For these conditions, the Reynolds number, based on the cylinder diameter and the freestream velocity, varied from 2220 to 43350.

The single hot wire was oriented parallel to the cylinder axis and measurements were obtained at two positions, 1.5 and 4.5 diameters downstream from the center of the cylinder. Instantaneous velocity measurements were acquired digitally, and they were used to calculate ensemble-averaged power spectrums and obtain the corresponding vortex shedding frequencies (as described in chapter 2). These frequencies were then used to calculate the Strouhal numbers based on the cylinder diameter and the freestream velocity. Results of this benchmarking experiment are presented and compared to the data of Norberg (1993) in figure 5.1.

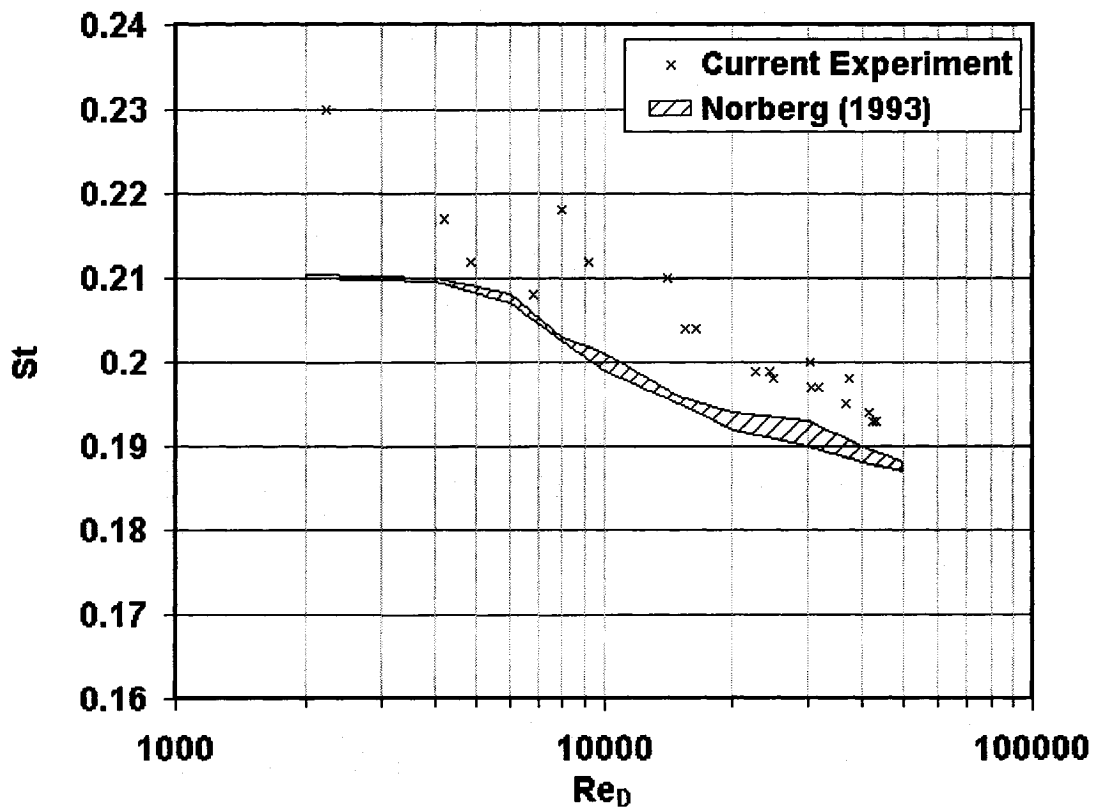


Figure 5.1 Strouhal number of vortex shedding from a cylinder in unconfined crossflow.

The largest discrepancy between the results obtained in this work and those of Norberg (1993) is a 9.5% relative difference of the Strouhal number at the lowest value of the Reynolds number. The average relative difference between these results is of the order of 5%. As the Reynolds number increases, the differences between these sets of results decrease appreciably. Considering the large scatter in the published results for this test case [Schlichting (1955); Norberg (1993)], and also differences in the test parameters such as wire sampling positions and a different length-to-diameter ratio (L/D) of the cylinder, these results were considered satisfactory.

Once the hot-wire apparatus and sampling methods were validated in the aforementioned benchmarking experiments, attention was focused on establishing the repeatability of measurements in the rectangular interrupted-plate duct. With respect to the notation in the schematics given on the right-hand side of figure 5.2, the hot-wire probe was inserted in hole H2 at position P8 and many power spectrums were obtained at essentially same values of the Reynolds number (Kays and London definition; see chapter 2). Sample results from three repeatability runs for a nominal Reynolds number of 20000 are shown in figure 5.2.

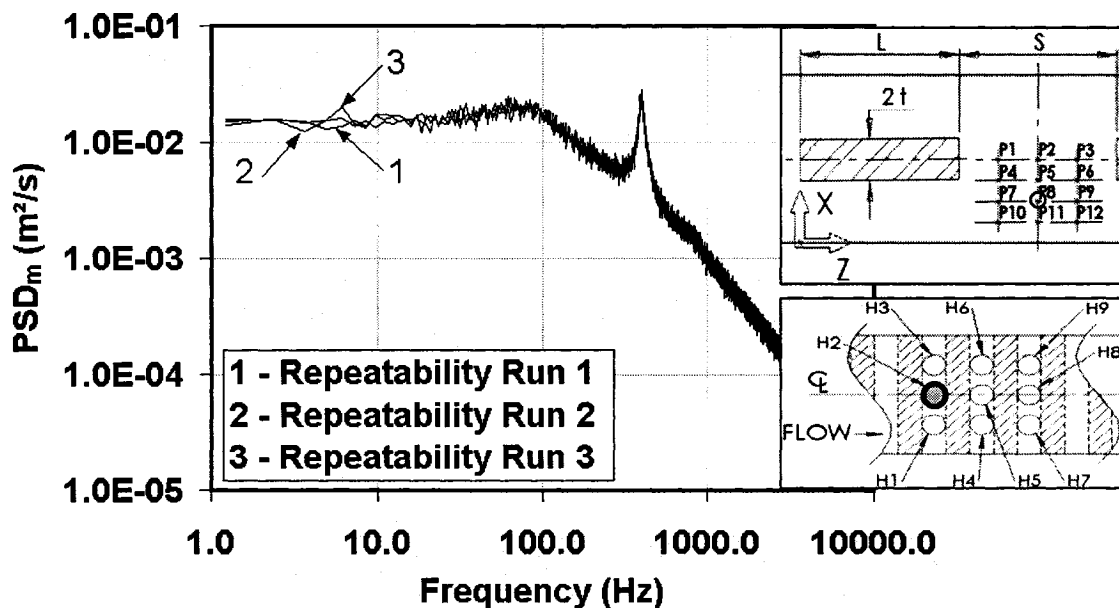


Figure 5.2 Power spectrums showing repeatability (H2, P8, $Re \approx 20000$).

The results provided in Figure 5.2 show that all three spectrums are essentially identical, thereby confirming that repeatable measurements and results are provided by the hot-wire apparatus and procedures used in this work.

Once the results were shown to be repeatable, the vertical symmetry of the measurements was investigated. With reference to notation in the schematics on the right-hand side of figure 5.3, the power spectrums were obtained from measurements with the probe in hole H2 at position P5 and also at its mirror vertical symmetry point on the other side of the duct centerline in the x direction. The results are presented in figure 5.3 and 5.4 for Reynolds numbers of 5000 and 20000 (nominal), respectively. These experiments were performed to assess the geometric precision of the assembled ducts, the precision of the wire positioning method, and the blockage effects of the hot-wire probe.

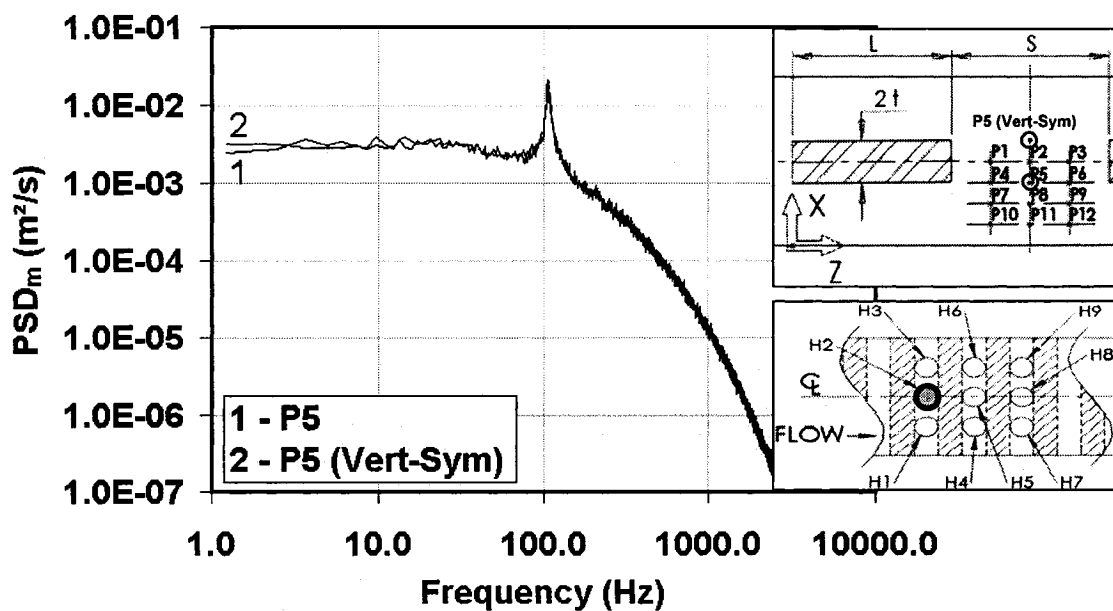


Figure 5.3 Power spectrums showing vertical symmetry
(H2, P5, and mirror position): $Re \approx 5000$.

The power spectrums for positions P5 and P5 (Vert-Sym) are essentially identical in both figures 5.3 and 5.4. These results confirm that the interrupted-plate duct was assembled

with excellent precision, the hot-wire positioning system is also very precise, and effects of flow blockage by the hot-wire probe are essentially negligible.

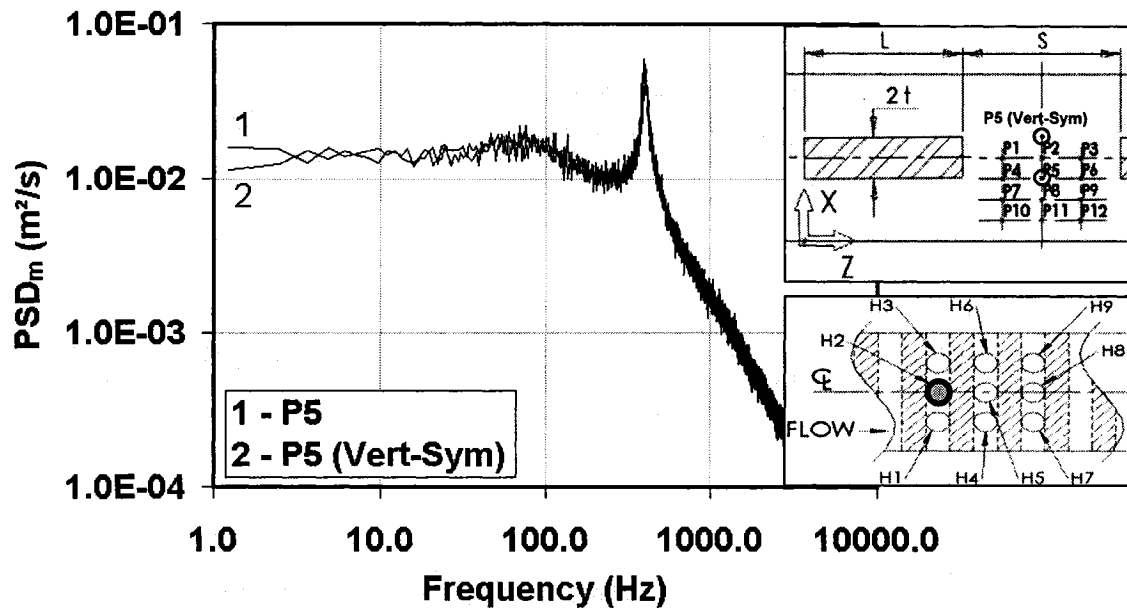


Figure 5.4 Power spectrums showing vertical symmetry (H2, P5, and mirror position): $Re \approx 20000$.

5.1.2 RESULTS OF LATERAL SYMMETRY AND SPATIAL PERIODICITY INVESTIGATIONS

Once the hot-wire apparatus was benchmarked and the aforementioned preliminary experiments were finished, the symmetry of the turbulence statistics was investigated in the lateral direction (y direction with respect to the schematic in figures 5.2) of the duct. The hot-wire probe was inserted at three different lateral positions (holes H1, H2, and H3) at location P8. These investigations were conducted at two different nominal values of the Reynolds numbers: 5000 and 20000. The resulting power spectrums and their respective sampling positions are shown in figures 5.5 and 5.6.

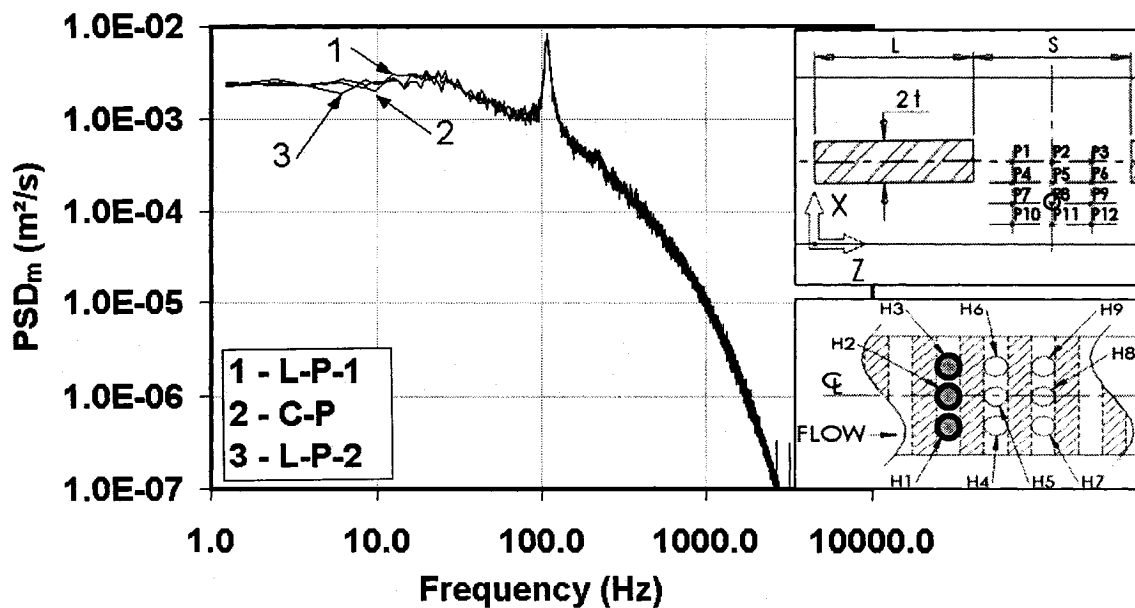


Figure 5.5 Power spectrums showing lateral symmetry (P8): $Re \approx 5000$.

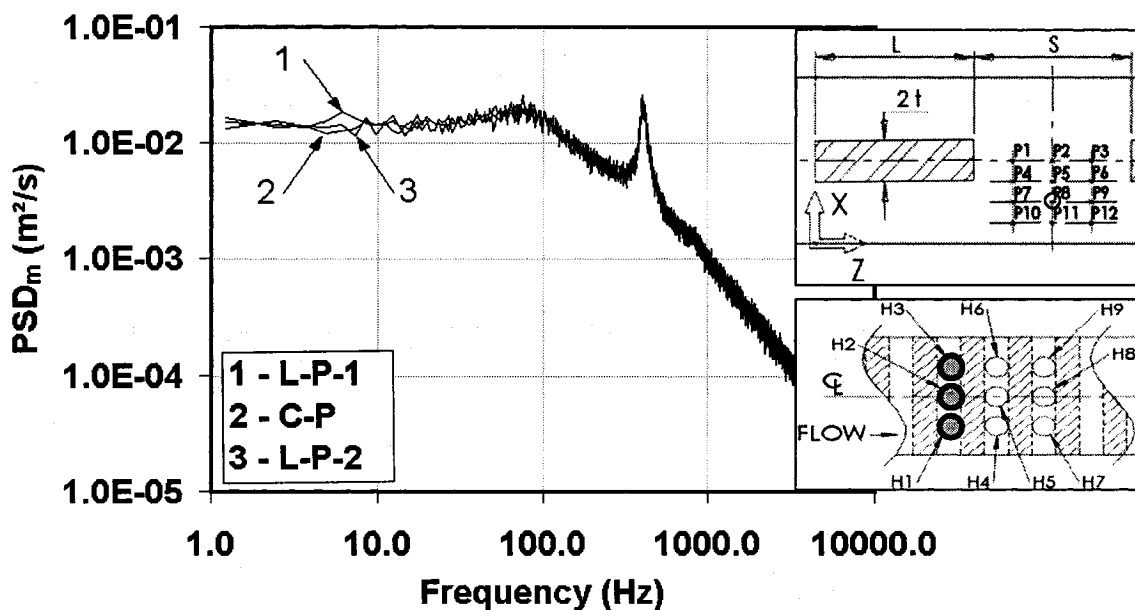


Figure 5.6 Power spectrums showing lateral symmetry (P8): $Re \approx 20000$.

The power spectrums are essentially identical for all three lateral positions ($H1$, $H2$, and $H3$), for both Reynolds number values. Thus, these results show that time-mean turbulent flows of interest here are two-dimensional over at least the central 76.3 mm ($b/2$) portion

of the duct. Past flow visualization experiments (done using paint streakline patterns on the surface of the plates) conducted by McBrien et al. (2000) in the same Reynolds number range also showed this two-dimensionality of the flow over about 80% of the width of the duct. The precise hot-wire measurements undertaken in this work confirm this flow behavior with quantitative results for the first time.

The next objective was to investigate the spatial periodicity of the turbulence statistics in consecutive modules. Power spectrums were obtained in three successive modules (holes H2, H5, and H8) at position P8. Figures 5.7 and 5.8 show the results of this spatial periodicity study for nominal Reynolds number values of 5000 and 20000, respectively.

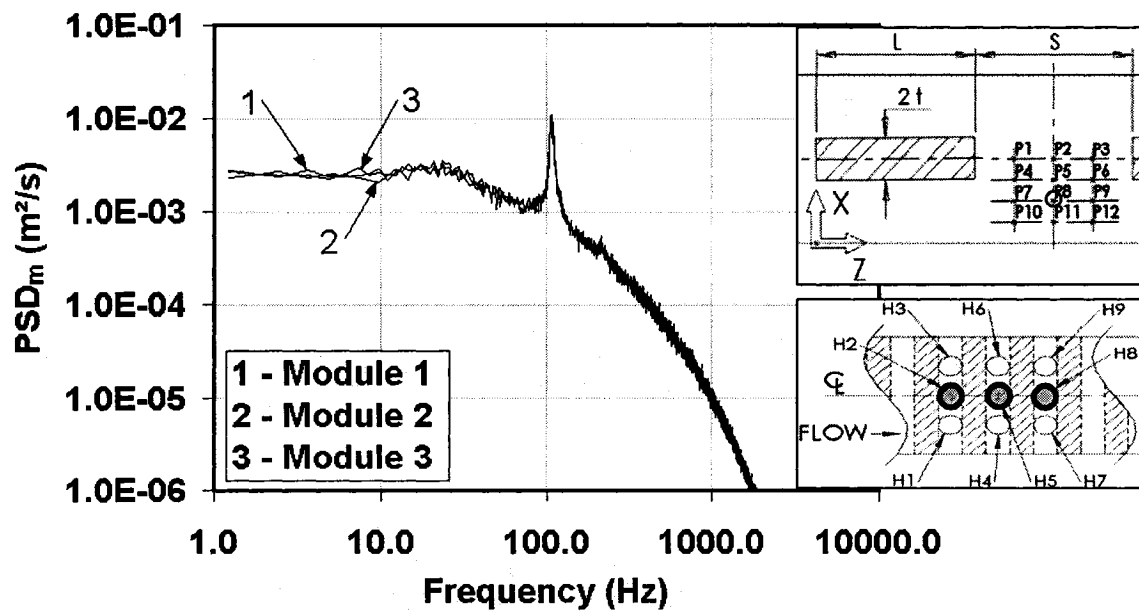


Figure 5.7 Power spectrums showing spatial periodicity in the axial direction (P8): $Re \approx 5000$.

The power spectrums obtained for these three modules are almost identical, for both Reynolds number values, thereby confirming the spatial periodicity of the turbulence statistics in the hot-wire measurement section. The existence of this flow regime in interrupted-surface geometries has been established in earlier experiments involving time-mean heat transfer data [Joshi and Webb (1987)] and wall static pressure

measurements [McBrien and Baliga (1988), Candanedo et al. (2003)]. However, this is the first time that it has been shown experimentally that the turbulence power spectrums also display spatially periodic behavior in such flows.

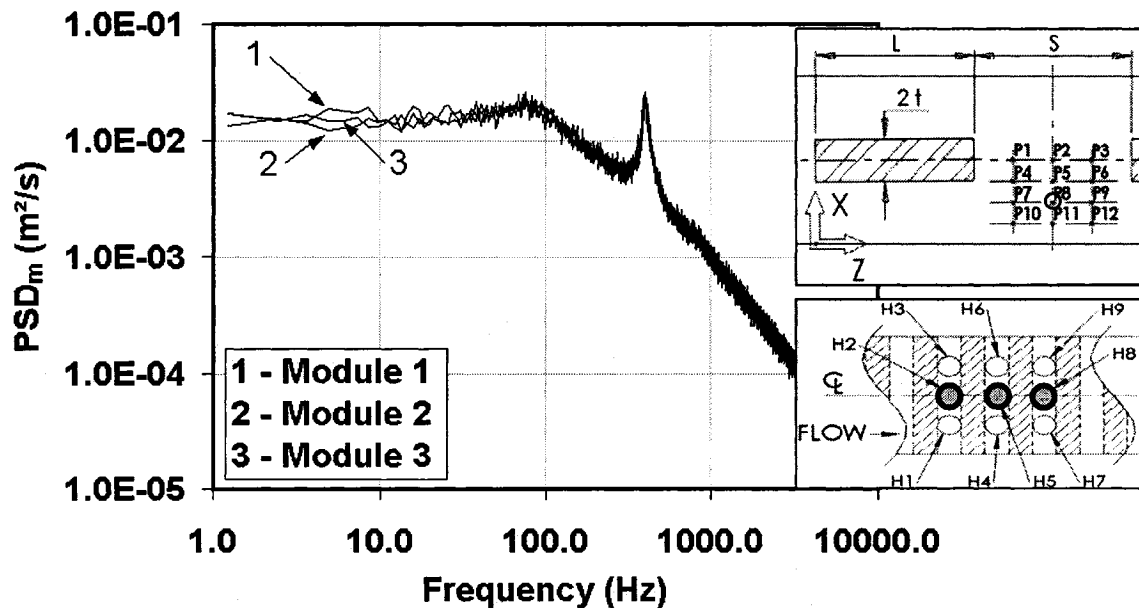


Figure 5.8 Power spectrums showing spatial periodicity in the axial direction (P8): $Re \approx 20000$.

5.1.3 TURBULENCE POWER SPECTRUMS

After the completion of the time-mean flow two-dimensionality and spatial periodicity investigation, as demonstrated in the previous subsection, ensemble-averaged power spectrums were obtained for all 12 positions in the longitudinal cross-sectional plane of the duct (see figures 3.3 and 5.2) in hole number H2, for Reynolds numbers ranging from 2000 to 30000. For the sake of conciseness, only a selection of these power spectrums is presented in this section.

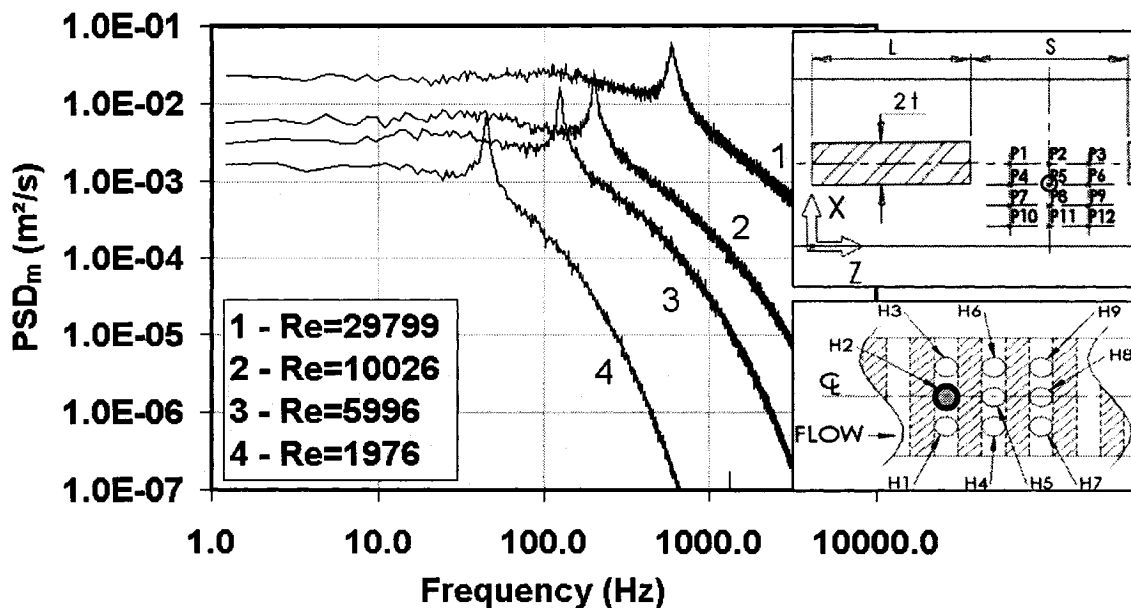


Figure 5.9 Power spectrums at position P5 and hole H2.

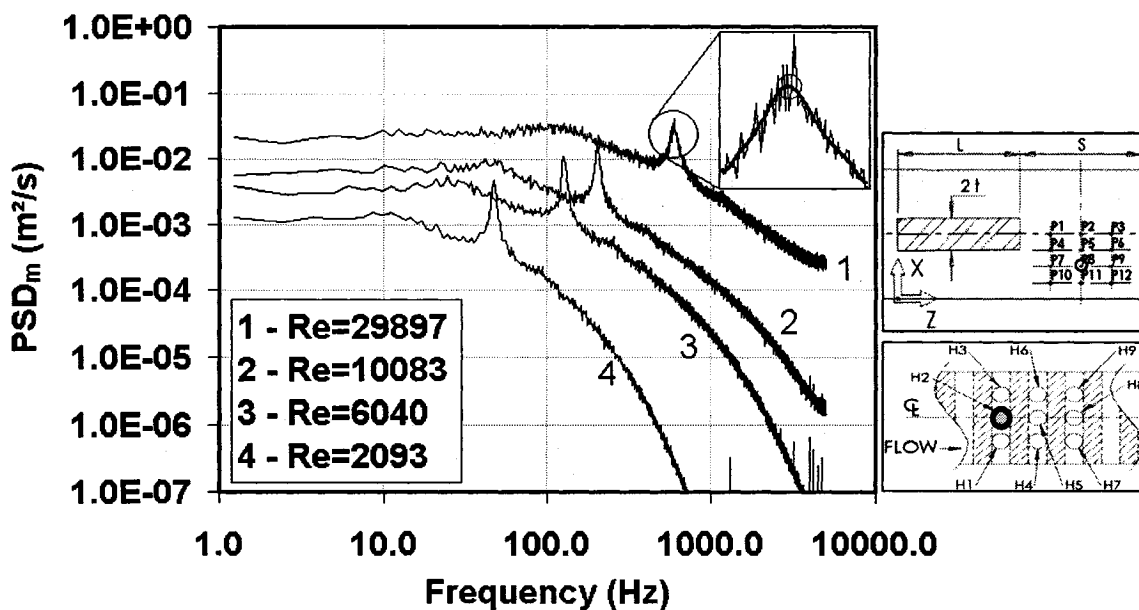


Figure 5.10 Power spectrums at position P8 and hole H2.

Figures 5.9, 5.10, and 5.11 show power spectrums measured at positions P5, P8, and P11, respectively, all with the probe in hole H2. Each figure contains four curves showing the ensemble-averaged power spectrums obtained at four different values of Reynolds number. The sampling positions are shown on the schematics on the right of these

figures. An additional subset schematic, provided in figure 5.10, shows how the power spectrums were locally curve-fitted using a ninth-order polynomial function and a least-squares regression method in order to find the precise dominant vortex shedding frequency. This procedure was necessary because even the ensemble-averaged spectrums are not sufficiently smooth to provide an unambiguous value of dominant vortex shedding frequency by a simply visual examination.

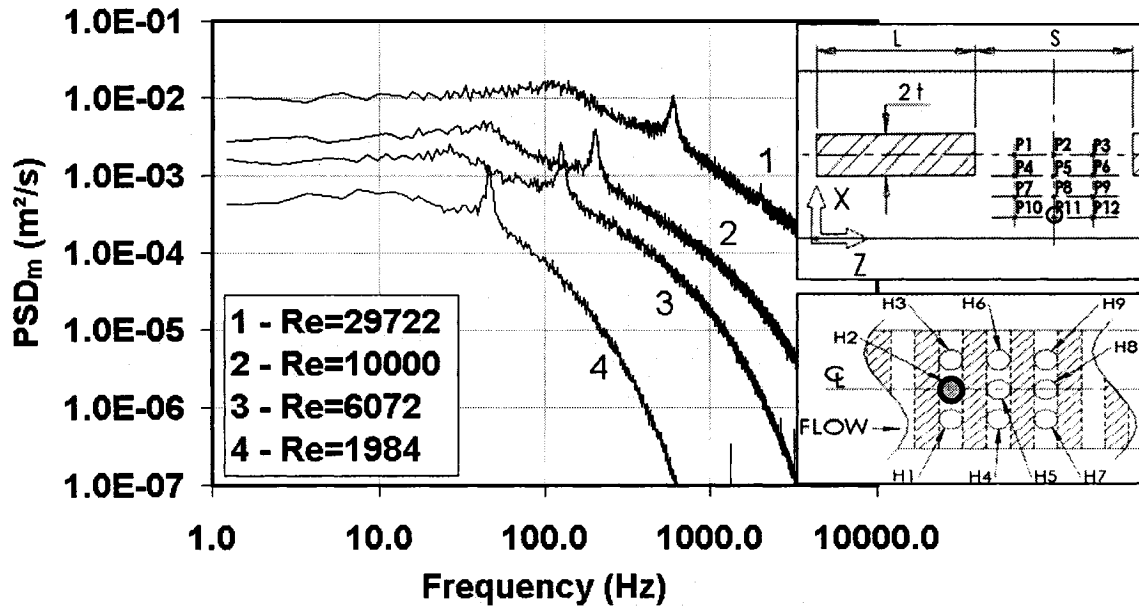


Figure 5.11 Power spectrums at position P11 and hole H2.

The illustrated power spectrums possess a single peak, or spike, which denotes the main vortex shedding frequency. As expected, this frequency increases with the Reynolds number.

Some power spectrums did not show the presence of vortex shedding: when plotted, they do not reveal any spike or dominant vortex shedding frequency. An example of such spectrums, in this case obtained at position P10, is illustrated in figure 5.12. Spectrums showing no or barely discernible vortex shedding were also measured at positions P3, P6 and P7.

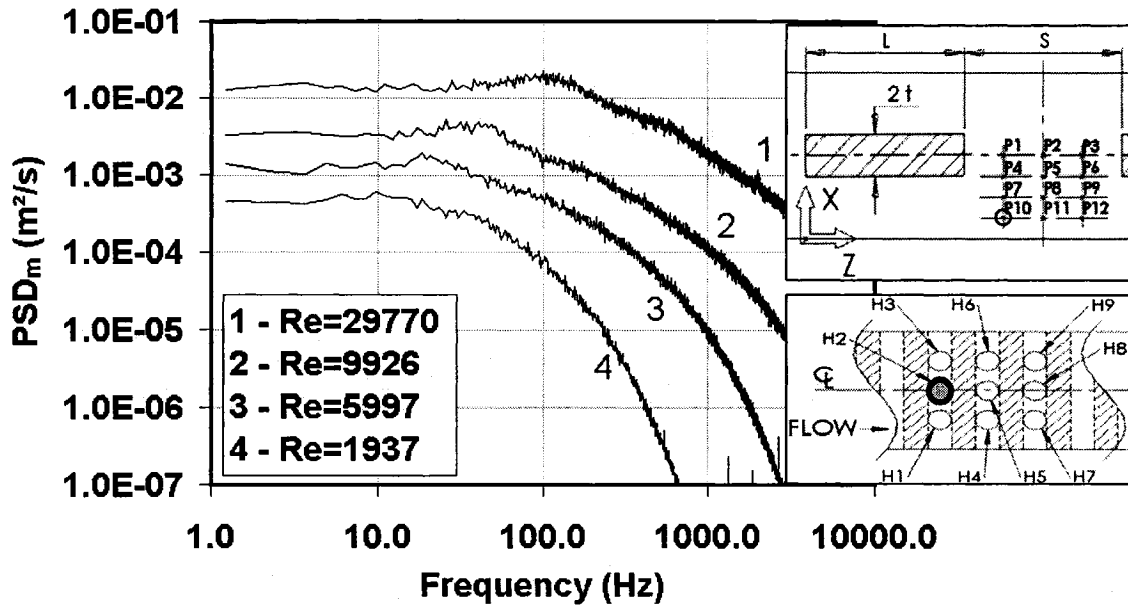


Figure 5.12 Power spectrums at position P10 and hole H2.

At some locations, the spectrums are characterized by the presence of two peaks, as shown in figures 5.13 and 5.14 for positions P1 and P2. In such cases, the magnitude of the first peak (lower frequency) generally surpasses the value of second one. An exception to this observation occurs at position P1 and at a high Reynolds number value of 29888, where both peaks attain almost equal magnitudes. Another exception is observed at position P2 and Reynolds number of 29800 (figure 5.14), where the first frequency peak is barely discernable. In all cases, the frequency of the second peak is essentially twice that of the first one. Such double-peak power spectrums are observed only at positions H1, H2, and H3, along the duct centerline. The double peaks are present when the hot-wire probe is exposed to counter-rotating vortices that are alternatively shed from the bottom and top trailing edges of the plates. The previously shown single-spike power spectrums were sampled at positions lower than the duct centerline, for which the effects of the vortices shed from the top edge were absent or not significant enough to be picked up in these measurements.

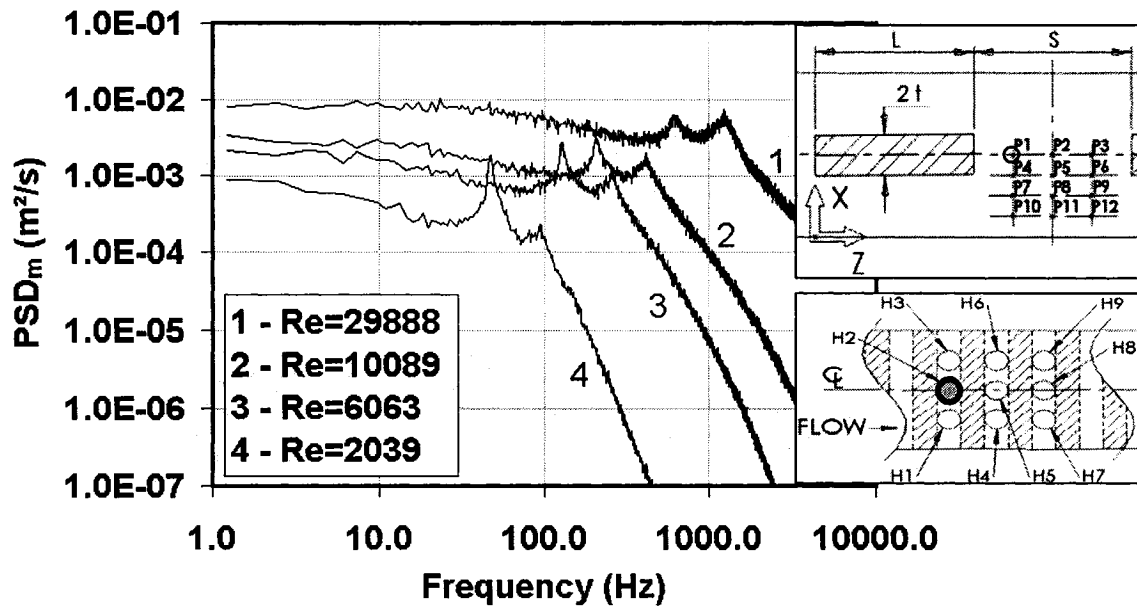


Figure 5.13 Power spectra at position P1 and hole H2.

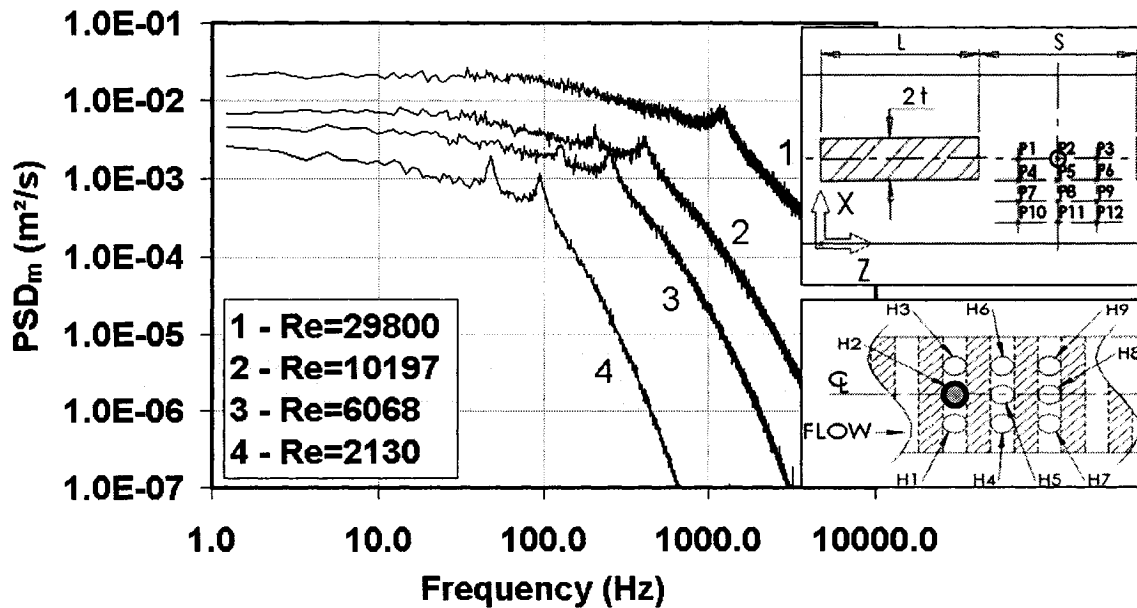


Figure 5.14 Power spectra at position P2 and hole H2.

All power spectra obtained in these experiments were analyzed to obtain the corresponding dominant vortex shedding frequencies. If two spikes were present in a

spectrum, the lower frequency peak was chosen since its magnitude is generally superior to that of the second peak. These frequencies were then used to calculate the Strouhal numbers: these results are presented in the next section.

5.1.4 VORTEX SHEDDING STROUHAL NUMBERS

The dimensionless vortex shedding frequencies, obtained by analyzing the power spectrums, were plotted as functions of the Reynolds number and probe position. These results are presented in figures 5.15, 5.16 and 5.17 for positions where the dominant frequencies were observable over most of the Reynolds number range explored in this work. Each figure displays the Strouhal numbers sampled at probe positions with identical axial locations (z): figure 5.15 shows these values for positions P1 and P4; figure 5.16 shows results for positions P2, P5, P8, and P11; and figure 5.17 displays results for positions P9 and P12. Strouhal numbers were not plotted for positions P3, P6, P7, and P10 because the vortex shedding frequencies were either absent from the spectrums or too weak to be picked up over most of the Reynolds numbers investigated.

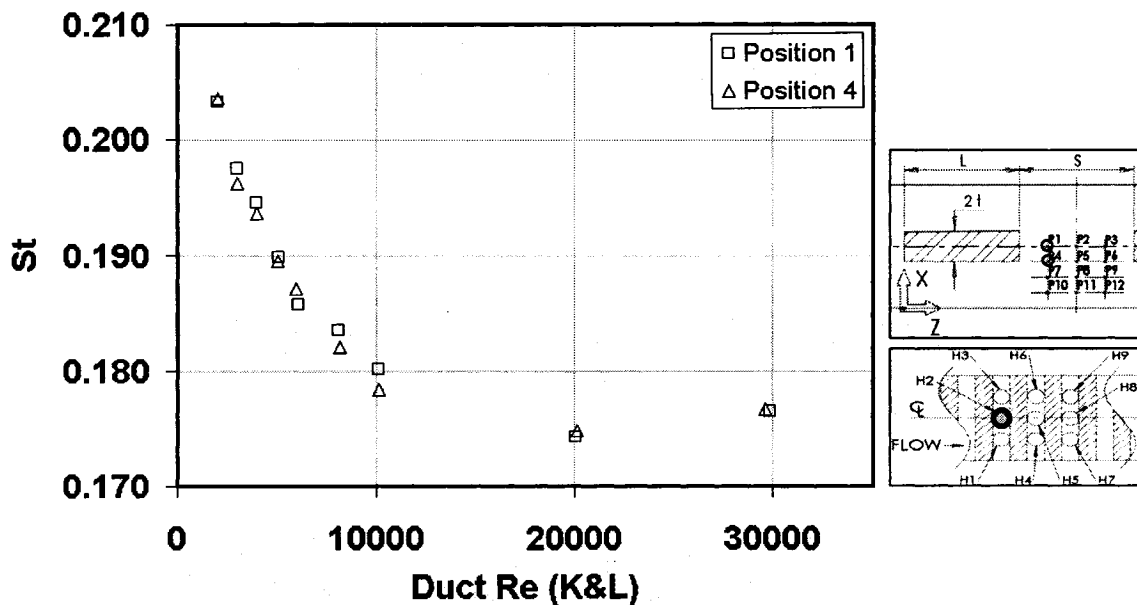


Figure 5.15 Strouhal numbers at positions P1 and P4, in hole H2.

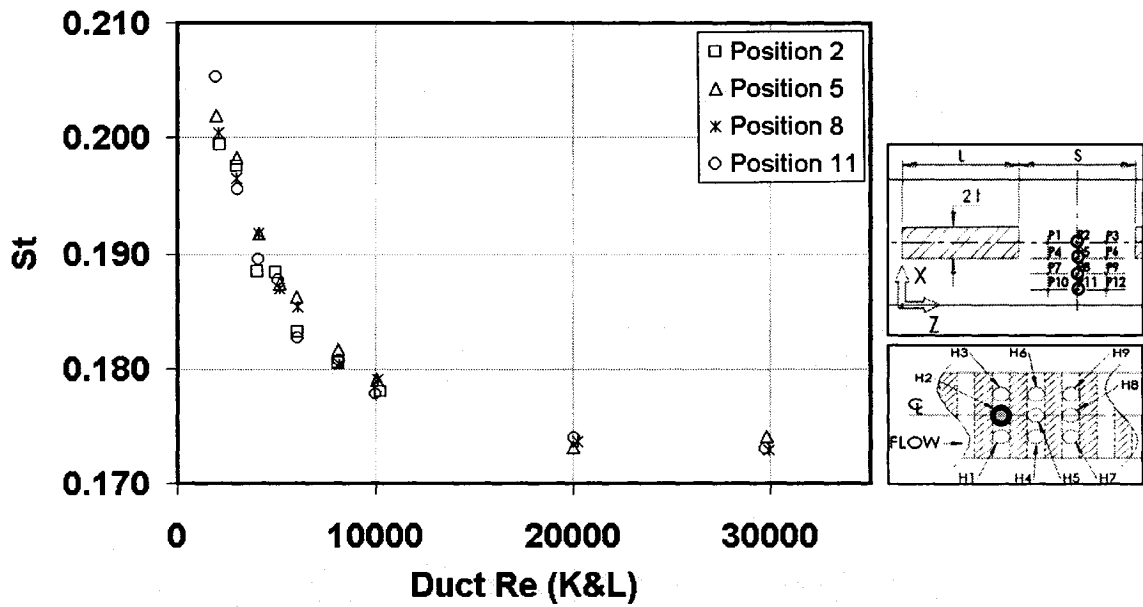


Figure 5.16 Strouhal numbers at positions P2, P5, P8, and P11, in hole H2.

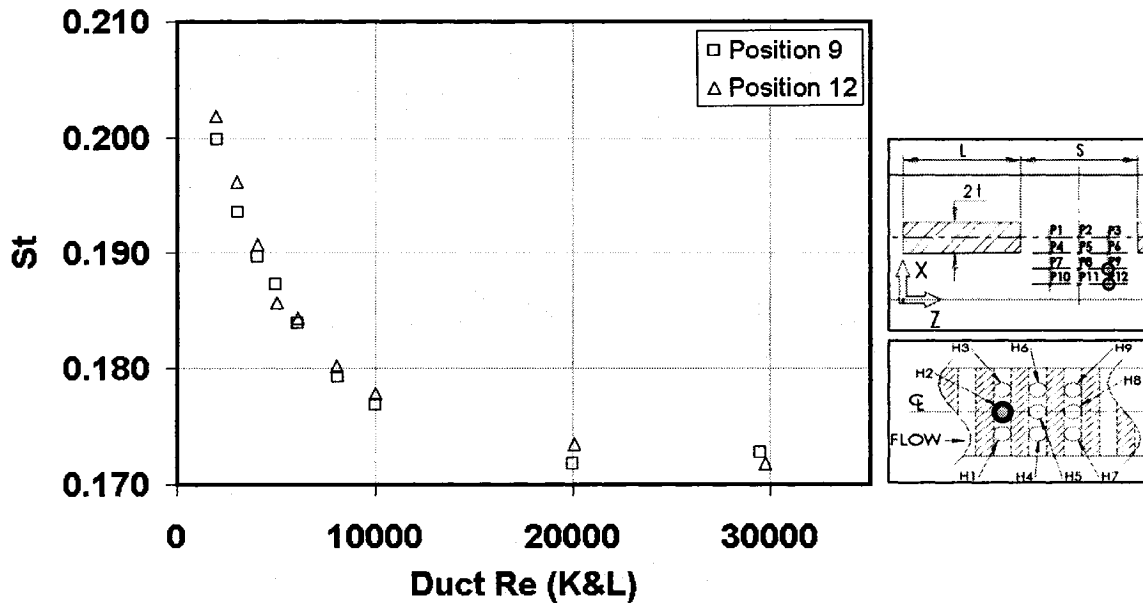


Figure 5.17 Strouhal numbers at positions P9 and P12, in hole H2.

The Strouhal number behavior is made quite clear by the three figures shown above. In most of the cases considered, the values decrease monotonically and asymptote to a

constant value at high Reynolds numbers. An exception is observed at positions P1 and P4, where the Strouhal number distributions show a slightly increasing trend at high Re values.

Additionally, the vortex shedding frequencies are not monochromatic: they depend on sampling position and on the Reynolds number. For same duct axial positions, the Strouhal number distributions shown above do not display any clear dependence on the vertical position. However, if the Strouhal numbers are plotted on a single figure and presented with respect to their axial location, their dependence on the axial position becomes apparent. Figure 5.18 shows such a variation of Strouhal numbers with respect to axial position.

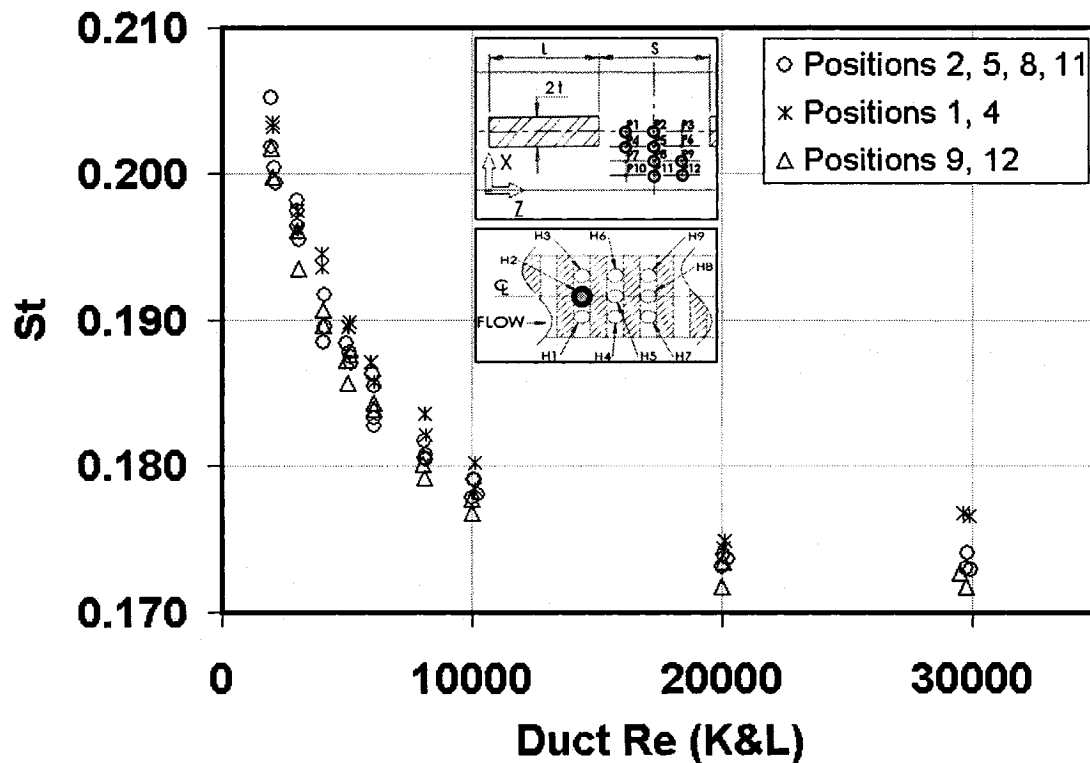


Figure 5.18 Variation of vortex shedding Strouhal numbers with respect to axial position (z), in hole H2.

As shown in the previous figure, a frequency dependence on axial position is observable for Reynolds numbers above 5000. Strouhal numbers sampled at upstream positions (P1, P4) are slightly higher than those measured at central axial positions (P2, P5, P8 and P11) which are, in turn, higher than those at the downstream positions (P9, P12). For Reynolds number less than 5000, this dependence on axial position could not be clearly ascertained due to the higher scatter in these results. It is difficult to offer an explanation for these features of the flows based on an examination of the available results, other than to say that in the regions where the hot-wire measurements were made, the flows reflect a rather complex interaction of four shear layers, two off the top and bottom surfaces of the plates, and another two on the top and bottom walls of the duct.

As a concluding remark in this section, the author would like to express the hope that the turbulence power spectrums and Strouhal numbers provide by the hot-wire measurements would serve as checks on the predictions of mathematical models and numerical solution methods for unsteady turbulent flows in interrupted-surface geometries, and thus prove useful to researchers who are currently developing such models and methods.

5.2 RESULTS OF THE NUMERICAL INVESTIGATIONS

The results of the numerical investigations are presented in this section. The problems were solved with a FORTRAN 77 computer program based on the finite volume method (FVM) described in chapter 4. All computations were performed on personal computers equipped with Pentium IV processors. The FVM and the computer program were first validated by solving many benchmarking test problems. Two such test problems were the following: (1) steady spatially-periodic fully-developed laminar flow and heat transfer in staggered plate arrays; and (2) unsteady unconfined laminar flow past a square cylinder. The first of these test problems evaluated the overall validity of the code and its ability to solve flow and heat transfer problems in cyclic domains. The second test problem validated the capability of the code to simulate unsteady flows. Finally, the two main problems of interested were tackled: (1) unsteady laminar developing flow in interrupted-plate ducts; (2) unsteady laminar developing flow in staggered-plate arrays.

5.2.1 TEST PROBLEM #1: STEADY SPATIALLY-PERIODIC FULLY-DEVELOPED LAMINAR FLOW AND HEAT TRANSFER IN STAGGERED PLATE ARRAYS

5.2.1.1 PROBLEM OVERVIEW

The objective of this investigation was to validate the numerical method by comparing the friction factors and Colburn factors results with those obtained by Sebben (1996). This problem was first solved by Patankar and Prakash (1981). Sebben (1996) later solved the problem with a modern staggered grid method. Thus, the recent results of Sebben (1996) are used to check the results obtained with the FVM developed in this work. Attention is focused on code benchmarking rather than providing a detailed analysis of the flows in this problem, which is already available in the aforementioned references. The computational domain is shown in figure 5.19 as a dotted area comprising a half-module.

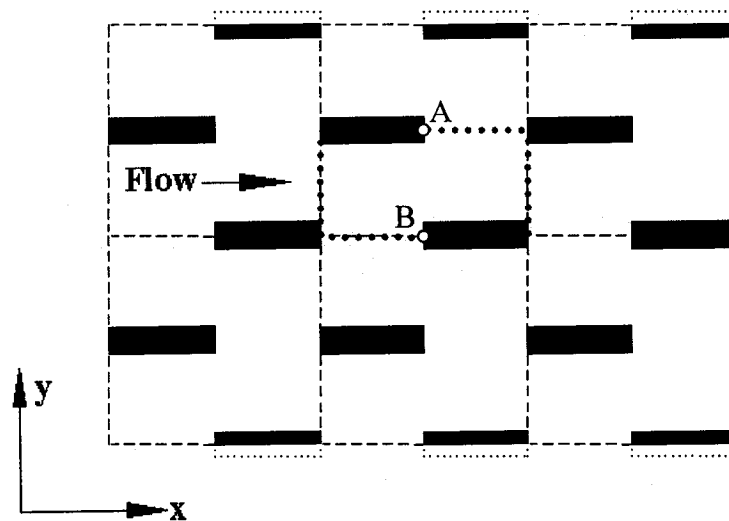


Figure 5.19 Cross-sectional view of a staggered plate array and the computational domain.

The computational domain may be limited to a half-module, since for such spatially-periodic fully-developed steady flows, the flow symmetry can be exploited. The top and bottom boundaries are lines of symmetry, while cyclic conditions are imposed on the left and right boundaries. Special equations for this specific cyclic problem are used and are presented in section 2.2.2. In this problem, a dimensionless overall modular pressure gradient term β^* is imposed, and this drives the flow to a corresponding Reynolds number or mass flow rate. Multiple values of this parameter were investigated, for three different geometrical configurations: $t/H = 0.1, 0.2$ and 0.3 . In all cases, L/H was set equal to 2. The resulting Reynolds numbers varied from approximately 100 to 1200. The Prandtl number was set equal to 0.7.

The boundary conditions for the flow problem are the following: velocities are nil on the plate surfaces; v is set to zero and $\frac{\partial u}{\partial y} = 0$ on the top and bottom symmetry lines; and periodic conditions apply to the velocity components on the left and right boundaries. The boundary conditions for the periodic temperature variable \tilde{T} (derived in section 2.2.2) are similar: $\frac{\partial \tilde{T}}{\partial y} = 0$ along the top and bottom symmetry lines; and periodic conditions prevail on the cyclic domain boundaries. Following the discussions in section 2.2.2, \tilde{T} in the first and second plates is given by the following expressions, respectively:

$$\begin{aligned}\tilde{T}\Big|_{First\ Plate} &= T_w - \Delta T \left(\frac{x}{L} \right) \\ \tilde{T}\Big|_{Second\ Plate} &= T_w + \Delta T - \Delta T \left(\frac{x}{L} \right)\end{aligned}\tag{4.51}$$

The dimensionless parameters involved in this study are defined with respect to the nomenclature used by Patankar and Prakash (1981) and Sebben (1996):

$$\beta^* = \frac{\beta H^3}{\rho(\mu/\rho)^2} \quad (4.52)$$

$$Re = \frac{\rho \bar{U}(4H)}{\mu}; \quad ff = \frac{\beta(4H)}{2\rho \bar{U}^2}; \quad St = \frac{h}{\rho \bar{U} c_p} \quad (4.53)$$

In the previous equations, \bar{U} is the average velocity based on the nominal height of the half-module H , and h is the average heat transfer coefficient over the module. These variables are defined as follows:

$$\bar{U} = \frac{\dot{m}}{\rho H}; \quad h = \frac{Q_{module}}{A_{H.T.} LMTD} \quad (4.54)$$

where \dot{m} is the calculated mass flow rate per unit depth, and Q_{module} is the total rate of heat transfer in the half-module per unit length. These heat transfer quantities are again defined with respect to the work of Patankar and Prakash (1981):

$$\begin{aligned} Q_{module} &= \dot{m} c_p (2\Delta T) \\ A_{H.T.} &= 2L \\ LMTD &= \frac{\Delta T}{\ln \left(1 + \frac{\Delta T}{T_W - T_{B\text{mid-domain}}} \right)} \end{aligned} \quad (4.55)$$

In the definition of $LMTD$ (the log-mean temperature difference), $T_{B\text{mid-domain}}$ is the bulk temperature calculated along the vertical mid-domain line formed by joining points A and B in figure 5.19. The bulk temperature definition used by Patankar and Prakash (1981) is based on the absolute value of velocity and is described by the following expression for constant property flows:

$$T_B = \frac{\int T |u| dy}{\int |u| dy} \quad (4.56)$$

Additionally, with the aforementioned equations, the Stanton number, St , may be expressed as follows:

$$St = \frac{1}{2} \frac{\Delta T}{LMTD} \quad (4.57)$$

Finally, the heat transfer results are expressed in the form of the module Colburn j factor:

$$j = St Pr^{2/3} \quad (4.58)$$

5.2.1.2 COMPUTATION DETAILS

The calculations were performed with three different orthogonal uniform grids: (1) 281X72 CVs; (2) 401X102 CVs; and (3) 481X122 CVs. Identical grids were used by Sebben (1996). In the computations, convergence was considered to be achieved when the two following criteria were met: (1) the absolute values of the normalized residues for every CV and dependent variable are lower than 10^{-8} ; and (2) the relative change in the calculated Reynolds number between two consecutive iterations is lower than 10^{-8} . The first convergence criterion may be expressed as:

$$CRIT_{N.R.}^{\phi} = \left| \frac{a_p^{\phi} - \sum a_{nb}^{\phi} - b^{\phi}}{Reftrn^{\phi}} \right| \leq 10^{-8} \quad \text{for every volume} \quad (4.59)$$

where the reference transport rates (Reftrn) for a single CV is defined as follows:

$$Reftrn^{u,v} = \dot{m} \frac{\Delta y}{H} \bar{U}; \quad Reftrn^p = \dot{m} \frac{\Delta y}{H}; \quad Reftrn^T = \dot{m} \frac{\Delta y}{H} \Delta T \quad (4.60)$$

The second criterion may be expressed as:

$$CRIT_{Re} = \frac{|Re^{\phi} - Re|}{Re} \leq 10^{-8} \quad (4.61)$$

Relaxation coefficients were automatically adapted by the program to prevent divergence during the solution process. In all cases, under-relaxation was applied and the relaxation coefficients, α , varied from 0.5 to 0.75 for all dependent variables.

5.2.1.3 RESULTS

The same problem parameters as those studied by Sebben (1996) were investigated. Three different values of β^* were considered for each geometrical configuration. The resulting Reynolds numbers, friction factors, and Colburn j factors are listed in tables 5.1, 5.2, and 5.3 for the geometrical configurations with t/H values of 0.1, 0.2, and 0.3, respectively. The relative differences (absolute values) between these and the corresponding results of Sebben (1996) are also included.

Table 5.1: Results for test problem #1: Values of Re, ff and j for $t/H = 0.1$

β^*	grid	Results of present study			Relative difference with Sebben(1996)		
		Re	ff	j	Re	ff	j
4687.5	1	1151.36	0.11315	0.02765	0.180%	0.359%	0.713%
4687.5	2	1149.79	0.11346	0.02768	0.144%	0.287%	0.651%
4687.5	3	1149.08	0.11360	0.02770	0.122%	0.244%	0.624%
1953.125	1	534.45	0.21881	0.05527	0.199%	0.396%	0.640%
1953.125	2	533.44	0.21964	0.05544	0.138%	0.275%	0.400%
1953.125	3	533.05	0.21996	0.05532	0.115%	0.230%	0.642%
312.5	1	107.56	0.86442	0.22266	0.147%	0.294%	1.351%
312.5	2	107.33	0.86805	0.22349	0.101%	0.203%	1.007%
312.5	3	107.25	0.86943	0.22321	0.084%	0.167%	1.136%

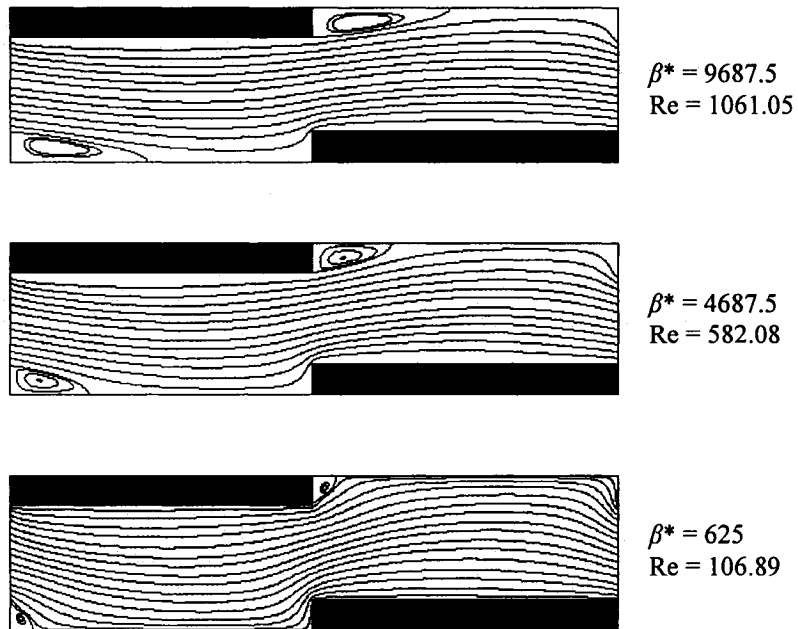
Table 5.2: Results for test problem #1: Values of Re, ff and j for $t/H = 0.2$.

β^*	grid	Results of present study			Relative difference with Sebben(1996)		
		Re	ff	j	Re	ff	j
9687.5	1	1063.80	0.27393	0.03668	0.276%	0.548%	0.692%
9687.5	2	1061.95	0.27489	0.03671	0.227%	0.453%	0.686%
9687.5	3	1061.05	0.27535	0.03685	0.197%	0.392%	0.359%
4687.5	1	584.14	0.43961	0.06143	0.376%	0.747%	0.927%
4687.5	2	582.72	0.44175	0.06155	0.273%	0.544%	0.788%
4687.5	3	582.08	0.44271	0.06161	0.226%	0.451%	0.732%
625	1	107.40	1.73396	0.28017	0.301%	0.601%	1.891%
625	2	107.03	1.74580	0.28130	0.199%	0.397%	1.553%
625	3	106.89	1.75034	0.28176	0.160%	0.320%	1.412%

Table 5.3: Results for test problem #1: Values of Re, ff and j for $t/H = 0.3$.

β^*	grid	Results of present study			Relative difference with Sebben(1996)		
		Re	ff	j	Re	ff	j
32500	1	no convergence obtained			N/A	N/A	N/A
32500	2				N/A	N/A	N/A
32500	3				N/A	N/A	N/A
14218.75	1	585.20	1.32862	0.08456	0.492%	0.978%	1.367%
14218.75	2	583.51	1.33634	0.08513	0.391%	0.777%	0.780%
14218.75	3	582.74	1.33989	0.08416	0.338%	0.673%	1.956%
1562.5	1	105.81	4.46583	0.38261	0.569%	1.129%	2.830%
1562.5	2	105.25	4.51405	0.38520	0.370%	0.737%	2.271%
1562.5	3	105.02	4.53299	0.38486	0.297%	0.591%	2.405%

As expected, the resulting Reynolds number increases with the overall pressure gradient term β^* . The friction factors decrease with increasing Reynolds numbers, a behavior confirmed in numerous experimental investigations. Similarly, the Colburn factors follow the same trend, as expected. Sample streamline plots are presented in figure 5.20 for the flow fields computed with the finest grids for a t/H ratio of 0.2.

**Figure 5.20** Streamline plots for $t/H = 0.2$ and β^* values of 9687.5, 4687.5 and 625.

As shown by the results in tables 5.1, 5.2 and 5.3, the agreement between both set of results is excellent. Convergence was not achieved for β^* values of 32500 and the $t/H = 0.3$ geometry. Sebben (1996) also encountered some convergence problems for this particular case. The maximum discrepancy, a 2.83% relative difference in Colburn factor, occurs at a β^* value of 1562.5 and a t/H ratio of 0.3 for the coarsest grid.

5.2.2 TEST PROBLEM #2: UNSTEADY LAMINAR FLOW PAST A SQUARE CYLINDER

5.2.2.1 PROBLEM OVERVIEW

This test problem involves unsteady unconfined laminar flows across a cylinder of square cross-section. The domain is two-dimensional and flows in the laminar-unsteady regime are studied: Reynolds numbers of 100, 200 and 300, based on the freestream velocity and the square height, were investigated. The results of this study are compared with those of the numerical investigations of Sebben (1996) and Franke et al. (1990), as well as the experimental results of Davis and Moore (1982) and Okajima (1982).

The regular (non-cyclic) computational domain dimensions were chosen to be identical to those used by Sebben (1996) for comparison purposes: the domain width is 12 times the square cylinder height (D), while its length was set to 40 D . The front face of the cylinder was positioned at 4.5 D from the flow entry boundary. This computational domain, its dimensions, and the problem boundary conditions are shown in figure 5.21.

As shown in the figure 5.21, the imposed boundary conditions are: inflow velocity U_0 entering from the left boundary; $\frac{\partial u}{\partial y} = v = 0$ on the top and bottom boundaries; and outflow condition imposed at the right boundary. Velocities were set equal to zero on the square cylinder surfaces. The top and bottom boundary conditions were chosen to approximate freestream conditions. The initial condition corresponds to an impulsive start

of the fluid from rest. In all cases investigated, vortex shedding appeared some time from after initiation, without any need for numerical perturbation of the flow field.

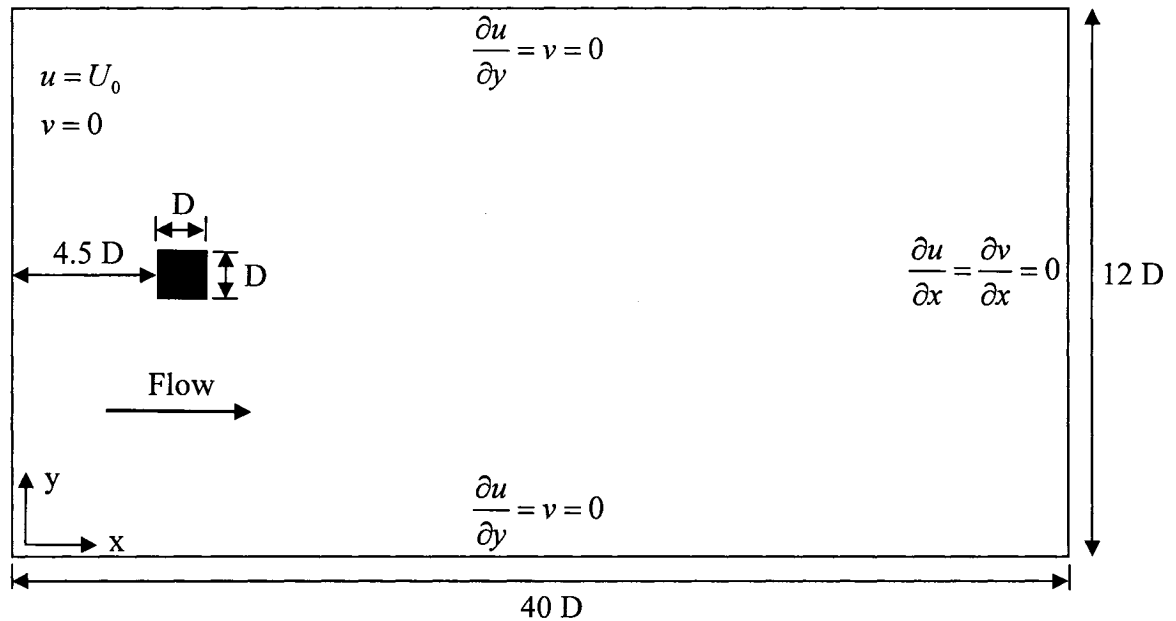


Figure 5.21 Computational domain, dimensions, and boundary conditions for Test Problem # 2.

The dimensionless parameters involved in this study are defined with respect to the nomenclature used by Sebben (1996), in order to facilitate comparisons of the results:

$$Re = \frac{\rho U_0 D}{\mu}; St = \frac{f_v D}{U_0}; C_D = \frac{F_D}{\frac{1}{2} \rho U_0^2 D}; C_L = \frac{F_L}{\frac{1}{2} \rho U_0^2 D} \quad (4.62)$$

The form (or pressure) drag and viscous force components were computed and stored separately, F_D in equation 5.12 includes both these components.

5.2.2.2 COMPUTATION DETAILS

Three different grids were used in the investigations: 201X123, 251X161, and 301X181 CVs. At least a hundred time steps per cycle of vortex shedding were used in the

simulations: preliminary computations showed that the results changed insignificantly with smaller values of the time step.

Convergence was considered to be achieved when the two following criteria were met: (1) the absolute values of the normalized residues for every CV and dependent variable are lower than 10^{-8} ; and (2) the relative change in the calculated Reynolds number between two consecutive inner iterations (in the same time step) is lower than 10^{-8} . The first convergence criterion may be expressed as:

$$CRIT_{N.R.}^{\phi} = \left| \frac{a_p^{\phi} - \sum a_{nb}^{\phi} - b^{\phi}}{Reftrn^{\phi}} \right| \leq 10^{-8} \quad \text{for every volume} \quad (4.63)$$

The reference transport rates (Reftrn) for a single CV is defined as:

$$Reftrn^{u,v} = \dot{m} \frac{\Delta y}{12D} U_0; \quad Reftrn^p = \dot{m} \frac{\Delta y}{12D} \quad (4.64)$$

The second criterion is expressed as follows:

$$CRIT_{Re} = \frac{|Re^0 - Re|}{Re} \leq 10^{-8} \quad (4.65)$$

Again, relaxation coefficients were automatically adapted by the program to prevent divergence during the solution process. However, in unsteady problems with small time steps such as this one, the initial guess variable field is already close to the converged solution for the next time step. Therefore, there is little or no need for under-relaxation. Thus, in all cases, under-relaxation was not required by the program and the relaxation coefficients α were maintained at 1.0 for all dependent variables.

The code monitored and recorded the vertical velocity component (v) at a point located on the domain horizontal centerline and one-D downstream from the cylinder in the axial direction. When periodic oscillations of this monitored velocity were observed, the program started the data recording when the oscillations displayed constant amplitude within $\pm 0.1\%$ between successive cycles. The program then recorded 20 cycles of vortex shedding. If the velocity oscillations were chaotic (notably for $Re = 300$), the data recording was started when the time-averaged result were shown to have reached constant values. Additionally, this monitored velocity was used to compute the vortex-shedding frequencies with the same algorithm as that used for the calculations of turbulence power spectrums in the experimental investigations. However, these power spectrums were smooth and the curve-fitting method (used to process the experimental results) was not required to determine the vortex shedding frequency.

5.2.2.3 RESULTS

First, it must be pointed out that results for this problem are known to be very sensitive to the numerical treatment of the cylinder corners and even slight differences in boundary conditions. On the experimental side, the results are strongly influenced by the alignment and sharpness of the cylinder corners. Therefore, a fair amount of scatter in the results is generally observed in the literature. This detail should be kept in mind when the experimental and the numerical results are reviewed and compared.

The calculated Strouhal numbers and time-mean total drag coefficients (form and shear forces) are first compared to the available numerical data of Sebben (1996) and Franke et al. (1990). These results are listed in table 5.4.

Table 5.4: Results for test problem #2: Values of St and C_D .

Re	Present calculations		Franke et al. (1990)		Sebben (1996)	
	St	C_D	St	C_D	St	C_D
100	0.156	1.612	0.154	1.61	0.156	1.57
200	0.144	1.699	0.157	1.60	0.166	1.66
300	0.140	1.922	0.13	1.83	0.147	1.86

The overall agreement between the present results and those of Franke et al. (1990) and Sebben (1996) is good. At $Re = 200$, the highest percentage relative difference in the Strouhal number values is 15.68% and 9.4% compared to the corresponding results of Sebben (1996) and Franke et al. (1990), respectively. The average differences (absolute values) with reference to the results of both Sebben (1996) and Franke et al. (1990) are 6.29% for Strouhal numbers and 3.1% for the drag coefficients.

The results were also compared with the experimental Strouhal number data of Okajima (1982) and Davis and Moore (1982). Both sets are shown in figure 5.22 along with results of the numerical investigations of Sebben (1996) and Franke et al. (1990).

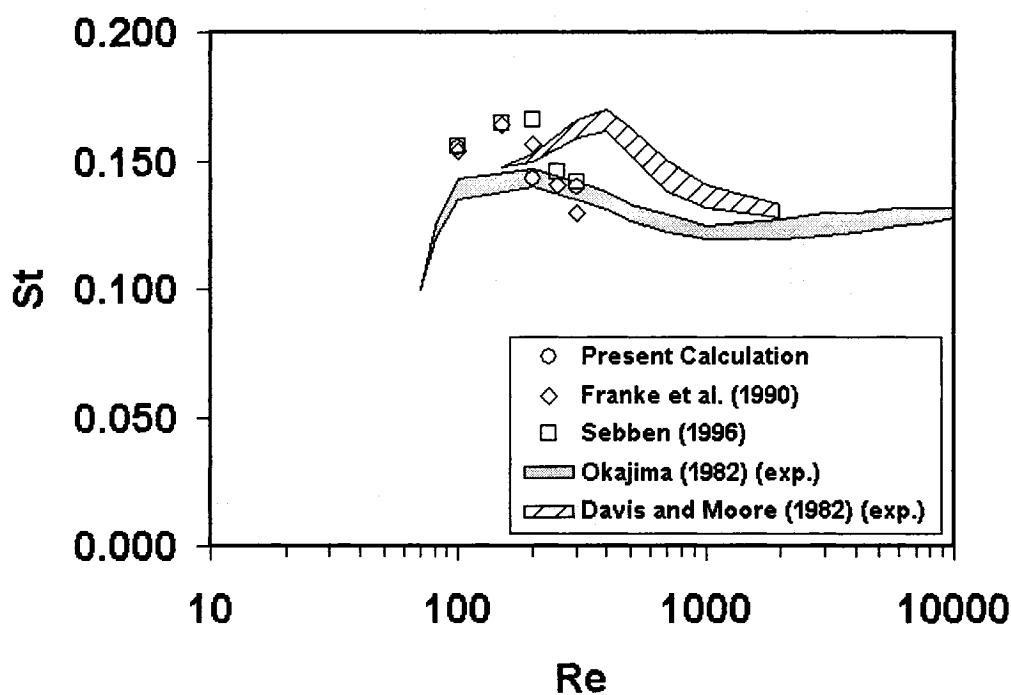


Figure 5.22 Strouhal number as function of Reynolds number.

The main striking feature observed in figure 5.22 is the difference between the two sets of experimental results of Okajima (1982) and Davis and Moore (1982). This appreciable difference of Strouhal numbers supports the earlier statement suggesting a strong sensitivity of such flows to slight variations in test parameters. Nevertheless, the results of the present calculation show very good agreement with the data of Okajima (1982), especially at Reynolds number values of 200 and 300, where they lie within in the

experimental scatter. Other numerical investigations of Sebben (1996) and Franke et al. (1990) show inferior agreement with the experimental results of Okajima (1982). None of the numerical calculations replicate the overall trend of the experimental data of Davis and Moore (1982), and the present computations show only average agreement with their experimental results.

5.2.3 NUMERICAL INVESTIGATION #1: UNSTEADY LAMINAR DEVELOPING FLOW IN INTERRUPTED-PLATE DUCTS

5.2.3.1 PROBLEM OVERVIEW

This problem involves unsteady two-dimensional developing laminar flows in interrupted-plate ducts akin to the one shown in figure 1.3. The objective of this study is to solve flows from the duct inlet plane downstream to the spatially-periodic fully-developed region. Modular time-mean friction factors are provided along with vortex shedding Strouhal numbers. The results are also compared with those of Sebben (1996), who investigated the unsteady spatially-periodic fully-developed flow regime by including multiple modules in an axially-cyclic domain. The computational domain is similar to the one shown in figure 4.2, except that the number of geometric modules included in the calculation domain in the axial direction was varied from 6 to 20.

The calculations are divided into two parts: (1) the effects of the number of modules included in the computational domain are investigated for a single geometrical configuration with $t/H = 0.32$; and (2) different Reynolds number values are investigated for two geometrical configurations with $t/H = 0.20$ and 0.32 . In the first part of this numerical investigation, the Reynolds number, based on the duct height ($2H$) and the time-mean average axial velocity \bar{U} , was kept at 382.65 and the number of modules was set to 6, 8, 10, and 20. The second set of calculations was performed with 10 modules in the axial direction and the Reynolds number was instead varied: Re values of 300 and 400 were explored for $t/H = 0.32$; and Re values of 239.04 and 484.58 were investigated

for $t/H = 0.20$. These Reynolds number values were specifically chosen to allow comparison with the results of Sebben (1996). The following geometrical parameters were kept constant: $L/H = 2$ and $s/H = 2$.

The boundary conditions for this problem are the following: a uniform inlet velocity profile at the left boundary; zero velocity ($u = v = 0$) on the top and bottom walls as well as on the plate surfaces; and outflow conditions ($\frac{\partial u}{\partial x} = \frac{\partial v}{\partial x} = 0$) at the right boundary. The initial condition is equivalent to fluid at rest and an impulsive start was applied at the first time step. Flow unsteadiness appeared spontaneously without any need for numerical perturbations of the flow field.

In order to facilitate the comparison of results, the dimensionless parameters involved in this study are defined with respect to the nomenclature used by Sebben (1996). They were listed and discussed in section 2.4.2.1. They are listed here again for convenience:

$$Re = \frac{\rho \bar{U} (2H)}{\mu}; \bar{U} = \frac{\dot{m}}{2H\rho}; ff = \frac{(2H)\langle\beta\rangle_{module}}{\frac{1}{2}\rho\bar{U}^2}; St = \frac{f_v(2t)}{\bar{U}} \quad (4.66)$$

The Strouhal number was computed by selecting the vortex shedding frequency observed in the power spectrums: the vertical velocity component (v), located along the duct centerline and at a quarter-plate length ($L/4$) behind the last plate, was monitored and stored; and then the power spectrums were computed with the same routine that was used in the experimental investigations. It should be noted that these power spectrums were smooth; thus the curve-fitting method (used earlier to process the experimental results) was not required to determine the vortex shedding frequency in this case.

5.2.3.2 COMPUTATION DETAILS

The objective of the current investigation is to complement and extend the past efforts of Sebben (1996) by simulating developing flows from the duct inlet plane downstream to the spatially-periodic fully-developed region. Sebben (1996) used a staggered grid method and an axially-cyclic domain comprising 1 to 6 modules. She performed

numerous grid and time step independence studies. Precious computing time was saved by assuming that the grids and time steps used by Sebben (1996) were adequate for the present numerical method. This assumption is justified by the similarities of both numerical methods and investigated parameters. Thus, the computations were performed with uniform grids ($\Delta x = \Delta y$). Such grids are known to ensure adequate simulation of oscillating recirculation zones and shear-layers. The grid was composed of 100X50 CVs per module. A flow exit section, consisting of a plain duct of same height $2H$, was added after the last plate module in order to prevent flow reversal at the exit boundary of the calculation domain. This exit section accounted for 300X50 CVs and its length was set equal to $7\Lambda=7(L+s)$: the x extent of this section was divided into three adjacent segments of lengths Λ , 2Λ , and 4Λ , and 100X50 CVs were distributed uniformly in each of these segments, making the exit section grid non-uniform. Therefore, a 10 module domain is composed of 1000X50 CV in the plate section, and an additional 300X50 CVs in the exit section, and would measure 17Λ long. The simulations were performed with the same time steps as those used by Sebben (1996).

Convergence of at each time step was considered to be achieved when the two following criteria were met: (1) the absolute values of normalized residues are lower than 10^{-6} for every CV and dependent variable; (2) the relative change in the calculated Reynolds number between two consecutive inner iterations (in the same time step) is lower than 10^{-8} . The first convergence criterion is expressed as follows:

$$CRIT_{N.R.}^{\phi} = \left| \frac{a_p^{\phi} - \sum a_{nb}^{\phi} - b^{\phi}}{Reftrn^{\phi}} \right| \leq 10^{-6} \quad \text{for every volume} \quad (4.67)$$

The reference transport rates (Reftrn) for a single volume were defined as follows:

$$Reftrn^{u,v} = \dot{m} \frac{\Delta y}{2H} \bar{U}; \quad Reftrn^p = \dot{m} \frac{\Delta y}{2H} \quad (4.68)$$

The second criterion is expressed as follows:

$$CRIT_{Re} = \frac{|Re^0 - Re|}{Re} \leq 10^{-8} \quad (4.69)$$

Under-relaxation was not invoked by the program and the relaxation coefficients, α , were maintained at 1.0 for all dependent variables. The results were recorded when the oscillation of the aforementioned monitored velocity displayed a constant amplitude within $\pm 0.1\%$ between consecutive cycles. The program then recorded data for at least 10 vortex shedding cycles.

5.2.3.3 RESULTS

In the first part of the investigation, the Reynolds number was kept constant and the number of modules in the computational domain was varied. Time-mean module friction factors (ff) were computed for $Re = 382.65$ and $t/H = 0.32$. Results were obtained for domains with 6, 8, 10 and 20 modules and are listed in table 5.5. It must be noted that the last module friction factor is not relevant since it is affected by the flow exit section.

Table 5.5: Time-mean module friction factors for $Re = 382.65$ and $t/H = 0.32$.

Module	ff			
	6 modules	8 modules	10 modules	20 modules
1	1.4564	1.4564	1.4564	1.4564
2	1.1116	1.1114	1.1114	1.1115
3	1.1593	1.1592	1.1590	1.1593
4	1.1584	1.1583	1.1580	1.1584
5	1.1538	1.1537	1.1533	1.1538
6		<u>1.1530</u>	<u>1.1525</u>	<u>1.1531</u>
7		<u>1.1531</u>	<u>1.1526</u>	<u>1.1531</u>
8			<u>1.1527</u>	<u>1.1532</u>
9			<u>1.1529</u>	<u>1.1532</u>
10				<u>1.1532</u>
11				<u>1.1532</u>
12				<u>1.1532</u>
13				<u>1.1532</u>
14				<u>1.1532</u>
15				<u>1.1532</u>
16				<u>1.1532</u>
17				<u>1.1532</u>
18				<u>1.1532</u>
19				<u>1.1533</u>

The overall behavior of the modular friction factors is the same for all four domains. The values of ff at the duct entry are high and they asymptote to a constant value as the spatially-periodic fully-developed regime starts to get established. The underlined friction factors denote modules where the flow is essentially fully-developed. The 6-module domain did not include enough modules to display the existence of the spatially-periodic fully-developed regime with confidence. On the other hand, this regime was shown to prevail in the 8-, 10-, and 20-module calculation domains, where essentially equal modular friction factors are observable after some distance from the inlet. For these three calculation domains, the fully-developed friction factors are essentially identical, the relative difference between results being lower than 0.1%. For this Reynolds number value (382.65), the fully-developed regime is shown to prevail after the fifth module. Thus, it was judged that the 10-module domain was adequate for future simulations. Additionally, the results obtained with 10 modules are nearly identical to those provided by the computationally expensive 20-module domain. Computed Strouhal numbers are identical for all four calculation domains and are equal to 0.3336.

Sebben (1996) performed calculations for the same geometrical configuration and Reynolds number. However, the computational domain was limited to a single module in the fully-developed region with the use of a cyclic domain similar to the one shown in test case 1. The time-mean modular friction factor was equal to 1.1403, a value very close the fully-developed values obtained in the present study. This very good agreement shows that the cyclic domain simplification used by Sebben (1996) yields similar results to those obtained by simulating a complete duct, and it also confirmed at the same time the validity of the numerical method used in this work. Unfortunately, no Strouhal number value was provided by Sebben (1996) for this case.

The second part of this numerical study consisted of investigating different geometrical configurations and multiple Reynolds number values with the adopted 10-module domain. The time-mean module friction factors are listed in table 5.6 for $t/H = 0.32$ and in table 5.7 for $t/H = 0.20$.

Table 5.6: Time-mean module friction factors for $t/H = 0.32$.

Module	ff	
	Re = 300	Re = 400
1	1.6101	1.4337
2	1.1888	1.1017
3	1.2099	1.1554
4	1.2083	1.1546
5	1.2058	1.1493
6	<u>1.2053</u>	1.1486
7	<u>1.2052</u>	<u>1.1487</u>
8	<u>1.2052</u>	<u>1.1488</u>
9	<u>1.2051</u>	<u>1.1489</u>

Table 5.7: Time-mean module friction factors for $t/H = 0.20$.

Module	ff	
	Re = 239.04	Re = 484.58
1	1.1292	0.7667
2	0.6839	0.4561
3	0.6698	0.4736
4	<u>0.6690</u>	0.4906
5	<u>0.6689</u>	0.4948
6	<u>0.6689</u>	0.4940
7	<u>0.6689</u>	0.4925
8	<u>0.6689</u>	<u>0.4920</u>
9	<u>0.6689</u>	<u>0.4919</u>

Once more, the spatially-periodic fully-developed regime is shown to prevail after some distance downstream from the duct inlet. Friction factors showing the existence of this regime are again underlined. As expected, these results also reveal that the development length increases with the Reynolds number for both geometries. In both cases, the fully-developed friction factor values decrease with Re. It must be noted that for $Re = 239.04$ and $t/H = 0.20$, the flow remained completely steady. An instantaneous streamline plot is presented in figure 5.23 for $Re = 300$ and $t/H = 0.32$.

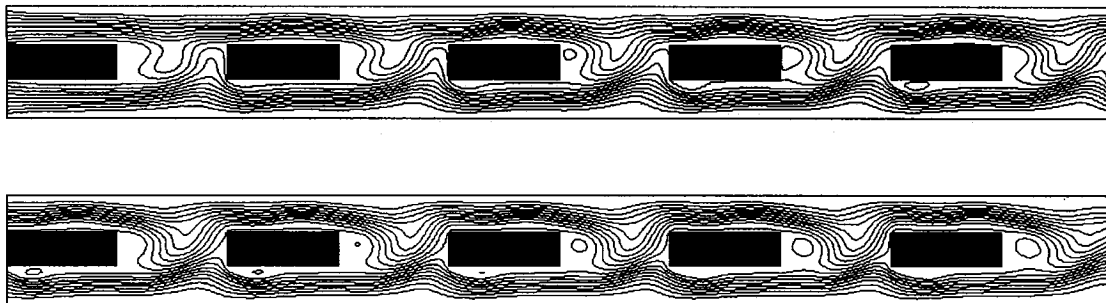


Figure 5.23 Instantaneous streamline plot for $Re = 300$ and $t/H = 0.32$.

In the figure 5.23, the 10-module duct is split into two parts, and the exit section is omitted: the flow enters from the top-left boundary and exits from the bottom right boundary; flow exiting the upper right corner enters the bottom left one. This plot reveals some flow features such as vortex shedding from the trailing edge of the plates and recirculation bubbles rolling down the plate horizontal surfaces. The figure also displays the vortex shedding phase variation between different modules. It can be seen that a complete vortex shedding cycle is not observed in the whole domain. Therefore, more modules should be included in the domain to determine if the flow would then display an unsteady cyclic behavior over a certain number of modules in the fully-developed region.

Next, the fully-developed module friction factors were compared with the results of Sebben (1996). For the first geometry ($t/H = 0.32$), Sebben (1996) performed multiple calculations for each Re value by including from one to six modules in the cyclic domain. The full range of friction factors is listed in table 5.8 and compared to the fully-developed values of the present investigation for both Re values. For the second geometrical configuration ($t/H = 0.20$), the results are compared in table 5.9 with those obtained by Sebben (1996) with a six module cyclic domain.

Table 5.8: Fully-developed module friction factors ($t/H = 0.32$) compared with results of Sebben (1996).

Re	Fully-developed values of ff		
	Current calc.	Sebben (1996)	
		min	max
300	1.2051	1.1916	1.2222
400	1.1489	1.1034	1.1720

Table 5.9: Fully-developed module friction factors ($t/H = 0.20$) compared with results of Sebben (1996).

Re	Fully-developed values of ff	
	Current calc.	Sebben (1996)
239.04	0.6689	0.7000
484.58	0.4919	0.4770

Again, the agreement between the results of both investigations is good. The fully-developed module friction factor values of the current calculation fall in the range of the results obtained by Sebben (1996) for $t/H = 0.32$. Good agreement is also observed for the second geometry ($t/H = 0.20$): for a Re value of 239.04 and $t/H = 0.20$, the agreement remained good even if steady flow was obtained with the current method whereas unsteadiness was present in the cyclic domain of Sebben (1996). In general, the comparison of results suggests that the cyclic model used by Sebben (1996) provides very similar fully-developed friction factors without the need to simulate a complete duct.

The computed Strouhal number values are listed in tables 5.10 for $t/H = 0.32$ and $t/H = 0.20$, along with the results of Sebben (1996).

Table 5.10: Strouhal numbers compared with results of Sebben (1996).

t/H	Re	St	
		Current calc.	Sebben (1996)
0.32	300	0.3280	0.332 - 0.375
	400	0.3344	0.333 - 0.409
0.2	239.04	N/A	0.215
	484.58	0.2337	0.212

In table 5.10, no Strouhal number value for $t/H = 0.2$ and $Re = 484.58$ is listed, since steady flow prevailed in the current calculations. As mentioned earlier, Sebben (1996) performed multiple calculations with 6 different domains for $t/H = 0.32$. A range of Strouhal numbers is thus listed for this geometry. At first glance, the agreement between both set of results looks very good for $t/H = 0.32$. However, the range of results provided by Sebben (1996) is quite wide, the largest difference between two Strouhal number values being as large as 22.8% for $Re = 400$. Thus, it is difficult to assess with precision the agreement between Strouhal numbers for this geometry.

For the second geometry, $t/H = 0.20$, different flow regimes were obtained for $Re = 239.04$. The flow remained steady in the present calculations while unsteadiness was present in the calculations of Sebben (1996). For $Re = 484.58$, the agreement between Strouhal number values is average, the difference between corresponding results being 10.2%.

5.2.4 NUMERICAL INVESTIGATION #2: UNSTEADY LAMINAR DEVELOPING FLOW AND HEAT TRANSFER IN STAGGERED-PLATE ARRAYS

5.2.4.1 PROBLEM OVERVIEW

This problem involves unsteady two-dimensional developing laminar flows and heat transfer in staggered-plate arrays. The Reynolds number, based on the Kays and London (1984) definition, was varied from 100 to 600, and the Prandtl number was set equal to 0.7 (air). The calculation domain, shown in figure 4.1, is portrayed again in figure 5.24 for convenience. The calculations were performed with multiple domains comprising: (1) 6 modules in the axial direction and 1 module in the lateral direction; (2) 6 modules in the axial direction and 2 modules in the lateral direction; (3) 10 modules in the axial direction and 1 module in the lateral direction. The laminar steady and time-periodic unsteady flow regimes are investigated. Calculations were performed for a single geometry with the

following geometrical parameters: $L/H = 2$ and $t/H = 0.25$. The L/H ratio is representative of actual plate-fin heat exchanger cores. However, the chosen plate thickness ratio t/H is roughly twice as large as common values. This value was intentionally selected to accentuate vortex shedding and shorten the flow developing length. Time-mean module friction factors, time-mean module Colburn factors, and vortex shedding Strouhal numbers were obtained.

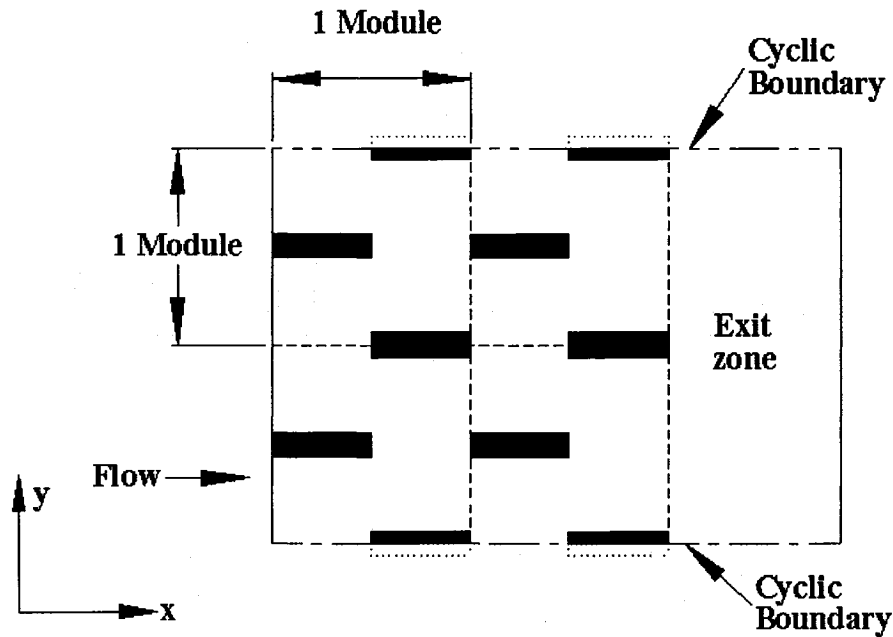


Figure 5.24 Cross-sectional view of staggered-plate array and computational domain.

The flow problem boundary conditions are the following: uniform velocity \bar{U}_{c-min} entering from the left boundary; outflow conditions at the right boundary ($\frac{\partial u}{\partial x} = \frac{\partial v}{\partial x} = 0$); and cyclic conditions imposed on the top and bottom boundaries. Velocities are forced to zero on the plate surfaces. The thermal conditions were fixed as follows: entering flow is at a constant temperature; outflow conditions at the right boundary ($\frac{\partial T}{\partial x} = 0$); and cyclic conditions at the horizontal boundaries. The plate temperature was set to a constant value T_w , different from the inlet fluid temperature, thus the fluid exchanges heat with the plates as it travels down the array.

The dimensionless parameters involved in this study are listed and discussed in detail in section 2.4.2.2. The key parameters are listed again for convenience:

$$Re = \frac{\rho \bar{U}_{c-smin} D_h}{\mu}; \quad ff = \frac{D_h \langle \beta \rangle_{module}}{\frac{1}{2} \rho \bar{U}_{c-smin}^2}; \quad j = \frac{\langle \bar{h} \rangle_{module}}{\rho c_p \bar{U}_{c-smin}} Pr^{2/3}; \quad St = \frac{f_v (2t)}{\bar{U}_{c-smin}} \quad (4.70)$$

The Strouhal number is computed with the vortex shedding frequency observed in the power spectrums. A vertical velocity component (v), located a quarter-plate length ($L/4$) behind the top aft plate of the second-last module and aligned with this plate centerline, was monitored. The power spectrums were calculated with the same procedures as those used in the previous problems.

5.2.4.2 COMPUTATION DETAILS

Grid and time-step independence studies were conducted prior to the main calculations. The time-step independence investigation was carried out first. These studies were performed with a Reynolds number of 1000, a value substantially higher than the maximum value of 600 investigated in the main calculations. If time-step independence is ensured for $Re = 1000$, it would also apply for the lower Re values, as the time period of the vortex shedding phenomenon reduces as Re is lowered. The time-step independence studies were performed with a 6X1 module domain. Each module was discretized into 80X40 CVs forming a uniform grid. The results are listed in table 5.11. The smallest time step investigated, noted here as Δt_{min} , serves as the reference value. Again, the last module data is not relevant since it is affected by the flow exit section and thus is not taken into account.

Table 5.11: Time-step independence study: values of ff and j factors for Re =1000.

Time step	ff					j				
	1	2	3	4	5	1	2	3	4	5
Δt_{\min}	0.5212	0.5411	0.5076	0.5103	0.4897	0.0252	0.0248	0.0255	0.0259	0.0255
$2\Delta t_{\min}$	0.4998	0.5451	0.5074	0.5169	0.4996	0.0252	0.0246	0.0253	0.0259	0.0257
$5\Delta t_{\min}$	0.4859	0.5528	0.5230	0.5326	0.4895	0.0252	0.0244	0.0253	0.0261	0.0260
$10\Delta t_{\min}$	0.4736	0.5489	0.5817	0.5281	0.4424	0.0251	0.0244	0.0247	0.0260	0.0256

The results became essentially independent of time-step when it was less than or equal to $2\Delta t_{\min}$. For this case, the largest discrepancy with the smallest time step Δt_{\min} calculations is a 4.11% relative difference between the first module friction factors. The remaining differences between the other friction and Colburn factors are less than 2.0%. The calculations performed with a $5\Delta t_{\min}$ time step yielded less satisfactory results with relative differences as high as 6.76% in the first module friction factor. The $10\Delta t_{\min}$ calculations are obviously inadequate with discrepancies as high as 14.62%. Thus, the main calculations were performed with time steps equal to or less than $2\Delta t_{\min}$. Typically, more than 300 time steps per vortex shedding cycle were used.

Spatial grid independence studies were also performed at a Reynolds number of 1000 with a time step value of $2\Delta t_{\min}$ and a 6X1 module domain. Again, a high Re value was chosen as an added precaution. The boundary layers become generally thinner with increasing Reynolds number. Therefore, the grids must be refined with increasing Re values and it is preferable to assess grid independence for such stringent conditions. Calculations were performed for four different uniform grids, for which each plate module is composed of: (1) 64X32 CVs; (2) 80X40 CVs; (3) 96X48 CVs; and (4) 112X56 Cvs. The results of this investigation are given in table 5.12.

Table 5.12: Grid independence study: values of ff and j factors for Re =1000.

grid	ff					j				
	1	2	3	4	5	1	2	3	4	5
112X56	0.5003	0.5445	0.5623	0.5098	0.4884	32.0269	33.2816	33.8692	34.1893	33.9481
96X48	0.5001	0.5402	0.5650	0.5291	0.4881	32.0254	32.6284	32.7817	34.5636	33.9284
80X40	0.5001	0.5448	0.5081	0.5158	0.4906	31.9996	31.2049	32.1369	32.8136	32.7463
64X32	0.4966	0.4900	0.3626	0.6241	0.5535	31.2942	31.3598	28.2145	30.8144	33.6573

Calculations performed with the finest grid (112X56 CVs per module) required substantial computing time, thereby preventing the investigation of finer grids. Fortunately, these results were found to be relatively grid independent for the second-finest grid (96X48): the largest discrepancy between the results obtained with the reference 112X56 grid and the 96X48 grid is 3.8% for the fourth module friction factor. For the friction and Colburn factors, the average of differences between corresponding results obtained with these grids is 1.14%. Therefore, the 96X48 grid was chosen for the subsequent calculations. The 80X40 and 64X32 grids were discarded. Finally, the 64X32 grid is inadequate. It is also assumed that the time-step independence studies performed with the 80X40 grid also apply for the chosen 96X48 grid.

Again, a flow exit section was required to prevent flow reversal at the exit boundary. This exit section accounted for 288X48 CVs and its length was set equal to $7\Lambda=7(2L)$: the x extent of this section was divided into three adjacent segments of lengths Λ , 2Λ , and 4Λ , and 96 X 48 CVs were distributed uniformly in each of these segments, making the exit section grid non-uniform. Thus, a 6 module domain is composed of 576X48 CVs in the array section, an additional 288X48 CVs in the exit section, and would measure 13Λ in total length. The Crank-Nicolson scheme was employed for the time integrations.

Convergence at each time step was considered to be achieved when the three following criteria were met: (1) the absolute values of the normalized residues are lower than 10^{-6} for every CV and dependent variable; (2) the relative change in the calculated Reynolds number between two consecutive inner iterations (in the same time step) is lower than 10^{-6} ; and (3) the difference between the target Reynolds number and the calculated value at the domain vertical centerline is less than 10^{-6} . The first convergence criterion is expressed as:

$$CRIT_{N.R.}^{\phi} = \left| \frac{a_p^{\phi} - \sum a_{nb}^{\phi} - b^{\phi}}{Refrn^{\phi}} \right| \leq 10^{-6} \quad \text{for every volume} \quad (4.71)$$

The reference transport rates (Reftrn) for a single CV are defined as follows:

$$Reftrn^{u,v} = \dot{m} \frac{\Delta y}{2H \cdot n} \bar{U}_{c-smin}; Reftrn^p = \dot{m} \frac{\Delta y}{2H \cdot n}; Reftrn^T = \dot{m} \frac{\Delta y}{2H \cdot n} (T_w - T_m) \quad (4.72)$$

where n is the number of modules in the transverse (y) direction.

The second criterion is expressed as follows:

$$CRIT_{Re} = \frac{|Re^o - Re|}{Re} \leq 10^{-6} \quad (4.73)$$

The third criterion is defined as:

$$CRIT_{Re} = \frac{|Re_{calc.} - Re_{target}|}{Re_{target}} \leq 10^{-6} \quad (4.74)$$

Once more, under-relaxation was not invoked by the program and the relaxation coefficients, α , were kept equal to 1.0 for all dependent variables.

Results were recorded when the oscillation of the aforementioned monitored velocity displayed a constant amplitude, to within $\pm 0.1\%$, between successive cycles. The program then recorded data for at least 20 vortex shedding cycles.

5.2.4.3 RESULTS

The first set of calculations were performed for a single geometry ($t/H = 0.25$ and $L = 2H$) and the Reynolds number was varied from 100 to 600. Time-mean module friction factors and Colburn factors were obtained as well as vortex shedding Strouhal numbers. This first set of calculations was performed with 6X1 module domains and also 6X2 module domains to investigate the effects of an added second module row in the

transverse direction. For Re values equal to or lesser than 300, the flows remained steady. Time-periodic unsteadiness was observed for Re values of 400, 500 and 600. The results are presented in table 5.13. As expected, for steady flows, calculations performed with a 6X2 domain yielded identical results to those obtained with a 6X1 domain. Therefore, results are only presented for the 6X1 module domain for steady flow cases. Multiple solutions were discovered with the 6X2 module domain for unsteady flows. The first stable solution (sol. 1) is obtained by introducing the 6X1 solution twice into the 6X2 domain. The second stable solution (sol. 2) is attained by running the calculations from scratch. Once more, last module data is not relevant since it is altered by the flow exit section and is omitted in table 5.13.

Table 5.13: Values of ff, j factors, and Strouhal numbers
for $t/H = 0.25$ and $L = 2H$.

Re	Domain	ff					j factor					St
		1	2	3	4	5	1	2	3	4	5	
600	6X1	0.5240	0.4459	0.4487	0.4749	0.4508	0.0327	0.0312	0.0305	0.0314	0.0306	0.2172
600	6X2 sol. 1	0.5241	0.4461	0.4486	0.4747	0.4510	0.0327	0.0312	0.0306	0.0314	0.0306	0.2173
600	6X2 sol. 2	0.5240	0.4458	0.4487	0.4746	0.4511	0.0327	0.0312	0.0305	0.0314	0.0306	0.2172
500	6X1	0.5404	0.4598	0.4495	0.4616	0.4582	0.0359	0.0340	0.0340	0.0342	0.0343	0.2209
500	6X2 sol. 1	0.5404	0.4598	0.4495	0.4616	0.4583	0.0359	0.0340	0.0340	0.0342	0.0343	0.2209
500	6X2 sol. 2	0.5388	0.4592	0.4499	0.4612	0.4582	0.0359	0.0339	0.0340	0.0342	0.0343	0.2210
400	6X1	0.5299	0.4706	0.4606	0.4600	0.4604	0.0398	0.0374	0.0383	0.0382	0.0383	0.2216
400	6X2 sol. 1	0.5299	0.4706	0.4606	0.4600	0.4604	0.0398	0.0374	0.0383	0.0382	0.0383	0.2216
400	6X2 sol. 2	0.4702	0.3343	0.3358	0.3391	0.3985	0.0378	0.0308	0.0313	0.0315	0.0336	N/A
300	6X1	0.5128	0.4007	0.4006	0.4006	0.4006	0.0464	0.0386	0.0388	0.0388	0.0388	steady
250	6X1	0.5757	0.4596	0.4593	0.4593	0.4593	0.0533	0.0454	0.0456	0.0456	0.0456	steady
200	6X1	0.6666	0.5435	0.5432	0.5432	0.5432	0.0632	0.0554	0.0555	0.0555	0.0555	steady
100	6X1	1.0797	0.9205	0.9202	0.9202	0.9202	0.1083	0.1014	0.1014	0.1014	0.1014	steady

The overall behavior of the module friction factor and Colburn factor is similar for all calculations. The module ff and j factors are initially high when flow enters the array and become essentially constant as flow travels downstream. The high entry values of ff are explained by the high pressure drops induced by the developing velocity profile. Further downstream, time-mean module friction factors approach constant values as the flow progresses towards the spatially-periodic fully-developed regime. For similar reasons,

entry Colburn factors are high adjacent to the inlet plane, and they head towards constant values as the thermal fully-developed condition is approached.

As expected, the first solution (sol. 1) obtained with 6X2 domains yields results that are identical to those obtained with the 6X1 domain. In this solution, the instantaneous velocity and temperature fields in each of the two horizontal module rows are identical to one another. An instantaneous streamline plot is shown in figure 5.25: flow features such as vortex shedding from the plate trailing edges and the presence of recirculation bubbles are noticeable.

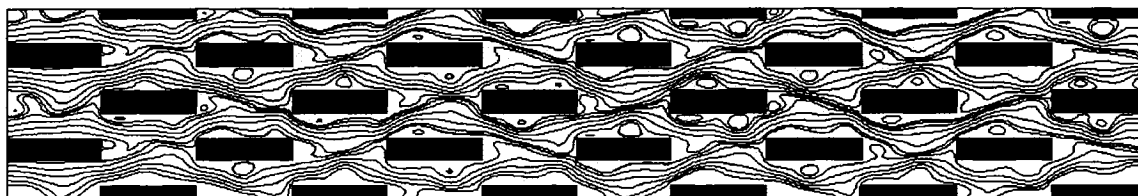


Figure 5.25 Instantaneous streamline plot for $Re = 600$ and 6X2 module domain (sol. 1).

The second solution (sol. 2) is distinct from the first with regard to the corresponding instantaneous velocity and temperature fields, but yields similar time-averaged results for Re values of 500 and 600. In such cases, the vortices shed from the top and the bottom module plates at the same axial position are slightly out of phase. The second solution (sol. 2) for a Re value of 400 is different from the first (sol. 1) and also the 6X1 domain solution: for solution 2, vortex shedding occurs in the last two modules whereas it is present in every module for solution 1 and also the 6X1 domain solution. Furthermore, solution 2 did not approach the spatially-periodic fully-developed regime and, thus, no Strouhal number was obtained for this case (indicated by N/A in table 5.13).

The vortex shedding Strouhal numbers are quite close to each other for the three Reynolds numbers at which flow unsteadiness is present. Adding an additional module row in the lateral direction did not affect the values of St . The multiple solutions obtained with 6X2 domains provided essentially identical Strouhal number values.

Therefore, it can be stated that adding a second module row generally induced no discernable effects on the computed results. An exception is observed for a Re value of 400, for which the flow is different for the 6X1 and 6X2 domains (sol. 2).

With the aforementioned calculation domains, fully-developed values of ff and j factor were obtained for Reynolds number up to 400; however, for Reynolds numbers of 500 and 600, these factors do not quite reach their fully-developed values. Additional calculations were performed with a 10X1 module domain to check if ff and j would then reach their fully-developed values: the results of these additional investigations for Re values of 400 and 500 are listed in table 5.14, with the fully-developed values underlined; no fully-developed values were obtained for Re = 600. The Strouhal numbers calculated with the 10X1 module domain were essentially identical to those obtained with the previous domains.

Table 5.14: Values of ff, j factors, and Strouhal numbers for $t/H = 0.25$ and $L = 2H$.

module	Re = 400		Re = 500	
	ff	j	ff	j
1	0.5299	0.0398	0.5403	0.0359
2	0.4706	0.0374	0.4597	0.0340
3	0.4606	0.0383	0.4494	0.0340
4	0.4600	0.0382	0.4615	0.0342
5	<u>0.4604</u>	<u>0.0383</u>	0.4582	0.0343
6	<u>0.4603</u>	<u>0.0383</u>	0.4604	0.0342
7	<u>0.4603</u>	<u>0.0383</u>	0.4598	0.0342
8	<u>0.4603</u>	<u>0.0383</u>	<u>0.4601</u>	<u>0.0341</u>
9	<u>0.4604</u>	<u>0.0383</u>	<u>0.4601</u>	<u>0.0341</u>

It is interesting to observe the variations of the fully-developed values of ff and j factor with Reynolds number, as plotted in figure 5.26.

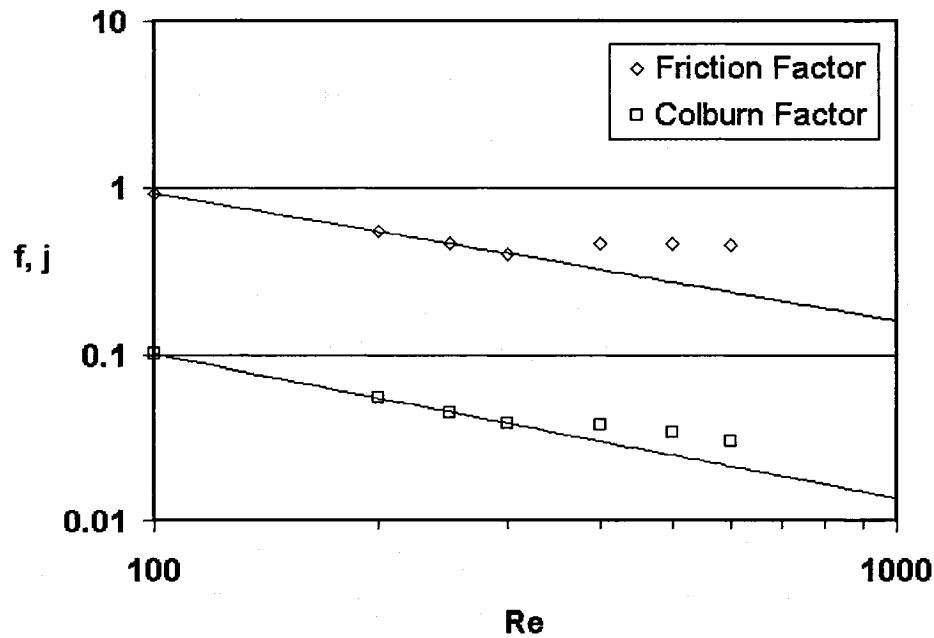


Figure 5.26 Fully-developed ff and j factors as functions of Re ($t/H = 0.25$ and $L = 2H$).

As can be seen in figure 5.26, on a log-log plot, the friction and Colburn factors vary linearly with Re in the steady flow regime: thus it can be deduced that the variations of both ff and j factor with Reynolds number in this flow regime can be represented by a power-law function: this behavior of ff and j factor has also been observed in numerous experiments on actual cores [Kays and London (1984)]. At higher values of Re , flow unsteadiness appears and the values of ff and j factor depart from this power-law function, the enhanced mixing due to vortex shedding is accompanied by an increase in pressure loss, consequently augmenting the values of ff ; and the corresponding heat transfer is also enhanced, thereby increasing the Colburn factor above the implied steady-state values. This increase in heat transfer and pressure loss due to unsteady effects was also observed by Kays and London (1984). Unfortunately, no direct quantitative comparisons are possible with experimental data for the following reasons: (1) the calculations were performed with an idealized two-dimensional geometry whereas flow three-dimensionality is present in actual heat exchanger cores; (2) the investigated plate thickness is about twice the actual values encountered in the tested heat exchanger cores; and (3) the majority of experiments were done with complete heat exchangers, thus fully-developed values of module ff and j factor cannot be extracted from the data provided.

This is the first investigation, to the author's knowledge, in which unsteady developing flow and heat transfer in such geometries have been simulated from the inlet plane to the spatially-periodic fully-developed region. Also, these investigations have quantified, for the first time, the effects of adding of a second module row to the domain in the transverse direction.

CHAPTER 6 – CONCLUSION

This final chapter contains: (1) a brief review of this thesis and its main contributions, and (2) a few suggestions regarding possible extensions of this work. The portions of the text pertaining to the contributions of the thesis are highlighted by presenting them in *italics*.

6.1 REVIEW OF THE THESIS AND ITS MAIN CONTRIBUTIONS

In the first chapter, the motivation and the overall aim of this work were presented. The past numerical and experimental contributions on flow and heat transfer in interrupted passages were reviewed. The main objectives of the numerical and experimental investigations conducted in this work were listed concisely.

In chapter 2, the theoretical considerations involved in the experimental and numerical investigations were discussed and presented. The governing equations relevant to this work were presented and the related assumptions were justified. The concept of a spatially-periodic fully-developed flow regime was presented and discussed. A variant of the governing equations was specially derived for the simulation of steady, laminar, spatially-periodic fully-developed flow in axially cyclic computational domains. The definitions of the turbulence power spectrums and Strouhal numbers were presented. Finally, the dimensionless parameters involved in the experiments and the main numerical simulations were listed.

The experimental apparatus and procedures were briefly described in chapter 3. An overview of the interrupted-plate duct test rig and instrumentation was presented along with its dimensions and performance characteristics. A summary of the experimental procedure was also provided. The hot-wire section that was designed in the course of this work was described along with the anemometry equipment. *The design, realization, and validation of this hot-wire measurement section is considered to be one of the*

contributions of this thesis. This new test section and the single hot-wire set-up and instrumentation, after being validated with a benchmarking investigation, were used to investigate the turbulence power spectrums and vortex shedding frequencies in the interrupted-plate duct at numerous positions.

Chapter 4 was devoted to the presentation of the finite volume method (FVM) used in the numerical investigations. First, the governing equations were recast to facilitate the time and space integration. Then, the two types of domain that were used in the simulations of flows and heat transfer in interrupted surface geometries were described. The integrated forms of the governing equations were then presented along with the numerical schemes used to approximate the diffusion and advection rates of transport. Special attention was given to the description of the QUICK scheme that was used to model the advection effects. Additional computational details, such as the treatment of solid regions, special domain boundary calculations, and underrelaxation were described. Then the discretized pressure equation was as derived. The overall solution procedure was presented along with the line-solver and block-correction algorithms. *The development, implementation, and validation of this second-order FVM are collectively considered to be one of the main contributions of this thesis. This FVM was used to perform numerical investigations of flow and heat transfer in interrupted-plate ducts and staggered-plate arrays. In the future, it may also be used to simulate various other flows with very few modifications.*

The results of the experimental investigations were presented in chapter 5. Preliminary test results were presented first, starting with the benchmarking investigation of unconfined flows past cylinders. The hot-wire instrumentation and related procedures were validated by measuring vortex shedding Strouhal numbers and comparing the data to other experimental results. For the interrupted-plate duct, repeatability and vertical symmetry were first established, and then the two-dimensionality and spatial periodicity of the turbulence power spectrums were investigated. *The demonstration of the two-dimensionality and spatial periodicity of the turbulence power spectrums is considered to be an important contribution of this thesis. It is the first time these characteristics of this flow property have been quantitatively established for this geometry.* The power

spectrums and the corresponding vortex shedding Strouhal numbers were obtained at multiple positions in the duct. *These experimental data are considered to be one of the main contributions of this work. The turbulent power spectrum measurements and dimensionless vortex shedding frequencies are potentially useful for checking and refining future mathematical models and numerical methods for the simulations of such flows.*

Additionally, in chapter 5, the results of the preliminary and main numerical investigations were presented. The numerical method was validated successfully with two test problems. First, steady spatially-periodic fully-developed laminar flow and heat transfer in staggered plate arrays were investigated and the results were compared with those of Sebben (1996). The excellent agreement of results confirmed the capability of the method to solve cyclic problems. The second test problem, involving unsteady laminar flow past a square cylinder, was then solved. The calculated Strouhal numbers and drag coefficients were in good agreement with the experimental and numerical data found in the literature, thus validating the implemented Crank-Nicolson time scheme. The first main problem of interest, unsteady laminar developing flow in interrupted-plate ducts, was then tackled. Time-mean modular friction factors and vortex shedding Strouhal numbers were obtained and showed good agreement with those calculated with an axially-cyclic domain by Sebben (1996). Multiple domain types were investigated and the modular friction factors established the existence of the spatially-periodic fully-developed regime after some distance downstream from the inlet. *This simulation of developing unsteady flows in interrupted-plate ducts is considered to be one of the main contributions of this work. This is the first time, to the author's knowledge, that unsteady laminar flows were simulated from the duct entry down to the spatially-periodic fully-developed region without the use of a cyclical domain approximation.* Finally, the results of the last main problem, unsteady laminar developing flow in staggered-plate arrays, were presented. Grid and time step independence studies were first conducted. Modular friction and Colburn factors were then obtained along with vortex shedding Strouhal numbers. The spatially-periodic fully-developed regime was shown to prevail after some distance from the inlet for most of the investigated Reynolds number range. For a

Reynolds number of 600, a larger domain was found to be necessary to establish the existence of this regime with high confidence. Numerous domains were investigated and multiple solutions were discovered when two module rows were included in the lateral direction (6X2 modules domain). The first of these stable solutions was obtained by introducing the 6X1 domain solution twice in the 6X2 domain. The second one was obtained by starting the simulation from scratch. *This is deemed as the last of the main contributions of this thesis. The existence of multiple solutions was discovered for domains containing two modules in the lateral direction. Also, this is the first time to the author's knowledge that unsteady laminar flows were solved from the array inlet plane downstream to the spatially-periodic fully-developed region.*

6.2 SUGGESTIONS FOR EXTENSIONS OF THIS WORK

A few suggestions for improvements and extensions of this thesis work are listed in this section.

The first logical extension of this work consists of gathering experimental data on friction factors in the fully-developed region of the rectangular interrupted-plate duct for the range of Reynolds numbers investigated in the numerical studies, for comparison purposes. Since the minimum flow rate limit of the apparatus is at the moment dictated by the lowest measurable differential pressure capability of the available transducer, it would be interesting to acquire a new transducer with enhanced capabilities and the extend the current experimental investigation to laminar steady, laminar unsteady, and transitional regimes.

It would also be interesting to perform additional numerical investigations of flows and heat transfer in staggered-plate arrays. The effects of including more modules in the lateral domain direction could be investigated when available computational power will make such simulations possible. Additionally, the spatially-periodic fully-developed regime could be investigated with domains having both axial and lateral cyclic conditions. Finally, geometries with smaller plate thicknesses values, representative of

actual heat exchanger cores, could be investigated. Since such geometries require much finer grids and longer domains to attain the fully-developed condition, these investigations could be performed when the required computing resources would be readily available.

In addition, the power spectrums and Strouhal numbers obtained in the experimental part of this work could be used to validate turbulence models for flows in interrupted-surface geometries. It would be interesting to perform simulations of turbulent flows in interrupted-plate ducts with suitable turbulence models, such as large eddy simulations (LES), and compare the calculated power spectrums and Strouhal numbers with the experimental data gathered in this work.

Finally, the author hopes that this thesis work will contribute to the refinement of cost-effective mathematical models and numerical methods potentially useful for designing the next generation of optimized compact heat exchanger cores.

REFERENCES

- Afshar, M. and Baliga, B.R. (1993), "A Sequential Algorithm for the Solution of the Discretized Momentum and Continuity Equations", *8th Int. Conf. on Numerical Methods in Laminar and Turbulent Flow*, Swansea, U.K., pp. 668-679.
- Amon, C.H., Majumdar, D., Herman, C.V., Mayinger, F., Mikic, B.B. and Sekulic, D. (1992), "Numerical and Experimental Studies of Self-Sustained Oscillatory Flows in Communicating Channels", *International Journal of Heat and Mass Transfer*, Vol. 35, No. 11, pp. 3115-3129.
- Amon, C.H. and Mikic, B.B. (1990), "Numerical Prediction of Convective Heat Transfer in Self-Sustained Oscillatory Flows", *Journal of Thermophysics*, Vol. 4, pp. 239-246.
- Baliga, B.R. and Atabaki, N. (2006), "Control-volume-based Finite Difference and Finite Element Methods", in *Handbook of Numerical Heat Transfer (2nd Ed.)*, W.J. Minkowycz, E.M. Sparrow, and J.Y. Murthy (Eds.), Chapter 6, John Wiley & Sons, New York.
- Batchelor, G.K. (1967), *An Introduction to Fluid Dynamics*, Cambridge University Press, Cambridge, U.K.
- Bejan, A. (1984), *Convection Heat Transfer*, J. Wiley, New York (Second Edition, 1995).
- Blancher, S., Creff, R. and Le Quéré, P. (2004), "Analysis of Convective Hydrodynamic Instabilities in a Symmetric Wavy Channel", *Physics of Fluids*, Vol. 16, pp. 3726-3737.
- Bird, R.B., Stewart, W.E. and Lightfoot, E.N. (1960), *Transport Phenomena*, J. Wiley, New York (Second Edition, 2002).
- Candanedo, J. (2003), "Time-Mean Wall Static Pressure Distributions and Module Friction Factors for Spatially Periodic Fully Developed Flows in Interrupted-Plate Rectangular Ducts", *M. Ing. Thesis*, Department of Mechanical Engineering, McGill University, Montréal, Canada.
- Candanedo, J.A., Aboumansour, E. and Baliga, B.R. (2003), "Time Mean Wall Static Pressure Distributions and Module Friction Factors for Fully Developed Flows in a Rectangular Duct with Spatially Periodic Interrupted-Plate Inserts", *Proceedings of the 2003 ASME International Mechanical Engineering Congress and Exposition*, Paper # IMECE2003-43969, Washington, D.C., pp. 1-10.
- Cebeci, T. (2002), *Convective Heat Transfer*, Horizons Publications, New York.
- Churchill, S.W. (1988), *Viscous Flows: the Practical Use of Theory*, Butterworths, Boston.

- Cur, N. and Sparrow, E.M. (1978), "Experiments on Heat Transfer and Pressure Drop for a Pair of Colinear, Interrupted Plates Aligned with the Flow", *International Journal of Heat and Mass Transfer*, Vol. 21, pp. 1069-1080.
- Cur, N. and Sparrow, E.M. (1979), "Measurements of Developing and Fully Developed Heat Transfer Coefficients along a Periodically Interrupted Surface", *ASME Journal of Heat Transfer*, Vol. 101, pp. 211-216.
- Currie, I.G. (1974), *Fundamental Mechanics of Fluids*, McGraw-Hill, New York (Third Edition, 2003).
- Davis, R.W. and Moore, E.F. (1982), "A Numerical Study of Vortex Shedding from Rectangles", *J. Fluid Mech.*, Vol. 116, pp. 475-506.
- Dejong, N.C. and Jacobi, A.M. (1997), "An Experimental Study of Flow and Heat Transfer in Parallel-plate Arrays: Local, Row-by-Row and Surface Average Behavior", *International Journal of Heat and Mass Transfer*, Vol. 40, No. 6, pp. 1365-1378.
- Dejong, N.C., Zhang, L.W., Jacobi, A.M., Balachandar S. and Tafti, D.K. (1998), "A Complementary Experimental and Numerical Study of the Flow and Heat Transfer in Offset Strip-Fin Heat Exchangers", *ASME Journal of Heat Transfer*, Vol. 120, pp. 690-698.
- Eckert, E.R.G. and Drake, R.M. (1971), *Analysis of Heat and Mass Transfer*, McGraw-Hill, New York.
- Ferziger, J.H. and Peric, M. (1996), *Computational Methods for Fluid Dynamics*, Springer, New York (Second Edition, 1999).
- Fox, R.F. and McDonald, Alan (1985), *Introduction to Fluid Mechanics*, Third Edition, Wiley and Sons, New York (Fifth Edition, 1998).
- Franke, R., Rodi, W. and Schnung (1990), "Numerical Calculation of Laminar Vortex-Shedding Flow Past Cylinders", *Journal of Wind Engineering and Industrial Aerodynamics*, Vol. 35, pp. 237-257.
- Greiner, M. (1991), "An Experimental Investigation of Resonant Heat Transfer Enhancement in Grooved Channels", *International Journal of Heat and Mass Transfer*, Vol. 34, No. 6, pp. 1383-1391.
- Grosse-Gorgemann, A., Weber, D. and Fiebig, M. (1995), "Experimental and Numerical Investigation of Self-Sustained Oscillations in Channels with Periodic Structures", *Experimental Thermal and Fluid Science*, Vol. 11, pp. 226-233.
- Hesselgreaves, J.E. (2001), *Compact Heat Exchangers: Selection, Design, and Operation*, Pergamon, New York.

Incropera, F.P., and DeWitt, D.P. (1981), *Fundamentals of Heat and Mass Transfer*, Wiley and Sons, New York (Fifth Edition, 2002).

Joshi, H.M. and Webb, R. (1987), "Heat Transfer and Friction in the Offset Strip-Fin Heat Exchanger", *International Journal of Heat and Mass Transfer*, Vol. 30, pp. 69-84.

Kakac, S. and Liu, H. (2002), *Heat Exchangers: Selection, Rating, and Thermal Design*, CRC Press, Boca Ratón, Florida, Second Edition.

Kays, W.M. (1972), "Compact Heat Exchangers", *AGARD Lecture Series*, No.57 on Heat Exchangers, AGARD-LS-57-72, NATO, pp. 1-22.

Kays, W.M. and Crawford, M.E. (1993), *Convective Heat and Mass Transfer*, McGraw-Hill, New York, Third Edition.

Kays, W.M. and London, A.L. (1964), *Compact Heat Exchangers*, Second Edition, McGraw-Hill, New York (Third Edition, 1984).

Kelkar, K.M., and Patankar, S.V. (1989), "Numerical Prediction of Heat Transfer and Fluid Flow in Rectangular Offset-Fin Arrays", *Numerical Heat Transfer A*, Vol. 15, pp. 149-164.

Kim, S.H. and Anand, N.K. (1994), "Turbulent Heat Transfer Between a Series of Parallel Plates with Surface-Mounted Discrete Heat Sources", *ASME Journal of Heat Transfer*, Vol. 116, pp. 577-587.

Lamoureux, A., Camargo, L. and Baliga, B.R. (2005), "Strouhal Numbers and Power Spectrums for Turbulent Fully-Developed Flows in Rectangular Ducts with Spatially-Periodic Interrupted-Plate Inserts", *Proceeding of Fifth International Conference on Enhanced, Compact and Ultra-Compact Heat Exchangers: Science, Engineering and Technology (CHE 2005)*, Whistler, B.C., pp. 73-80.

Landau, L.D. and Lifshitz, E.M. (1959), *Fluid Mechanics*, translated from the Russian by J.B. Sykes and W.H. Reid, Pergamon Press, Oxford (Second Edition, 1987).

Leonard, B.P. (1979), "A Stable and Accurate Convective Modelling Procedure Based on Quadratic Upstream Interpolation", *Comput. Methods Appl. Mech. Eng.*, Vol. 19, pp. 59-98.

London, A.L. and Shah, R.K. (1968), "Offset Rectangular Plate-Fin Surfaces – Heat Transfer and Flow Friction Characteristics", *ASME Journal of Engineering for Power*, Vol. 90, pp. 218-228.

Majumdar, D. and Amon, C.H. (1992), "Heat and Momentum Transport in Self-Sustained Oscillatory Viscous Flows", *ASME Journal of Heat Transfer*, Vol. 114, pp. 866-873.

Manglik, R.M. and Bergles, A. (1995), "Heat Transfer and Pressure Drop Correlations for the Rectangular Offset Strip Fin Compact Heat Exchanger", *Experimental Thermal and Fluid Science*, Vol. 10, pp. 171-180.

Masson, C., Saabas, H.J. and Baliga, B.R. (1994), "Co-Located Equal-Order Control-Volume Finite Element Method for Two-Dimensional Axisymmetric Incompressible Fluid Flow", *International Journal for Numerical Methods in Fluids*, Vol. 18, pp. 1-26.

McBrien, R.K. and Baliga, B.R. (1988), "Module Friction Factors and Intramodular Pressure Distributions for Periodic Fully Developed Turbulent Flow in Rectangular Interrupted-Plate Ducts", *ASME Journal of Fluids Engineering*, Vol. 110, pp. 147-154.

McBrien, R.K. (1989), "Fully Developed Turbulent Flow in Rectangular Interrupted-Plate Ducts", *Doctoral Thesis*, Department of Mechanical Engineering, McGill University, Montréal, Canada.

McBrien, R.K., Aboumansour, E. and Baliga, B.R. (2000), "Static Pressure Distributions and Surface Flow Visualization Data for Periodic, Fully Developed, Turbulent Flows in Rectangular Interrupted-Plate Ducts", *NCABE 2000, Proc. Fifth National Conference on Air Breathing Engines and Aerospace Propulsion*, Defence Research & Development Laboratory, Hyderabad, India, pp. 774-786.

McDonald, C.F. (1972), "Gas Turbine Recuperator Technology Advancements", *ASME Gas Turbine and Fluids Engineering and Products Show*, Paper No. 72-GT-32, San Francisco, March 26-30.

McDonald, C.F. (2000), "Low-Cost Recuperator Concept for Microturbine Applications", *Proceedings of ASME TURBOEXPO 2000*, Paper No. 2000-GT-167, Munich, Germany, May 8-11.

Michna, G.J., Jacobi, A.M. and Burton, R.L. (2005), "Air-Side Thermal-Hydraulic Performance of an Offset-Strip Fin Array at Reynolds Numbers up to 120 000", *Proceeding of Fifth International Conference on Enhanced, Compact and Ultra-Compact Heat Exchangers: Science, Engineering and Technology (CHE 2005)*, Whistler, B.C., pp. 8-14.

Minkowycz, W.J., Schneider, G.E., Pletcher, R.H. and Sparrow, E.M. (1988), *Handbook of Numerical Heat Transfer*, John Wiley and Sons, New York.

Minkowycz, W.J. and Sparrow, E.M., editors (1997), *Advances in Numerical Heat Transfer, Vol. 1*, Taylor and Francis, Washington D.C.

- Minkowycz, W.J. and Sparrow, E.M., editors (2000), *Advances in Numerical Heat Transfer, Vol. 2*, Taylor and Francis, Washington D.C.
- Mochizuki, S., Yagi, Y and Yang, W.J. (1988), "Flow Pattern and Turbulence Intensity in Stacks of Interrupted Parallel-Plate Surfaces", *Experimental Thermal and Fluid Science*, Vol. 1, pp. 51-57.
- Mullisen, R.S. and Loehrke, R.I. (1986), "A Study of the Flow Mechanisms Responsible for Heat Transfer Enhancement in Interrupted-Plate Heat Exchangers", *ASME Journal of Heat Transfer*, Vol. 108, pp. 377-385.
- Norberg, C. (1993), "Flow Around Rectangular Cylinders: Pressure Forces and Wake Frequencies", *Journal of Wind Engineering and Industrial Aerodynamics*, Vol. 49, pp. 187-196.
- Okajima, A. (1982), "Strouhal Numbers of Rectangular Cylinders", *Journal of Fluid Mechanics*, Vol. 123, pp. 379-398.
- Panton, R.L. (1996), *Incompressible Flow*, Second Edition, J. Wiley, New York.
- Patankar, S.V. (1980), *Numerical Heat Transfer and Fluid Flow*, McGraw-Hill, New York.
- Patankar, S.V., Liu, C.H. and Sparrow, E.M. (1977), "Fully Developed Flow and Heat Transfer in Ducts Having Streamwise-Periodic Variations of Cross-Sectional Area", *ASME Journal of Heat Transfer*, Vol. 99, pp. 180-186.
- Patankar, S.V. and Prakash, C. (1981), "An Analysis of the Effect of Plate Thickness on Laminar Flow and Heat Transfer in Interrupted-Plate Passages", *International Journal of Heat and Mass Transfer*, Vol. 24, pp. 1801-1810.
- Press, W.H., Teulosky, S.A., Vetterling, W.T. and Flannery, B.P. (1992), *Numerical Recipes in Fortran: The Art of Scientific Computing*, Cambridge University Press, Cambridge, U.K.
- Reddy, J.N. and Gartling, D.K. (1994), *The Finite Element Method in Heat Transfer and Fluid Dynamics*, CRC Press, Boca Ratón, Florida.
- Roache, P.J. (1976), *Computational Fluid Dynamics*, Hermosa Publishers, Albuquerque, New Mexico.
- Roadman, R.E. and Loehrke, R.I. (1983), "Low Reynolds Number Flow Between Interrupted Flat Plates", *ASME Journal of Heat Transfer*, Vol. 105, pp. 166-171.
- Rohsenow, W.M., Harnett, J.P. and Ganic, E.M., editors (1985), *Handbook of Heat Transfer Fundamentals*, Second Edition, McGraw-Hill, Toronto.

- Rouse, H. (1946), *Elementary Mechanics of Fluids*, Dover Publications Inc., New York, (Second Edition, 1978).
- Saidi, A. and Sundén, B. (2001), “A Numerical Investigation of Heat Transfer Enhancement in Offset Strip Fin Heat Exchangers in Self-Sustained Oscillatory Flows”, *International Journal of Numerical Methods for Heat & Fluid Flow*, Vol. 11, No. 7, pp. 699-717.
- Schlichting, H. (1955), *Boundary Layer Theory* (Translation of “Grenzschicht Theorie” by J. Kestin), McGraw Hill, New York (Second Edition, 1968; Third Edition, 1979).
- Sebben, S. and Baliga, B.R. (1995), “Some extensions of tridiagonal and pentadiagonal matrix algorithms”, *Numerical Methods, Part B: Fundamentals*, Vol. 28, pp. 323-351.
- Sebben, S. (1996), “Temporally and Spatially Periodic Flows in Interrupted-Plate Rectangular Ducts”, *Ph.D. Thesis*, Department of Mechanical Engineering, McGill University, Montréal, Canada.
- Sekulic, D. (1989), “Flow through Communicating Channels Compact Heat Transfer Geometry”, *International Communications in Heat and Mass Transfer*, Vol. 16, pp. 667-679.
- Settari, A. and Aziz, K. (1973), “A Generalization of the Additive Correction Methods for the Iterative Solution of Matrix Equations”, *SIAM J. Numer. Anal.*, Vol. 10, pp. 506-521.
- Shah, R.K. and London, A.L. (1978), *Laminar Flow Forced Convection in Ducts*, Advances in Heat Transfer, Supplement 1, Academic Press, New York.
- Shah, R.K., Heikal, M.R., Thonon, B. and Tochon, P. (2001), “Progress in the Numerical Analysis of Compact Heat Exchanger Surfaces”, *Advances in Heat Transfer*, Vol. 34, pp. 363-443.
- Smotrys, M.L., Ge, H., Jacobi, A.M. and Dutton, J.C. (2003), “Flow and Heat Transfer Behavior for a Vortex-Enhanced Interrupted Fin”, *Journal of Heat Transfer*, Vol. 125, pp. 788-794.
- Spalding, D.B. (1972), “A Novel Finite Difference Formulation for Differential Expressions Involving Both First and Second Order Derivatives”, *International Journal for Numerical Methods in Engineering*, Vol. 4, pp. 551-559.
- Sparrow, E.M., Baliga, B.R. and Patankar, S.V. (1977), “Heat Transfer and Fluid Flow Analysis of Interrupted-Wall Channels, with Application to Heat Exchangers”, *ASME Journal of Heat Transfer*, Vol. 99, pp. 4-11.

Sparrow, E.M. and Hajiloo, A. (1980), "Measurements of Heat Transfer and Pressure Drop for an Array of Staggered Plates Aligned Parallel to an Air Flow", *ASME Journal of Heat Transfer*, Vol. 102, pp. 426-432.

Sparrow, E.M. and Liu, C.H. (1979), "Heat Transfer, Pressure Drop and Performance Relationships for In-Line, Staggered, and Continuous Plate Heat-Exchangers", *International Journal of Heat and Mass Transfer*, Vol. 22, pp. 1613-1625.

Streeter, V.L (1951), *Fluid mechanics*, McGraw Hill, Boston (Third Edition, 1962).

Suzuki, K., Hirai, E., Miyake, T. and Sato, T. (1985), "Numerical and Experimental Studies on a Two-Dimensional Model of an Offset-Strip-Fin Type Compact Heat Exchanger used at Low Reynolds Number", *International Journal of Heat and Mass Transfer*, Vol. 28, pp. 823-836.

Suzuki, K., Xi, G.N., Inaoka, K. and Hagiwara, Y. (1994), "Mechanism of Heat Transfer Enhancement Due to Self-Sustained Oscillation for an In-line Fin Array", *International Journal of Heat and Mass Transfer*, Vol. 37, Suppl. 1, pp. 83-96.

Timmerhaus, K. D. and Flynn, T. M. (1989), *Cryogenic Process Engineering*, Plenum Press, New York.

Valencia, A. (1999), "Heat Transfer Enhancement Due to Self-Sustained Oscillating Transverser Vortices in Channels with Periodically Mounted Rectangular Bars", *International Journal of Heat and Mass Transfer*, Vol. 42, No. 11, pp. 2053-2062.

Van Doormal, J.P. and Raithby, G.D. (1984), "Enhancements of the Simple Method for Predicting Incompressible Fluid Flows", *Numerical Heat Transfer*, Vol. 7, pp. 146-163.

Webb, R.L. and Joshi, H.M. (1982), "A Friction Factor Correlation for the Offset Strip-Fin Matrix", *Heat Transfer 1982*, Vol. 6, pp. 257-262.

White, F.M. (1974), *Viscous Fluid Flow*, Second Edition, McGraw-Hill, New York (Second Edition, 1991).

Wieting, A.R (1975), "Empirical Correlations for Heat Transfer and Flow Friction Characteristics of Rectangular Offset-Fin Plate-Fin Heat Exchangers", *ASME Journal of Heat Transfer*, Vol. 97, pp. 488-490.

Wilkes, J.O. (1999), *Fluid Mechanics for Chemical Engineers*, Prentice Hall, Upper Saddle River, New Jersey.

Winternitz, F.A.L. and Fischl, C.F. (1957), "A Simplified Integration Technique for Pipe-Flow Measurement", *Water Power*, pp. 225-234.

Zelenka, R.L. and Loehrke, R.I. (1983), "Heat Transfer from Interrupted Plates", *ASME Journal of Heat Transfer*, Vol. 105, pp. 172-177.

Zhang, L.W., Balachandar, S., Tafti, D.K. and Najjar, F.M. (1997), "Heat Transfer Enhancement Mechanisms in Inline and Staggered Parallel-Plate Fin Heat Exchangers", *International Journal of Heat and Mass Transfer*, Vol. 40, No. 10, pp. 2307-2325.